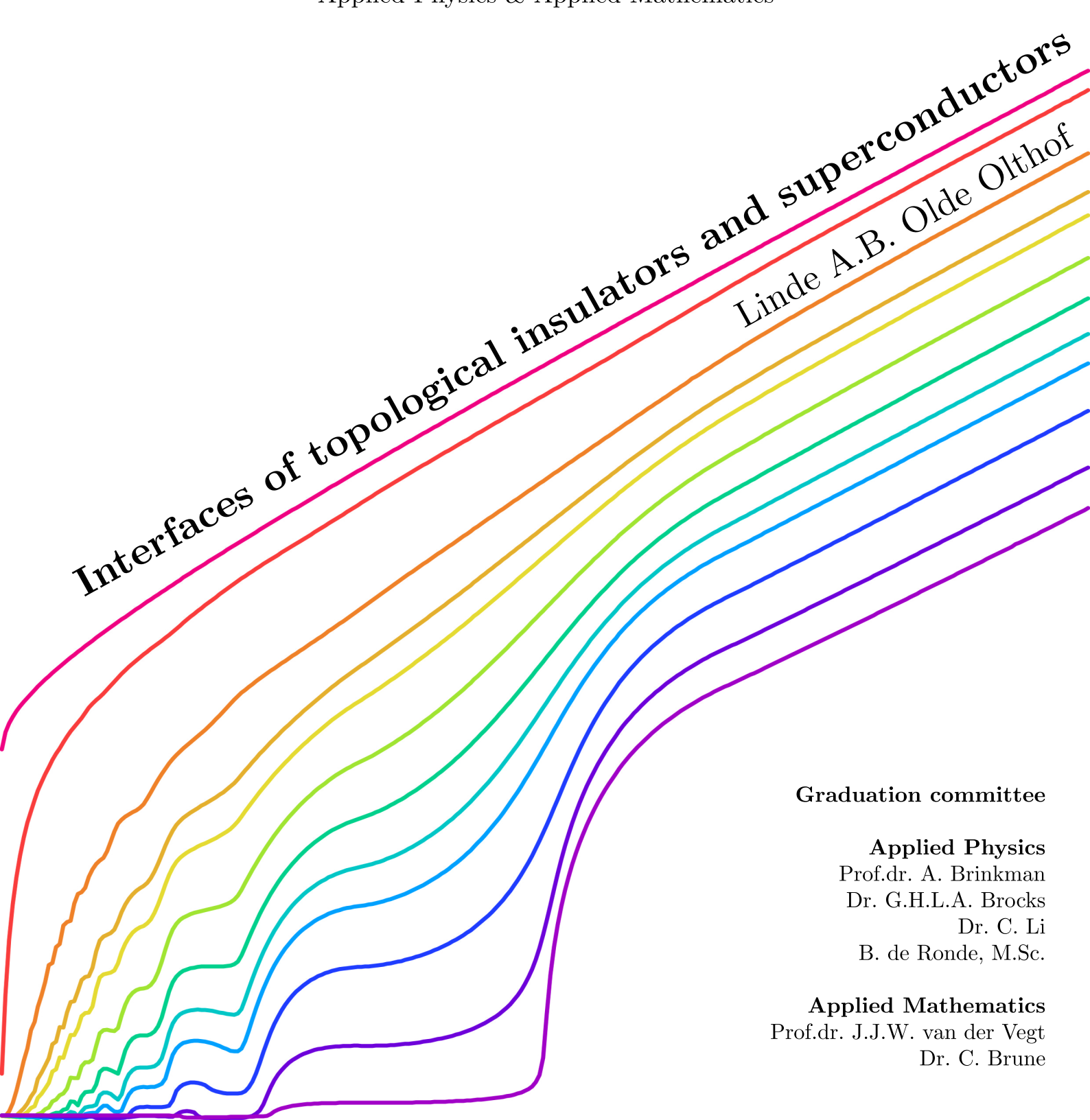


UNIVERSITY OF TWENTE.

Master's Thesis
Applied Physics & Applied Mathematics



Interfaces of topological insulators and superconductors

Linde A.B. Olde Olthof

Graduation committee

Applied Physics

Prof.dr. A. Brinkman

Dr. G.H.L.A. Brocks

Dr. C. Li

B. de Ronde, M.Sc.

Applied Mathematics

Prof.dr. J.J.W. van der Vegt

Dr. C. Brune

August 10, 2018

Abstract

At every interface with a superconductor, there is a probability that an incident electron is reflected as a spin-flipped hole, which is known as Andreev reflection. In certain geometries consisting of a topological insulator and an s -wave superconductor, Andreev reflection can lead to the formation of a Majorana bound state (MBS). Since a MBS obeys non-Abelian statistics, it can serve as a building block for topological quantum bits in future devices. In this thesis, we investigate interfaces of topological insulators and superconductors, both theoretically and experimentally.

The transport through topological Josephson junctions has a sub-harmonic gap structure as a result of multiple Andreev reflections. Oscillations in the current occur when an electron can overcome the energy gap after performing $n - 1$ Andreev reflections. We show that in a two dimensional topological Josephson junction, this energy gap depends on the Fermi surface mismatch between the superconductor and the topological insulator. This implies that the full spectrum shifts according to the mismatch, although this is hardly visible after angle averaging the current. Furthermore, we show that in the absence of an applied voltage, a bound state can exist with the same energy as seen in chiral p -wave superconductors.

Nowadays, there are two types of experiments that show the existence of MBSs; a zero bias conductance peak (ZBCP) in the differential conductance of a nanowire and a 4π periodic current-phase relation in topological Josephson junctions. It is our goal to investigate the hypothesis that these two experiments describe the same physics. We do this by probing the ZBCP in a normal metal/topological insulator/superconductor junction. If the junction is small enough, this system is able to host a surface Andreev bound state (SABS), which is characterised by Andreev reflection at the superconductor interface and normal reflection at the other interface. We present the speculative idea that the SABS is a MBS which oscillates with magnetic field, which is known as the Aharonov-Bohm effect.

Contents

Introduction	3
A note on notation	5
1 Introducing physical concepts	7
1.1 Quantum mechanics	7
1.1.1 Classical mechanics vs. Quantum mechanics	7
1.1.2 Electrons and holes	8
1.1.3 Bosons, fermions, anyons	9
1.2 Superconductors	10
1.2.1 Macroscopic view	11
1.2.2 Microscopic view	11
1.2.3 Bogoliubov-de Gennes formalism	14
1.2.4 Flux quantization	16
1.2.5 Andreev reflection	17
1.3 Topological insulators	18
1.3.1 Topology	19
1.3.2 Spin-orbit coupling	20
1.3.3 Weak antilocalisation	22
1.4 Majorana particles	22
1.4.1 Non-Abelian statistics	23
1.4.2 Two- and three-dimensional space	24
1.4.3 Superconductor / topological insulator junctions	25
2 Modelling multiple Andreev reflections	27
2.1 The resistively shunted junction model	28
2.2 The S/N/S junction in 1D	28
2.2.1 Wave functions	30
2.2.2 Recurrence relations	31
2.2.3 The DC current	32
2.3 The S/TI/S junction in 1D	34
2.4 The S/TI/S junction in 2D	36
2.4.1 Scattering matrix	37
2.4.2 Andreev coefficients	40
2.4.3 The DC current	43
2.4.4 Angle integration	44
2.4.5 Bound state energy	45

3	Numerical methods	49
3.1	Three-term recurrence relations	49
3.1.1	Minimal solutions	49
3.1.2	Asymptotic behaviour	50
3.1.3	Backward recurrence algorithm	52
3.1.4	The non-homogeneous case	56
3.2	Two-term recurrence relations	57
3.3	Comparison of algorithms for recurrence relations	58
3.3.1	Matlab backslash operator	58
3.3.2	Comparison	59
3.4	Numerical integration	61
3.4.1	Adaptive Simpson's method	61
3.4.2	Avoiding singularities	62
3.5	Angle averaging	63
4	Experimental observation of the zero bias conductance peak	65
4.1	Brief review of previous work	65
4.1.1	Zero bias conductance peak in nanowires	65
4.1.2	4π periodicity in topological Josephson junctions	66
4.1.3	Goal of this project	67
4.2	Sample design	68
4.3	Sample fabrication	69
4.3.1	Structure including tunnel barrier	69
4.3.2	Destruction of the tunnel barrier due to static charge	72
4.3.3	Structure without tunnel barrier	74
4.3.4	Sample overview	75
4.4	Zero bias conductance peak	76
4.4.1	Origin of the ZBCP	76
4.4.2	The peak height	79
4.5	Magnetic field effects	82
4.5.1	The Aharonov-Bohm effect	83
4.5.2	The Doppler shift	85
4.5.3	Weak antilocalisation	88
4.5.4	Structure outside the gap	89
4.6	$\text{Bi}_{0.97}\text{Sb}_{0.03}$	89
5	Conclusions and outlook	93
5.1	Conclusions on theoretical work	93
5.2	Conclusions on experimental work	94
5.3	Outlook	94
	Acknowledgements	97
	Appendices	99
A	Recurrence relations for the S/N/S junction	101
A.1	Recurrence relation for B_n	101
A.2	Recurrence relation for A_n	104
B	Recurrence relations for the S/TI/S junction	105
B.1	Recurrence relation for B_n	105
B.2	Recurrence relation for A_n	107

C	Scattering matrix	109
D	Nb etch rate calibration	111
E	Relation between the DOS and the conductance	113
	References	115

Introduction

Our technology is quickly developing, but our conventional transistor-based computers cannot keep up. The operating frequency of our computers is restricted, they dissipate large amounts of heat and the limit of downscaling the physical size is almost reached. We are in need of a new technology that can outperform the conventional computer in terms of operating frequency. A promising candidate is the so-called quantum computer.

A conventional, transistor-based computer uses bits that can only represent the values 0 and 1. It returns 0 if the transistor is “off” and 1 if it is “on”. A quantum computer utilizes the quantum properties of superposition, which means that a quantum bit (qubit) can be in both states at the same time. It adapts the values 0 and 1 simultaneously and therefore, it is twice as fast. Two qubits hold four values at once: 00, 01, 10 and 11. The number of values as a function of the number of bits in a conventional computer scales as n , while in a quantum computer, it scales as 2^n , implying that it is exponentially faster. Only 20 qubits are needed to take over a million values. [1, 2]

The idea of the quantum computer was initially proposed by Richard Feynman in 1981. He stated that accurate and efficient simulation of a quantum mechanical system is impossible on a conventional computer. They cannot handle the complexity and the exponentially growing amount of data that is inherent to quantum systems. A quantum computer, on the other hand, “is built of quantum mechanical elements which obey quantum mechanical laws” and should therefore be able to do the job. [3] Besides being used for fundamental quantum physics simulations, other applications are in, e.g., information theory, engineering of molecules, cryptography and language theory. [4] Moreover, the quantum computer will most likely have an even bigger impact than we can imagine. The conventional computer was first built solely to simulate Newtonian mechanics. In the 1950s, people could not imagine why anyone would want a computer in their home. A quantum computing expert at MIT claims that replacing our conventional computers with quantum computers will have the same huge impact as the conventional computer originally had; it is going to be a milestone in technology. [5]

At the moment, quantum computers have been realised at a proof of concept scale, but there are still many challenges to overcome. [6] One of the greatest challenges is protecting the qubits from noise from the surroundings that perturb the quantum states. [4] Current quantum computers can hold their quantum states for only a fraction of a second before becoming too seriously perturbed. IBM’s 50 qubit computer that was built in 2017 is able to hold a quantum state for only 90 microseconds. [7]

A possible solution to this problem is the idea of a topological quantum computer, which is presumably less sensitive to noise and therefore makes the quantum computer more stable. In these topological systems, the role of the qubit is fulfilled by a so-called Majorana bound state (MBS). A system consisting of multiple MBSs obeys non-Abelian statistics, which implies that if the system is manipulated by interchanging the positions of the MBSs, the final quantum state depends on the order in which the MBSs are interchanged. [8] This is illustrated in the figure below.

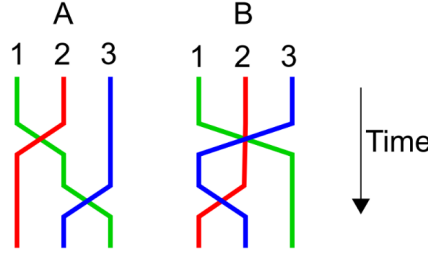


Figure 1: The order of interchanging results in a different state, such that the final states of A and B are different. From [9].

The quantum state is obtained by the process of interchanging MBSs, which is not very likely to happen as a result of noise. Therefore, a quantum computer based on MBSs is more robust against environmental noise. [8]

This concept is very appealing, but a lot of work still has to be done. MBSs and their non-Abelian statistics are exotic phenomena and not easy to realise. In order to obtain them, a very specific symmetry of the materials is required. It turns out that this can, for example, be realised by bringing a superconductor into contact with a topological insulator. The goal of this thesis is to investigate the existence of MBSs in systems of topological insulators and superconductors, both theoretically and experimentally.

The organization of this thesis is as follows: Chapter 1 introduces the physical concepts, starting from an introduction to the relevant topics of quantum mechanics and ranging to the mathematical formalisms that will be used later on. Chapter 2 consists of a theoretical study on the electrical current through superconductor/topological insulator/superconductor junctions in one and two dimensions. The goal of this study is to give a prediction for future experiments. The numerical methods that are used in the theoretical work are explained and used in Chapter 3. Chapter 4 discusses the experimental methods and measurements for spectroscopically probing the interface of a superconductor with a topological insulator. We consider a surface Andreev bound state, which consists of a single superconductor (i.e. the experiments are not related to the model of Chapter 2). Finally, in Chapter 5, conclusions are drawn and we give some recommendations for future research.

A note on notation

The use of symbols in mathematics and physics is not always consistent. Two symbols that have very different meanings in both fields are Δ and $*$. Therefore, we will introduce them here separately, to avoid any confusion.

In physics, the Laplacian, or Laplace-operator, is usually denoted by ∇^2 . What is actually meant here is $\nabla^2 = \nabla \cdot \nabla$. In mathematical textbooks, the Laplacian is often denoted by the symbol Δ . This is very confusing for physicists, since in physics, Δ corresponds to a property of superconductors. In literature, it is referred to as the energy gap, pair potential or superconducting order parameter, just to name a few.

Another point of confusion is the notation used to describe transpose and conjugate matrices. The symbol $*$ has a different meaning, depending on if we are reading a text on quantum mechanics (physics) or on linear algebra (mathematics). An overview of the notation:

	Physics	Mathematics	
Matrix	A	A	$\begin{bmatrix} a_{11} & a_{12} \\ a_{21} & a_{22} \end{bmatrix}$
Transpose matrix	A^T	A^T or A'	$\begin{bmatrix} a_{11} & a_{21} \\ a_{12} & a_{22} \end{bmatrix}$
Conjugate matrix	A^*	\bar{A}	$\begin{bmatrix} a_{11}^* & a_{12}^* \\ a_{21}^* & a_{22}^* \end{bmatrix}$
Conjugate transpose	A^\dagger	A^*	$\begin{bmatrix} a_{11}^* & a_{21}^* \\ a_{12}^* & a_{22}^* \end{bmatrix}$

We will stick to the physics notation throughout this thesis.

Introducing physical concepts

1.1 Quantum mechanics

1.1.1 Classical mechanics vs. Quantum mechanics

Classical mechanics consists mostly of the physics prior to the 20th century. It accurately describes most “normal” systems; systems that are a “normal” size (larger than a molecule and smaller than a planet) and are moving at a “normal” speed (significantly less than the speed of light). [10] Only when one of these “normal” parameters is violated, a different theory is needed.

Quantum mechanics gradually arose to explain experiments that did not match the classical descriptions anymore. A famous example is the “ultraviolet catastrophe”, i.e. in classical mechanics, black bodies can emit an infinite amount of energy. [11] This was solved by Planck’s law in 1900 and Einstein’s 1905 paper on the photoelectric effect (explaining the correspondence between energy and frequency) [12]. A couple of years later, in 1927, the famous double slit experiment took place, in which a coherent light source (e.g. a laser) is emitted towards two slits. The resulting interference pattern behind the slits revealed that the light splits into two waves and then combines again, just like a wave would do. This gave rise to the particle-wave duality of light. [13] In the mid-1920s, Schrödinger, Heisenberg and Born developed the mathematical formalisms, which we know today as quantum mechanics. [14] It describes nature on the energy smallest scales of energy levels and considers subatomic particles.

There are three major differences in which quantum mechanics differs from classical mechanics. First of all, since quantum mechanics considers small scales and individual particles, the energy, momentum and other quantities of a system may be restricted to discrete values. This is called “quantization” and is what quantum mechanics is named after. Secondly, objects have characteristics of both particles and waves (particle-wave duality). Thirdly, classical mechanics assumes that an object has definite, knowable attributes, such as its position and momentum. In quantum mechanics on the other hand, there can be limits to the precision with which quantities can be known (uncertainty principle). [14]

An important consequence is the existence of the wave function. In classical mechanics, we can simply define the position of a particle x . But since the exact position is not always known in quantum mechanics, we consider the wave function instead; a mathematical description of a quantum state,

denoted by $\psi(x)$. The wave function can be interpreted as a complex-valued probability amplitude. More concretely, [14]

$$\int_a^b |\psi(x)|^2 dx = \text{probability of finding the particle between } a \text{ and } b.$$

The wave function can be obtained via the Schrödinger equation; the most famous equation of quantum mechanics. The time-independent Schrödinger equation is an eigenvalue equation that is known as

$$\mathcal{H}\psi = E\psi, \quad (1.1)$$

where \mathcal{H} is the Hamiltonian, which is mathematical representation of the physical phenomena in the system. The wave function ψ is the eigenfunction of the Hamiltonian. The eigenvalue E corresponds to the energy of the system. We will see that the Hamiltonian is a function of momentum k , which makes the energy momentum dependent as well, i.e. $E = E(k)$. The relation between E and k is called the dispersion relation.

The Schrödinger equation is just an example. In fact, all observables in quantum physics can be written as the real eigenvalues of Hermitian operators. [14]

1.1.2 Electrons and holes

In particle physics, every particle has a corresponding antiparticle. The antiparticle has the same mass, but has the opposite charge. We will focus on electrons (the particles). In solid state physics, the antiparticle of an electron is called a hole (a positron in particle physics). The electron charge is defined as $-e$, such that a hole has charge $+e$.

A hole is usually considered as a missing electron. This can be interpreted by second quantization operators. The creation operator \hat{c}_k^\dagger creates a particle in quantum state k , whereas the annihilation operator \hat{c}_k removes it (or, equivalently, creates the corresponding antiparticle). Since a hole is a missing electron, the creation of a hole the same is as the annihilation of an electron.

The final property of electrons and holes we will discuss here is their dispersion relation. The notion of treating a hole as a missing electron turns out to be very important here. In the simplest case of a normal metal (a metal which does not have any special properties), the Schrödinger equation for electrons in one dimension is given by [14]

$$\mathcal{H}\psi = \left(-\frac{\hbar^2}{2m} \frac{\partial^2}{\partial x^2} - \mu \right) \psi = E\psi, \quad (1.2)$$

where the first term describes the kinetic energy, with \hbar the reduced Planck constant and m is the mass. The second term, μ , is the chemical potential, which can be considered as just a constant offset to the energy. Assuming a simple propagating wave, i.e. $\psi(x) = e^{ikx}$, we find that the energy (and therefore, the dispersion relation) is given by

$$E = \frac{\hbar^2 k^2}{2m} + \mu. \quad (1.3)$$

We can do the same for holes in which case we find the same result with a minus sign (this will be explained in more detail further on). Hence, we have two parabolic dispersions $E \sim \pm k^2$. The Fermi level E_F is the energy level of interest. For convenience, we take $E_F = \mu$ (which we can do since μ is an arbitrary offset). We say that the states below the Fermi level are filled with electrons, while the levels above it are empty (or filled with holes). In literature, it is conventional to depict an

electron as a solid circle and a hole as an open circle. The arrows connected to these circles represent the direction of the group velocity.

In the simple case we have considered so far, it then follows that the wave function of the particle and antiparticle are related by complex conjugation. For example, consider a propagating electron described by $\psi(x) = e^{ikx}$. The corresponding hole has the wave function $\psi^*(x) = e^{-ikx}$. This property is known as “time-reversal symmetry” and will play an important role throughout this work. Note that in many cases time-reversal symmetry is broken, most notably, by a magnetic field.

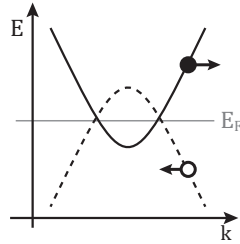


Figure 1.1: Parabolic dispersion.

	electron	hole
	particle	anti-particle
charge	$-e$	$+e$
creation	\hat{c}_k^\dagger	\hat{c}_k
annihilation	\hat{c}_k	\hat{c}_k^\dagger
energy	E	$-E$
momentum	k	$-k$
wave function	ψ	ψ^*

Table 1.1: Properties of electrons and holes.

In order not to get confused, note that we have two ways of considering electrons in a system: the “ordinary picture” and the “particle-hole picture”. Recall that the states up to the Fermi level are filled. This is called the ground state. In the ordinary picture we are concerned with these electrons. Exciting an electron leaves an empty state behind. In the particle-hole picture, we do not consider the electrons up to the Fermi level. This has the consequence that exciting electrons requires us to consider missing electrons, i.e. holes. The ordinary picture and particle-hole picture are sketched in Fig. 1.2. Throughout the rest of this work, we will mainly focus on the particle-hole picture.

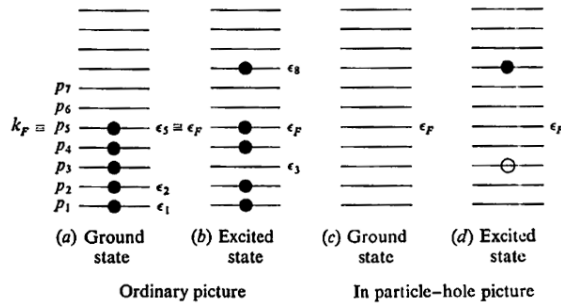


Figure 1.2: Two ways of considering non-interacting Fermi systems. Image from [15].

1.1.3 Bosons, fermions, anyons

Suppose we have two particles. In the simple case of classical mechanics, we could say that particle 1 is in state $\psi_a(x)$ and particle 2 is in state $\psi_b(x)$. In that case, the total wave function would be simply given by [14]

$$\psi(x_1, x_2) = \psi_a(x_1)\psi_b(x_2). \quad (1.4)$$

This assumes that we can tell the particles apart, otherwise it would not make any sense to give the particles number 1 and 2. In quantum mechanics, this is not the case. Particles are indistinguishable and we have to take this into account in the wave function. Two possible ways to do so are

$$\psi_{\pm}(x_1, x_2) = \frac{1}{\sqrt{2}} [\psi_a(x_1)\psi_b(x_2) \pm \psi_b(x_1)\psi_a(x_2)], \quad (1.5)$$

where $1/\sqrt{2}$ is just a normalization factor. [14] These two ways describe two kinds of particles: *bosons* (corresponding to the $+$ sign) and *fermions* (the $-$ sign). Some examples: photons are bosons, electrons are fermions. [14]

An important concept related to this topic is *spin*. Particles carry two types of angular momentum: orbital angular momentum and spin angular momentum (or, in short, spin). Spin is quantized and can either have integer or half-integer values. It turns out that all particles with integer spin are bosons, while all particles with half-integer spin are fermions. [14] In non-relativistic quantum mechanics, this is taken as an axiom. It follows naturally from the unification of quantum mechanics and special relativity, [16, 17] but this goes beyond the scope of this work. It turns out that there is a connection between the spin and statistics of bosons and fermions. This becomes evident when we try to put two particles in the same state, i.e. $\psi_a = \psi_b$. For bosons, this is not a problem at all. In the case of fermions, however, the full wave function becomes zero, which means that this is not possible. This is known as the *Pauli exclusion principle*; two identical fermions cannot occupy the same state. [14]

More generally, the wave functions (1.5) have different symmetries. Interchanging two particles (i.e. $x_1 \rightarrow x_2, x_2 \rightarrow x_1$), we find

$$\begin{array}{ll} \text{bosons} & \psi(x_1, x_2) = \psi(x_2, x_1), \\ \text{fermions} & \psi(x_1, x_2) = -\psi(x_2, x_1), \end{array}$$

or in words, the wave function for bosons is symmetric, while the fermion wave function is anti-symmetric. [14] There is, however, one other option:

$$\psi(x_1, x_2) = e^{i\phi} \psi(x_2, x_1), \quad (1.6)$$

where $i = \sqrt{-1}$ and $\phi \in \mathbb{R}$ is a phase. This type of particle is called an *anyon*. Note that since the probability is related to $|\psi|^2$, these different types of symmetry are not observable. However, it turns out to be very relevant, as will be elaborated on in Section 1.4.1.

1.2 Superconductors

Superconductivity has been a hot topic (or perhaps “a cold topic” is more appropriate in this case) since its discovery in 1911. In the early years, only the macroscopic phenomena were known. The basic concept of superconductors is explained in Section 1.2.1.

Only 46 years later, in 1957, a microscopic theory on superconductivity was postulated by Bardeen, Cooper and Schrieffer.[18] Their theory is now known as the *BCS theory* (named after the three of them). They received the Nobel Prize in 1972 for their theory. We will briefly touch upon some of the key concepts of their theory in Section 1.2.2.

The BCS wave function had been derived from a variational argument. [19] One year later, in 1958, Bogoliubov showed that it could also be obtained using a transformation of the electronic Hamiltonian. [20] This transformation is now known as the Bogoliubov transformation. It forms the basis of the Bogoliubov-de Gennes theory, which is the mathematical formalism describing the physics of superconductors. This topic is introduced in Section 1.2.3.

1.2.1 Macroscopic view

A superconductor is a special type of material that has two phases: a superconducting state and a normal state. In order to become superconducting, two properties have to be fulfilled. Firstly, when a superconductor is cooled down below its critical temperature T_c , the electric resistance suddenly drops to zero. This was discovered by H. Kammerlingh Onnes in 1911, who showed that if mercury is cooled below 4.1 K, it loses all electrical resistance. [21] The lack of electrical resistance allows an electric current flowing through a loop of superconducting wire to last indefinitely. [22] Secondly, a superconductor has a characteristic way of behaving in a magnetic field. [23] There are two types of superconductors. A type I superconductor has a single critical field H_c . If the applied magnetic field is lower than H_c and the temperature is lower than T_c , the superconductor excludes the magnetic field, which is called the Meissner effect. [23] A type II superconductor has two critical fields H_{c1} and H_{c2} . In between them, the magnetic field can partially penetrate the superconductor in the form of vortices. Below H_{c1} , the type II superconductor behaves the same as a type I superconductor. [22] If the temperature is above T_c or if the applied magnetic field is higher than H_c (type I) or H_{c2} (type II), the superconductor behaves like a normal metal. Considering both the critical temperature T_c and the critical field(s), H_c for type I and H_{c1} , H_{c2} for type II, we can construct a phase diagram for the superconductor, as shown in Fig. 1.3. The property of

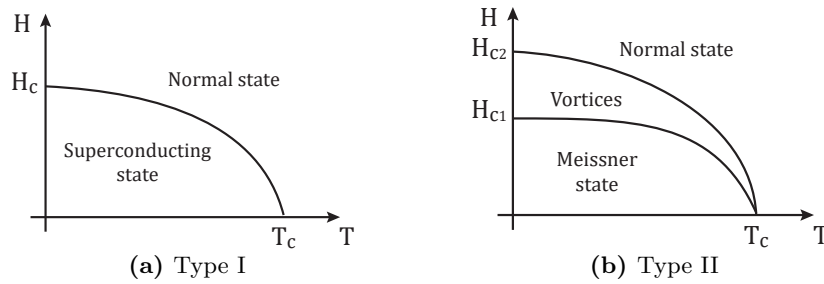


Figure 1.3: Phase diagrams of superconductors.

indefinite current and zero resistance makes superconductors very appealing candidates for future electronics, which is why it's an interesting type of materials to study. However, the goal of this work is not to look into the details of possibilities for new electronics. We are much more interested in the microscopic phenomena that are going on in superconductors.

1.2.2 Microscopic view

The first thing to note about a superconductor is that its ground state is a condensate. The easiest way to envision this is by thinking of some more everyday examples of condensates, for example, a paramagnet (magnetic moments in all directions) transitioning to a ferromagnet (magnetic moments in the same direction) or a gas (atoms moving freely), which transitions into a solid (atoms at fixed positions). This is shown in Table 1.2. In a normal metal, we have electrons with different spins and different momenta moving around. In the superconducting state, they pair up into electron pairs, so-called *Cooper pairs*. So what exactly is a Cooper pair? How and why is it formed?

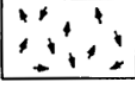

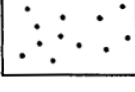
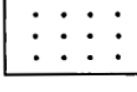
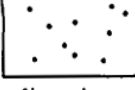
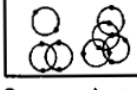
Normal phase	Condensed phase
 Paramagnet	 Ferromagnet
 Gas	 Solid
 Normal conductor	 Superconductor

Table 1.2: Examples of phase transitions from a normal state to a condensed state. From [15].

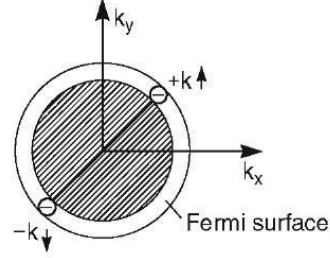


Figure 1.4: Schematic diagram of a Cooper pair; a pair of electrons with opposite momentum ($+k$ and $-k$) and opposite spin (\uparrow and \downarrow). The axes k_x and k_y denote 2D momentum space. The Fermi surface represents the 2D equivalent of the Fermi level E_F . Inside, states are filled. The Cooper pair is located just above the Fermi level. Image from [24].

Cooper pairs are pairs of electrons, but not just any two electrons. In the simplest case (and the only case that we consider here), they are pairs of electrons with opposite spin and opposite momentum. This is illustrated in Fig. 1.4

To explain why they have opposite momentum, a simplified picture is sometimes used. [24] A right-going electron state (momentum $+k$) looks like $\psi_R \sim e^{ikx}$, while a left-going state (momentum $-k$) can be written as $\psi_L \sim e^{-ikx}$. Making a pair gives a superposition of these states, i.e. $\psi_C = (\psi_R + \psi_L)/\sqrt{2}$, whose probability distribution has the form $|\psi_C|^2 \sim \cos^2(kx)$. This means that combining electron states with $+k$ and $-k$ results in a probability distribution that has a static spatial pattern. This spatial pattern slightly distorts the lattice, bringing positively charged ions closer together and therewith lowering the Coulomb energy. This is sketched in Fig. 1.5.

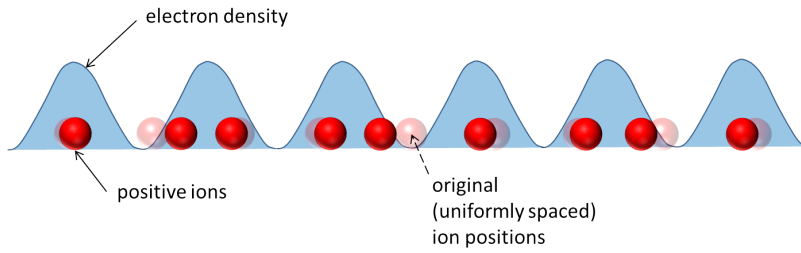


Figure 1.5: Lowering the Coulomb energy by pairing $+k$ and $-k$ states. Image from [24].

However, the pairing of these two electron states does not go on indefinitely (like a cosine). It has a finite size, which is known as the coherence lengths, ξ . This acts as an envelope around the electron density, as shown in Fig. 1.6. Hence, pairing up states with opposite momentum is a clever way of lowering the energy. Recall that we are looking for the ground state, which has the lowest energy of all possible states.

To see why electrons in Cooper pairs have opposite spin, we consider their wave function. Electrons are fermions, which means their wave function should be anti-symmetric (see Section 1.1.3).

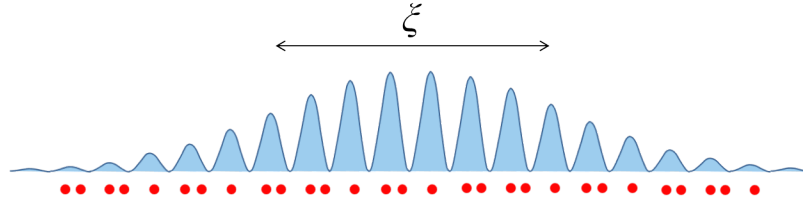


Figure 1.6: Picture of a Cooper pair with finite size ξ . Image from [24].

This can be fulfilled by considering opposite spin. Define the spins as s and s' where $s, s' \in \{\uparrow, \downarrow\}$. Under the assumption of opposite spin, the wave function gives $\psi(s, s') = \uparrow\downarrow - \downarrow\uparrow = -\psi(s', s)$, which is exactly what we were after.¹

To summarize, a Cooper pair consists of two electrons with opposite momentum and opposite spin. Hence, the momentum of the Cooper pair itself is $k - k = 0$ and its spin is $\uparrow + \downarrow = 0$. Therefore, a Cooper pair has integer spin, which means it is a boson (see Section 1.1.3). Bosons all occupy the same ground state, which is exactly what is happening in the condensate.

So then what is the excited state? When adding one extra electron to a superconductor in the ground state, we increase the energy by at least Δ . Therefore, the spectrum of excited states is separated from the ground state energy by Δ . For this reason, Δ is called the *energy gap*. It is sketched in Fig. 1.7. The value of Δ lies in the range 1 to 10 meV, depending on the material. When we want to break a Cooper pair, we have to excite both of the electrons (an unpaired electron cannot occupy the ground state), for which we need 2Δ . Therefore, Δ is also referred to as the *pair potential*. Following [25], we find that it is originally defined as

$$\Delta = -g\langle\hat{c}_{k,\uparrow}\hat{c}_{-k,\downarrow}\rangle, \quad (1.7)$$

where g is a so-called interaction constant (which is negative because of the attractive interaction). In Section 1.1.2, we defined \hat{c}_k as the annihilation operator of an electron in state k . The brackets denote the expectation value. Hence, $\langle\hat{c}_{k,\uparrow}\hat{c}_{-k,\downarrow}\rangle$ can be understood as the expectation value of the annihilation of two electrons with opposite momentum and opposite spin, i.e. the creation of a Cooper pair.

To envision Δ , recall the other condensates that we considered at the beginning of this section. In the case of ferromagnets, the relevant order parameter is magnetization, while in solids, it is the lattice constant. In superconductors, the order parameter is Δ as well.

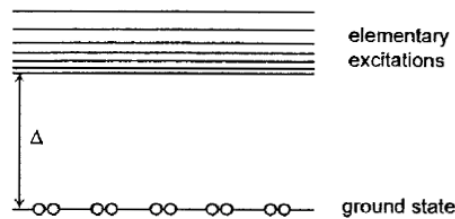


Figure 1.7: The energy gap Δ separates the excited states from the ground state (the energy level of electron pairs in the condensate). Image from [26].

¹There also exist other combinations where the electrons have the same spin. In this case, the spin part of the wave function is symmetric and another part of the wave function is antisymmetric. This type of superconductivity is known as triplet superconductivity. We will come back to this later.

In the previous section, we have discussed the macroscopic picture. We saw that superconductivity breaks down if the temperature and/or the magnetic field becomes too high. Up until now, this might seem unrelated to the Cooper pairs that we have just discussed, but in fact, these properties can be explained by the existence of Cooper pairs.

In a normal metal, in the absence of Cooper pairs, electrons repel each other, inducing electrical resistance. In a superconductor, however, the electrons form pairs which results in the disappearance of the resistance. The pairing energy of two electrons is quite weak ($\sim 10^{-3}$ eV). Thermal energy can easily break the pairs, which is the reason why Cooper pairs can only exist at low temperatures. [22]

Secondly, a Cooper pair exists of two electrons with opposite spins. Spins tend to align with the direction of an applied magnetic field. But since electrons with opposite spin are paired, it is not possible to align a Cooper pair with a magnetic field. Hence, a strong magnetic field breaks down the Cooper pair. [22]

Finally, breaking down the Cooper pairs means that we no longer have a condensate, but just a normal metal, as shown in Table 1.2.

1.2.3 Bogoliubov-de Gennes formalism

In this section, we will focus on the mathematical description of superconductors, which is done by the so-called *Bogoliubov-de Gennes* (BdG) formalism. Recall the dispersion relation for a normal metal, which is shown again in Fig 1.8a. In a superconductor, a gap Δ is introduced, as shown in Fig 1.8b. This causes the electron and hole band to mix.

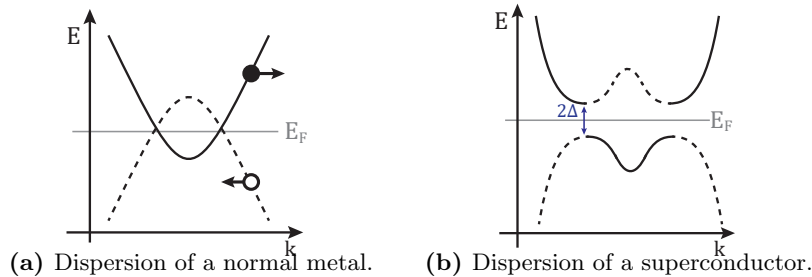


Figure 1.8: Dispersion relations. Electron and hole bands are depicted by solid and dashed lines, respectively.

As a result of the mixing of the electron and hole bands, the particles change as well. Electrons and holes become electron-like and hole-like *quasi particles*; particles that are part electron and part hole. This can be envisioned as follows: consider a horse galloping in a desert in a western movie. Around him, a cloud of dust starts to form as a result of interaction with the horse's surroundings (the desert). What is left is a galloping cloud of dust - a quasi horse. The same happens with particles in a superconductor. This is illustrated in Fig. 1.9. If the original particle is an electron, we call it *electron-like* and if it is a hole, we refer to it as *hole-like*. We will now consider the mathematical formalism to see what this implies. We first look at the case of the normal metal, which we will then compare to the superconductor.

In Section 1.1.2 we already came across the most basic Schrödinger equation for electrons. By partially integrating it twice and substituting some relations between the particles, it can be shown that $\mathcal{H}_{\text{hole}} = -\mathcal{H}_{\text{electron}}^*$ (depending on the choice of basis), such that the two Schrödinger equations

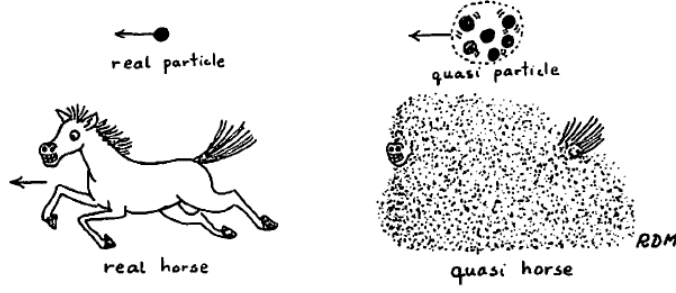


Figure 1.9: Concept of quasi particles. Image from [15].

for electrons and holes become

$$\text{electrons} \quad \left(-\frac{\hbar^2}{2m} \frac{\partial^2}{\partial x^2} - \mu \right) \psi = E\psi, \quad (1.8)$$

$$\text{holes} \quad \left(\frac{\hbar^2}{2m} \frac{\partial^2}{\partial x^2} + \mu \right) \psi = E\psi. \quad (1.9)$$

It is common to write this in matrix notation, i.e.

$$\begin{bmatrix} \left(-\frac{\hbar^2}{2m} \frac{\partial^2}{\partial x^2} - \mu \right) & 0 \\ 0 & \left(\frac{\hbar^2}{2m} \frac{\partial^2}{\partial x^2} + \mu \right) \end{bmatrix} \begin{bmatrix} \psi_e \\ \psi_h \end{bmatrix} = E \begin{bmatrix} \psi_e \\ \psi_h \end{bmatrix}, \quad (1.10)$$

where ψ_e and ψ_h correspond to the electron and hole contributions of the eigenvector (wave function), respectively. The off-diagonal elements of the matrix correspond to the interactions between particles and holes, which is absent in this case. Hence, the particles and holes are strictly separate, such that the corresponding eigenvectors are orthogonal and given by

$$\psi_{\text{electron}} = \begin{bmatrix} 1 \\ 0 \end{bmatrix}, \quad \psi_{\text{hole}} = \begin{bmatrix} 0 \\ 1 \end{bmatrix}. \quad (1.11)$$

In the case of the superconductor, we are dealing with quasi particles which are part electron and part hole. This implies that they are no longer orthogonal. Hence, we define the eigenvectors as

$$\psi_{\text{electron-like}} = \begin{bmatrix} u \\ v \end{bmatrix}, \quad \psi_{\text{hole-like}} = \begin{bmatrix} -v^* \\ u^* \end{bmatrix}. \quad (1.12)$$

We say that the quasi particles in superconductors have a weight u in the electron channel and a weight v in the hole channel, with $u^2 + v^2 = 1$. Another way to think of u and v are as amplitudes of the electron and hole wave function. The Schrödinger equations for electrons and holes are now coupled via the superconducting energy gap Δ . Together, they are called the Bogoliubov-de Gennes equations, which are given by

$$\text{electron-like quasi particles} \quad \left(-\frac{\hbar^2}{2m} \frac{\partial^2}{\partial x^2} - \mu \right) u + \Delta v = Eu, \quad (1.13)$$

$$\text{hole-like quasi particles} \quad \left(\frac{\hbar^2}{2m} \frac{\partial^2}{\partial x^2} + \mu \right) v + \Delta^* u = Ev, \quad (1.14)$$

or, in matrix notation,

$$\begin{bmatrix} \left(-\frac{\hbar^2}{2m} \frac{\partial^2}{\partial x^2} - \mu \right) & \Delta \\ \Delta^* & \left(\frac{\hbar^2}{2m} \frac{\partial^2}{\partial x^2} + \mu \right) \end{bmatrix} \begin{bmatrix} u \\ v \end{bmatrix} = E \begin{bmatrix} u \\ v \end{bmatrix}. \quad (1.15)$$

Note that if we set $\Delta = 0$, we will obtain the normal metal case again. This is exactly what happens when a superconductor transitions from the superconducting state to the normal state: the gap will gradually close.

We have now introduced the BdG formalism; the basis for most of the theory on superconductivity. The attentive reader might have noticed that there are no Cooper pairs in the BdG formalism. Where did they go? Recall the ordinary and particle-hole picture from Fig. 1.2. In the particle-hole picture, Cooper pairs simply form a “background” that we leave out. The Cooper pairs are, however, hidden in the equations. In Eq. (1.7) we showed that Δ originates from the existence of Cooper pairs. Hence, the Cooper pairs still exist in the BdG formalism, although they are not taken into account explicitly.

We will revisit the topic of quasi particles in Section 1.4, where we will introduce a very special type of particle. For now, we will first discuss a few consequences of the properties of superconductors, i.e. flux quantization and Andreev reflection.

1.2.4 Flux quantization

In the Aharonov-Bohm experiment, a beam of electrons (or a single electron) is split into two ($\psi_1 \sim e^{ikx_1}$ and $\psi_2 \sim e^{ikx_2}$) and sent past two different sides of a solenoid. The two beams travel the paths C_1 and C_2 and after passing the solenoid, the beam is recombined, resulting in an interference pattern. In the absence of a magnetic field, the interference only depends on the difference between the travelled paths of the two beams, i.e. $\Delta\Phi = k(x_2 - x_1)$. [14]

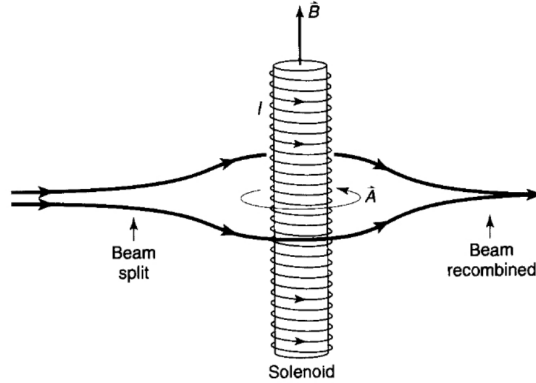


Figure 1.10: Aharonov-Bohm effect. Picture from [14].

We now consider the case where we turn on a magnetic field. The total magnetic flux through the solenoid Φ_m is determined by the applied magnetic field \vec{B} and the area of the solenoid S . We can express this in terms of the vector potential \vec{A} via one of the Maxwell equations ($\vec{B} = \nabla \times \vec{A}$). By subsequently applying Stokes theorem, we obtain

$$\Phi_m = \int_S \vec{B} \cdot d\vec{S} = \int_S (\nabla \times \vec{A}) \cdot d\vec{S} = \oint \vec{A} \cdot d\vec{r}. \quad (1.16)$$

In the presence of a magnetic field, the wave functions acquire an additional phase (say g_1 and g_2) and become of the form $\psi'_1 = e^{ig_1}\psi_1$ and $\psi'_2 = e^{ig_2}\psi_2$. These phases can be written in terms of the vector potential as $g(\vec{r}) = e/\hbar \int \vec{A}(\vec{r}) \cdot d\vec{r}$. The interference pattern is now given by [14]

$$\Delta\Phi = g_1 - g_2 = \frac{e}{\hbar} \left[\int_{C_1} \vec{A} \cdot d\vec{r} - \int_{C_2} \vec{A} \cdot d\vec{r} \right] = \frac{e}{\hbar} \oint_{C_1 \cup C_2} \vec{A} \cdot d\vec{r} = \frac{e}{\hbar} \Phi_m. \quad (1.17)$$

In a normal metal, the wave functions ψ_1 and ψ'_1 have the same physical properties. In superconductors, this is in general not the case, since type II superconductors can be partially penetrated by the magnetic field by means of vortices (see Section 1.2.1). All of these vortices carry a quantized unit of flux

$$\Phi_0 = \frac{h}{2e}, \quad (1.18)$$

where $2e$ (instead of just e) comes from the fact that Cooper pairs consist of two electrons. The quantity Φ_0 is referred to as the *flux quantum*.

If we consider one full circle, the wave function picks up the phase $\psi' = e^{i\Delta\Phi}\psi$. Since we want the wave function to be single-valued, we require $e^{i\Delta\Phi} = 1$. Making use of Eq. (1.17) with the altered electron charge $e \rightarrow 2e$, we find that

$$\Phi_m = \frac{h}{2e}m = \Phi_0 m, \quad m \in \mathbb{Z}. \quad (1.19)$$

Hence, the flux is quantized in a superconductor. This will be an important notion for the experiments that we will discuss in Chapter 4.

1.2.5 Andreev reflection

Suppose a superconductor is brought into contact with a normal metal. Remember that the charge carriers in a normal metal are electrons, whereas in a superconductor they are pairs of electrons. We consider an incident electron at a normal metal/superconductor (N/S) interface. We assume the electron has spin up and momentum k . The electron can only enter the superconductor if it finds another single electron with spin down and momentum $-k$ to form a Cooper pair with. However, single electrons are not available in the superconductor. Therefore, the pairing electron must originate from the normal metal, leaving a hole behind with spin down and momentum $-k$. This process is called *Andreev reflection* and is illustrated in Fig 1.11. Andreev reflection relies on the properties of Cooper pairs and is therefore a unique feature of superconductors.

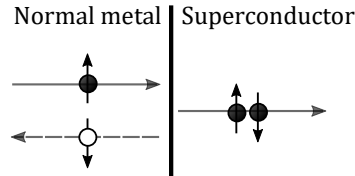


Figure 1.11: Andreev reflection. Black and white circles denote electrons and holes, respectively. The horizontal arrows represent the momentum, while the vertical arrows correspond to the spin.

We consider a superconductor with kinetic energy ξ and energy gap Δ (not to be confused with the Laplacian operator). The physics in a superconductor can be described by the Bogoliubov de Gennes (BdG) equation. The BdG equation is an eigenvalue equation. In its simplest form, it can be written as

$$\begin{bmatrix} \xi & \Delta \\ \Delta & -\xi \end{bmatrix} \begin{bmatrix} u \\ v \end{bmatrix} = \varepsilon \begin{bmatrix} u \\ v \end{bmatrix}.$$

The components of the eigenvector, u and v , represent the amplitudes of the electron and hole wave function, respectively. The eigenvalue ε corresponds to the energy and is equal to

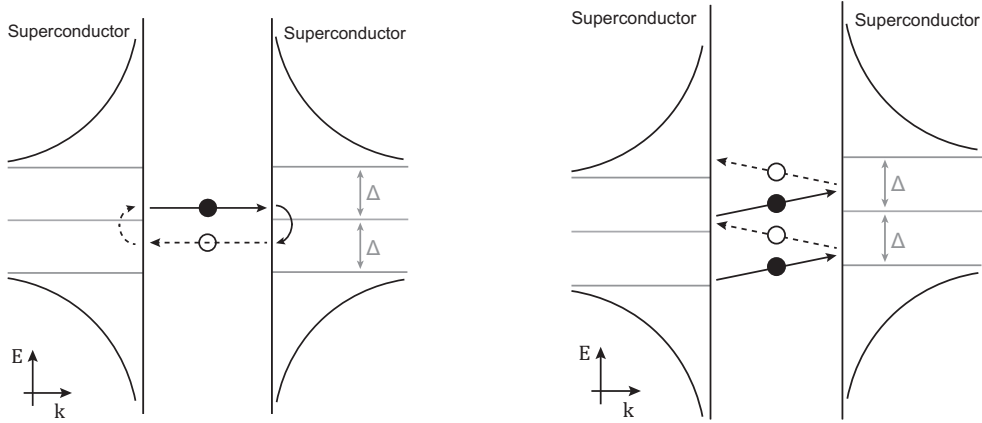
$$\varepsilon = \pm \sqrt{\xi^2 + \Delta^2}.$$

From this, we can also derive that the kinetic energy of the superconductor can then be written as $\xi = \pm\sqrt{\varepsilon^2 - \Delta^2}$ (\pm for electrons and holes, respectively). Plugging ξ back into the BdG equation and solving for the eigenfunctions, we obtain

$$\begin{bmatrix} u \\ v \end{bmatrix} = \begin{bmatrix} 1 \\ a(\varepsilon) \end{bmatrix} \quad \text{with} \quad a(\varepsilon) = \frac{1}{\Delta} \begin{cases} \varepsilon - \text{sgn}(\varepsilon)\sqrt{\varepsilon^2 - \Delta^2} & |\varepsilon| > \Delta, \\ \varepsilon - i\sqrt{\Delta^2 - \varepsilon^2} & |\varepsilon| < \Delta. \end{cases} \quad (1.20)$$

where $a(\varepsilon)$ can be interpreted as the Andreev reflection amplitude of a particle with energy ε .

Andreev reflection happens at every interface with a superconductor. Hence, if we have two superconductors, particles start bouncing back and forth in between them. If the two superconductors are at the same level, the particle keeps reflecting back and forth. This is called an Andreev bound state (figure 1.12a). However, if we apply a voltage eV , the superconductors are shifted with respect to each other. The particle will scatter to higher (or lower) energies and can eventually escape the bound state. This concept is known as multiple Andreev reflections (figure 1.12b) and section 2 will revolve around this topic.



(a) $eV = 0$, Andreev bound state.

(b) $eV \neq 0$, multiple Andreev reflections.

Figure 1.12: Reflections in between two superconductors. Solid (open) circles represent electrons (holes).

Up until now, we have not said anything about the layer in between the two superconductors. In the conventional cases, a normal metal or an insulator is placed in between them, depending on the application. In Chapter 2, we will consider a special type of material instead: the topological insulator. This type of material is also starring in the experimental results that we will discuss in Chapter 4.

1.3 Topological insulators

Normal metals are fully conducting. Normal insulators are fully insulating. A topological insulator is a type of material that is insulating in the bulk (in the interior), but becomes conducting at its surface when brought into contact with another material. The existence of the topological insulator was predicted in 2005 [27] and experimentally discovered shortly after. [28] We will first briefly introduce the topic of topology, which is what makes this type of material special. We will then

discuss the concept of spin-orbit coupling, a physical phenomenon that will turn out to be important in this research.

1.3.1 Topology

Topology is a branch of mathematics that deals with properties that are preserved under continuous deformations. For illustration, we consider three unhealthy foods: a pizza, a doughnut and the popular Dutch “oliebol” (deep-fried raisin bun). We can transform the “oliebol” into a pizza by flattening it (and adding some tomato sauce, cheese, etc.). This is a continuous deformation and therefore, we say that the “oliebol” and pizza are topologically equivalent. Transforming an “oliebol” into a doughnut, however, requires puncturing a hole in the dough, which is not a smooth deformation. Therefore, we call them topologically distinct. We can label the foods by their integer topological invariant, the so-called *genus*, g . Loosely speaking, the genus is the number of punctures. The pizza and “oliebol” have $g = 0$, while the doughnut has $g = 1$. By definition, integers cannot change continuously into one another.

We can now apply this to band structures of actual materials. Recall the parabolic band structure in a normal metal from Fig. 1.1. The top band (a) is called the *conductance band*, while the bottom band (b) is referred to as the *valence band*. A normal insulator has the same parabolic band structure, but with a gap in between the two bands. The Fermi level lies inside the gap, such that there is no electrical conductance. This is shown on the far left in Fig. 1.13. A normal insulator has topological invariant $g = 0$.

In a topological insulator, the bands a and b are inverted as a result of strong spin-orbit coupling (more on this in the next section). Therefore, its topological invariant is $g = 1$, making it topologically distinct from the normal insulator. We note that the topological insulator still has an energy gap (with the Fermi level inside it), so it is still insulating. This is depicted on the far right of Fig. 1.13.

When bringing a normal metal into contact with a topological insulator, the bands of the two materials have to connect to each other, a to a and b to b . But the band order is inverted, so what happens at the interface?

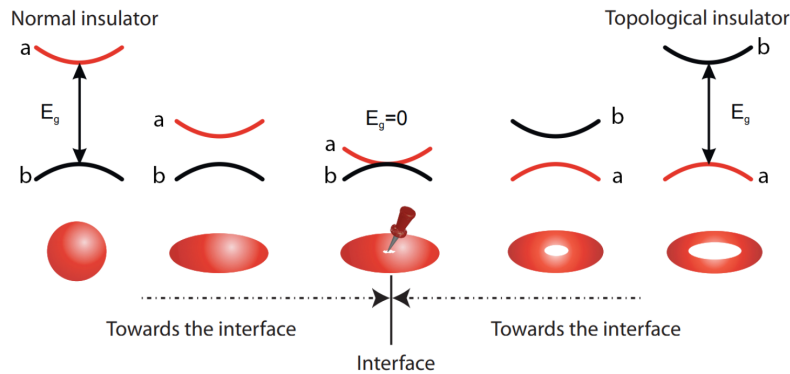


Figure 1.13: Bringing a normal insulator (left) and a topological insulator with inverted bands (right) into contact results in a band crossing at the interface. From [29].

In Hong Kong, cars drive on the left, while in China, they drive on the right. The traffic rules in both countries are not an issue, but problems arise when trying to connect the two. To solve this problem, the “Flipper bridge” was proposed (but never built). This bridge illustrates how the

distinct topological band structures are connected at the interface: a band crossing occurs. The bands cross the Fermi level, which means there is electrical conduction at the interface. We go from $g = 0$ (sphere) to $g = 1$ (thorus). At the interface, a hole is punctured in the sphere in order to obtain the thorus. This is illustrated in the middle of Fig. 1.13.



Figure 1.14: The Flipper bridge, which was proposed to connect Hong Kong to the mainland of China. If two materials with different topological ordering are connected, a band crossing occurs. From [30].

1.3.2 Spin-orbit coupling

At the interface of a normal insulator and a topological insulator, the bands are connected. It was experimentally observed that the bands at the interface are connected. [31, 32] Therefore, the Hamiltonian to describe them is linear in momentum as well, i.e.

$$\mathcal{H} = \alpha \vec{k} \cdot \hat{\sigma}, \quad (1.21)$$

where α is the coupling strength (depending on the material), \vec{k} is the momentum vector and $\hat{\sigma} = (\sigma_x, \sigma_y, \sigma_z)$, which contains the Pauli matrices

$$\sigma_x = \begin{bmatrix} 0 & 1 \\ 1 & 0 \end{bmatrix}, \quad \sigma_y = \begin{bmatrix} 0 & -i \\ i & 0 \end{bmatrix}, \quad \sigma_z = \begin{bmatrix} 1 & 0 \\ 0 & -1 \end{bmatrix}. \quad (1.22)$$

These matrices are used to calculate properties related to the spin of the particles. What is most important about Eq. (1.21) is that the momentum (orbit contribution) and the spin are connected via the inner product. In quantum mechanics, the inner product is defined as $\vec{k} \cdot \hat{\sigma} = k_x \sigma_x + k_y \sigma_y + k_z \sigma_z$. From this equation, it follows immediately that the momentum of the eigenstates is coupled to the spin. This is known as spin-orbit coupling (SOC).

In materials with strong SOC (i.e. large α), the spin is coupled to the momentum, which is referred to as *spin-momentum locking*. It has important implications for charge transport in a topological insulator. Two states with opposite spin are orthogonal, i.e. they cannot interact. Because the momentum is coupled, this implies that particles with the opposite momentum cannot interact either. We say that *backscattering* is not possible in a topological insulator. This is exactly why they are stable, as discussed in the introduction.

Solving $\mathcal{H}\psi = E\psi$ with \mathcal{H} from Eq. (1.21), we obtain the dispersion relations $E = \pm\alpha|\vec{k}|$. In two spatial dimensions, this looks like a cone, the so-called Dirac cone.² The Dirac cone and an interpretation of the spin-momentum locking are illustrated in Fig. 1.15. The absolute value in

²The name comes from Paul Dirac. He proposed the relativistic version of the Schrödinger equation, which is known as the Dirac equation. It is linear in momentum as well. All systems that have linear dispersion (most famously, topological insulators and graphene) are referred to as “Dirac-like”, the particles are called “Dirac fermions” or “relativistic particles” and the dispersion relation is known as the Dirac cone.

$E = \pm\alpha|\vec{k}|$ is crucial here. The top cone has energy $E = \alpha|\vec{k}|$, while the bottom cone has dispersion $E = -\alpha|\vec{k}|$. We note that this is fundamentally different from a dispersion without the absolute value, which describes two intersecting lines. Hence, at a fixed energy (e.g. the Fermi energy), we only have particles with one type of spin.³

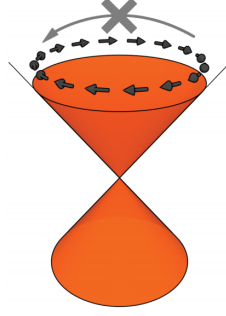


Figure 1.15: Schematic illustration of a Dirac cone. The black arrows denote the spin-momentum locking. Backscattering is not allowed. This is illustrated with the big grey arrow. From [29].

As already mentioned, the band inversion is a result of strong spin-orbit coupling. How are these two concepts related? The conduction and valence bands of a material can split for many different reasons. From a mathematical point of view, all these contributions are off-diagonal terms in the Hamiltonian. The largest contributions come from chemical bonds and crystal-field splitting (not relevant here). Finally, the much smaller contribution of the spin-orbit coupling pushes the levels closest to the Fermi level towards each other, reversing the two bands. This is illustrated schematically in Fig. 1.16. Hence, a topological insulator is the result of several splitting effects, of which strong spin-orbit coupling (strong enough to make them cross) is the most important one.

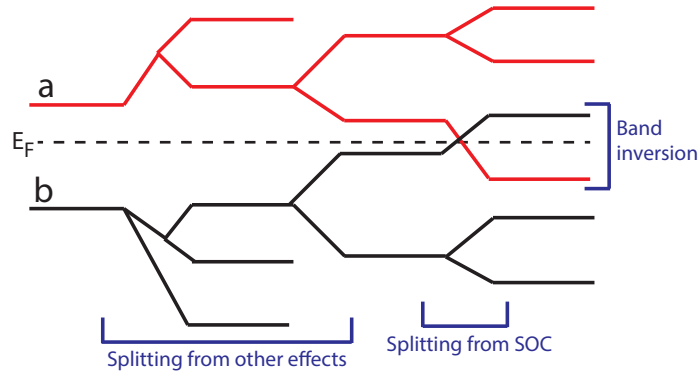


Figure 1.16: Schematic representation of effects leading to the band inversion of the conduction band (a) and the valence band (b) in a topological insulator.

³Although this is usually referred to as “chirality” instead of spin. The chirality can be ± 1 , depending on whether the spin rotates clockwise or counter clockwise.

1.3.3 Weak antilocalisation

There are three types of electronic transport in solids, which can be classified by three characteristic lengths: ℓ , ℓ_ϕ and L . The mean free path ℓ is the average distance an electron can travel before being scattered by impurities. The phase coherence length ℓ_ϕ is the average distance the electron travels before losing its phase coherence. Finally, the sample size L is the distance the electron has to travel. [33]

If $\ell \gg L$, electrons can pass through the sample without scattering, which we call it *ballistic* transport. The opposite case, when $\ell \ll L$, is known as *diffusive* transport. Usually we assume $\ell_\phi < \ell$, such that phase does not play a role. However, if $\ell_\phi \gg \ell$, electrons can maintain a phase even after many scattering events. This is called *quantum diffusive* transport. [33]

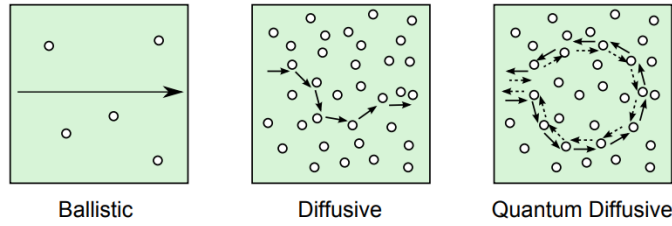


Figure 1.17: Three types of electronic transport. From [33].

In the quantum diffusive regime, an electron can scatter around and come back to a location where it was before. Weak (anti)localisation is a correction as a result of electrons interfering with themselves after scattering off impurities in the material and returning to the initial position (i.e. after completing a closed loop). This interference can be both constructive or destructive. The former is called weak localisation and the latter is referred to as weak antilocalisation. In the case of topological insulators, we have weak antilocalisation which results from the strong spin-orbit coupling that we discussed in the previous section.

Electrons travelling clockwise and counter-clockwise have opposite momentum, and because of spin-momentum locking, opposite spin as well. Hence, back-scattering (scattering to the direction where the electron came from) is suppressed, which leads to weak antilocalisation. [33]

1.4 Majorana particles

A Majorana particle is a particle that is its own antiparticle. This was hypothesized by Ettore Majorana in 1937. He suggested that some neutral (i.e. zero charge) spin- $\frac{1}{2}$ particles might be described by a real wave function. Since the wave functions of a particle and its antiparticle are related by complex conjugation, the two wave functions are identical. We note that the fact that they are neutral (i.e. zero charge) is crucial, since particles and antiparticles have opposite conserved charges (see Section 1.1.2). Put in second quantization operators, for a Majorana particle we have

$$\hat{c}_k = \hat{c}_k^\dagger. \quad (1.23)$$

Expressed in words, removing a Majorana particle in state k is equal to creating a Majorana particle in state k . Recall that the antiparticle of an electron is a hole. We can think of a Majorana as an equal superposition of an electron and a hole. Since an electron has energy E and a hole is located $-E$, we have

$$\hat{c}_k^\dagger(E) = \hat{c}_k(-E) \quad \Rightarrow \quad E = 0. \quad (1.24)$$

Hence, a Majorana particle is always located at zero energy. Since Majorana particles are part electron and part hole, a natural starting point to look for Majorana particles is in systems where both electron and hole quasi particle excitations occur; for example, in superconductors.

In an *s*-wave superconductor (that is, the standard superconductor that we have discussed so far), Cooper pairs consist of electrons with opposite spin. The annihilation operator of such an electron pair is

$$b = uc_{\uparrow}^{\dagger} + vc_{\downarrow}, \quad (1.25)$$

where c_{\uparrow}^{\dagger} is the creation operator for a spin up particle and c_{\downarrow} is the annihilation operator for a spin down particle. The coefficients u and v can be interpreted as the weights in the electron and hole channel, respectively (see Section 1.2.3). Obviously, $b \neq b^{\dagger}$. We slightly change the expression to

$$\gamma = uc_{\sigma}^{\dagger} + u^{*}c_{\sigma}, \quad \sigma \in \{\uparrow, \downarrow\}. \quad (1.26)$$

The quasi particle described by γ has equal electron and hole components, which have the same spin direction. We find that $\gamma = \gamma^{\dagger}$ and therefore, γ describes a Majorana particle.

1.4.1 Non-Abelian statistics

It turns out that Majorana particles always form pairs of the form

$$f = \frac{\gamma_1 + i\gamma_2}{2}, \quad f^{\dagger} = \frac{\gamma_1 - i\gamma_2}{2}. \quad (1.27)$$

These pairs are constructed by means of a Kitaev chain [34] (which we will not discuss here), which results in two properties: they are degenerate and highly non-local. [35, 36] The first property, the degeneracy, implies that they always come in pairs (f and f^{\dagger}). This makes sense, since a Majorana particle is half electron and half hole, but “half an electron” does not exist. Having two of them solves this problem. The second property of being highly non-local implies that the pair of Majorana particles is spatially separated. Therefore, they are protected from local changes that only affect one of them, which implies that they are protected from decoherence. This causes the Majorana particles to be insensitive to environmental noise and suitable for quantum computing, as already touched upon in the Introduction.

We now consider exchanging the two particles in a pair. Quantum mechanically, we need to include all possible ways to do. The probability amplitude is given by the sum over all possible paths from one space-time point to another,

$$A = \sum_{\text{paths}} \exp \left(i \int_{t_1}^{t_2} \mathcal{L}[\vec{r}_1(t), \vec{r}_2(t)] dt \right), \quad (1.28)$$

where the integral represents a particular path. Most of these paths destructively interfere with each other. What remains is a contribution that can be written as a phase factor to the wave function, just like we already saw in Section 1.1.3:

$$\psi(\vec{r}_1, \vec{r}_2) = e^{i\phi} \psi(\vec{r}_2, \vec{r}_1). \quad (1.6)$$

This implies that Majorana particles are anyons. A very nice mathematical explanation of these integrals in several spaces is given in [35], but here, it is enough to realize that Eq. (1.6) holds. We can go one step further.

Suppose we have N degenerate Majorana pairs. We can describe this state by the column vector $\psi = [\psi_1 \ \psi_2 \ \dots \ \psi_N]^T$. If we exchange two particles, the vector undergoes a linear transformation (a rotation of the form of Eq. (1.6)) and arrives in another state in the same degenerate space, i.e. $\psi \rightarrow U\psi$, where U is an $N \times N$ unitary matrix. If we interchange two other particles, we have the rotation $\psi \rightarrow V\psi$, with V another unitary matrix. Since U and V do not commute (which usually is the case with matrix multiplication), the order of interchanging the particles determines the final state that we arrive in. [35] Say we have three particles, 1-2-3, and we want to get the state 2-3-1. If we first interchange 1-2 and then 2-3, this gives a different final state than if we were to interchange 1-3 and then 1-2 (see Fig. 1). This property is called *non-Abelian statistics* and is crucial for applications in quantum computers, as already explained in the Introduction.

Note that, in order to have non-Abelian statistics, we need to have at least 2 degenerate states (4 Majorana particles). Otherwise, the space is one-dimensional and therefore all linear transformations commute.

1.4.2 Two- and three-dimensional space

We can consider the probability amplitude from Eq. (1.28) in two or three dimensions and these will give quite different results. We consider three possible phases of the wave function in the cases of no exchange (A), single exchange (B) and two exchanges (C).

We start with the three dimensional case as shown in Fig. 1.18a. Path A is closed and does not involve any exchange. Therefore, it can be shrunk to a point, which implies that the wave function cannot pick up a phase. Path B, with one exchange, has two different endpoints and cannot be shrunk to a point. This means that path B can result in a phase, which we call η . Path C contains two exchanges that form a loop. We can compare this with a string tied around a sphere, which we can also shrink into a point by tightening the string. Hence, two exchanges is equivalent to no exchange it all. This implies that $\eta^2 = 1$, such that $\eta = \pm 1$. In three dimensions, we can only get bosons ($\eta = 1$) or fermions ($\eta = -1$), but no anyons.

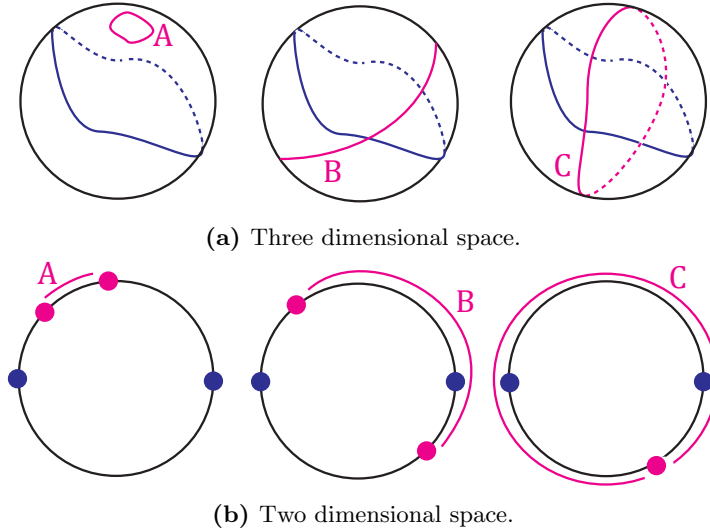


Figure 1.18: Three types of paths. A: no exchange. B: single exchange. C: two exchanges.

If we now switch to two dimensions (Fig. 1.18b), the topology of the space is different. Again, path A can be shrunk into a point and path B has fixed end points so it cannot. Path C, however, is different. This time, we imagine a string around an infinitely long cylinder, which of course

cannot be shrunk into a point. Therefore, we have a phase η after one exchange, a phase η^2 after two exchanges, a phase η^3 after three exchanges, and so on. Hence, the phase has to be $\eta = e^{i\phi}$, which explains why we can only get the anyon wave function in two dimensions.

The mathematical crux lies in the study of the topology of these space, as already introduced in Section 1.3.1. The sphere in three dimensions has genus $g = 0$ (it is similar in shape to an “oliebol”), or, in mathematical terms, we can say that it is *simply connected*. Two dimensional space is not simply connected. This makes it possible to define paths that wind around the origin, resulting in the anyon behaviour. A full discussion on these spaces using homotopies (i.e. continuous deformations from pizzas to “oliebollen”) from three dimensions to \mathbb{Z}_2 and from two dimensions to \mathbb{Z} is given in [35].

The reason why we went through the hassle of relating Majorana behaviour to the topology of two and three dimensional space, is that it will turn out to be an important issue in the experiments that we will discuss in Chapter 4.

1.4.3 Superconductor / topological insulator junctions

We have now established the construction and importance of Majorana particles. The question that arises is, what kind of system supports their existence? From Eq. (1.26) it follows that we are looking for a superconductor where pairing between electrons with the same spin happens. This type of pairing is known as *triplet pairing*.⁴ Moreover, the structures of f and f^\dagger are ($\sim \gamma_1 \pm i\gamma_2$) are crucial here as well. The most obvious candidate to fit these two criteria is a chiral p -wave superconductor. In the superconductors we have considered so far, the Δ parameter was a constant (see Section 1.2.3). In a chiral p -wave case, it is momentum dependent and has the structure

$$\Delta(\vec{p}) = \Delta(p_x \pm ip_y) = \Delta e^{\pm i\phi}, \quad (1.29)$$

where p_x and p_y are the momentum components in the x and y direction, respectively, and $\phi = \tan(p_y/p_x)$. This structure implies that the pair potential Δ is rotating as a function of momentum. The direction of the rotation can be either \pm , which is called the *chirality*.

The most well known chiral p -wave superconductor is Sr_2RuO_4 . However, it is very difficult to realise this material experimentally. Besides that, the actual pair potential remains a point of discussion and it is still not proven that Sr_2RuO_4 has indeed the pairing symmetry described by Eq. (1.29). [37]

There are, however, other ways to induce triplet pairing in materials. A well known way to do so is using nanowires, which we will discuss in Section 4.1.1. Another possibility, which is the topic of interest here, is bringing a standard s -wave superconductor (with a constant Δ and Cooper pairs with opposite spin) in combination with a topological insulator.

When we first introduced the Majorana particle at the beginning of this section, we considered it as a particle that is half electron/half hole and that is located at zero energy. As discussed in Section 1.2.5, two superconductors with another material in between them can host an Andreev bound state (see Fig. 1.12a). If this bound state is located at zero energy, does that turn the Andreev bound state into a Majorana bound state? Almost.

In the conventional case, the material in between the two superconductors is a normal metal, which has the parabolic dispersion relation that was shown in Fig. 1.8a. If the interfaces are absolutely perfect, an electron (without hole component) reflects as a hole (without electron component) and there is no interaction between the two bands. Therefore, there are states at zero energy, so in principle, this should work. In reality, however, the interfaces are not perfect. The two bands

⁴The name “triplet pairing” comes from the fact that there are three ways to pair electrons that are symmetric under exchange: $|\uparrow\uparrow\rangle$, $|\downarrow\downarrow\rangle$ and $|\uparrow\downarrow\rangle + |\downarrow\uparrow\rangle$. This is opposed to singlet pairing, where we only had $|\uparrow\downarrow\rangle - |\downarrow\uparrow\rangle$, as discussed in Section 1.2.2.

interact and a gap in the dispersion opens, comparable to the dispersion shown in Fig. 1.8b. The zero energy level lies inside this gap and therefore, it is impossible to have a Majorana bound state in this system. [29, 38]

If we replace the normal metal in the middle by a topological insulator, this problem is solved. Recall that a topological insulator has spin-momentum locking (see Section 1.3.2) and therefore, backscattering is not possible. Hence, a particle inside the topological cannot go back; it can only go into the superconductor. Therefore, the transmission is equal to 1. We will see in Section 4.4.2 that this is a crucial property to host a Majorana particle.

It can be shown mathematically that the spin-momentum locking of Eq. (1.21) with induced superconductivity results in the same energy spectrum as the $p_x + ip_y$ superconductor. This idea was first postulated in the famous work of Fu and Kane. [39] In Chapter 2, we will calculate the current through a superconductor/topological insulator/superconductor junction and it will turn out that we find indeed the p -wave bound state energy spectrum.

Modelling multiple Andreev reflections

There are several ways to detect a Majorana particle. The most common ones are the use of nanowires and the 4π periodic current-phase relation. These two methods will be explained in Chapter 4, when we look at the experimental aspects of detecting a Majorana particle. In this chapter, we focus on yet another method, which considers multiple Andreev reflections (MAR).

The concept of MAR was explained in Section 1.2.5. MAR occur in junctions with two superconductors with a different material in between them. A superconductor/normal metal/superconductor (S/N/S) junction is called a *conventional Josephson junction*. If we replace the normal metal with a topological insulator, we have a superconductor/topological insulator/superconductor (S/TI/S) junction, which is referred to as a *topological Josephson junction*.

In Section 2.1, we will first discuss the rather simple resistively shunted junction model that has been used to model S/N/S junction. This model does not take MAR into account. The current through a one dimensional S/N/S junction as a result of MAR was first modelled by Averin-Bardas in 1995. Their model is discussed in Section 2.2. As a next step, we are interested in a junction with a topological insulator (TI) in the middle. When a TI is brought into contact with a superconductor, its surface becomes superconducting as well via the proximity effect. This combination of spin-momentum locking and superconductivity allows symmetry protected surface states to host Majorana particles; which has been a hot topic for the past decades. The one dimensional S/TI/S junction and its relation to Majorana particles were considered by Badiane, Houzet and Meyer in 2011. A brief review of their work is given in Section 2.3.

The S/TI/S model showed a phenomena that is fundamentally different from the S/N/S junction. This is very interesting, however, it is not directly applicable to experiments. The reason is that experimental junctions cannot be considered one dimensional. The current can also flow through the junction under an angle, which makes the system two dimensional. The experimentally obtained result then corresponds to the current averaged over all possible angles. We expanded the existing one dimensional model to two dimensions to make an actual experimental prediction. By going to two dimensions, we are able to take the length of the TI, as well as the chemical potentials of both materials into account. Our expanded model is shown in Section 2.4.

We have obtained some very remarkable results. The angle that we introduced is a measure for the Fermi surface mismatch between the topological insulator and the superconductor. This mismatch shifts the full spectrum. After angle averaging, however, most of the MAR structure was lost. We also showed that in the absence of an applied voltage, the S/TI/S junction hosts a bound state that

is similar to the bound state in chiral p -wave superconductors.

2.1 The resistively shunted junction model

A frequently used tool to model S/N/S junctions is the resistively shunted junction (RSJ) model. In the RSJ model, a resistor (R) is put parallel to the S/N/S junction (JJ), such that the current can be modelled as the sum of the supercurrent I_S (the current in the absence of an applied voltage) and the normal state current I_N (Ohmic behaviour). This is shown in Fig 2.1.

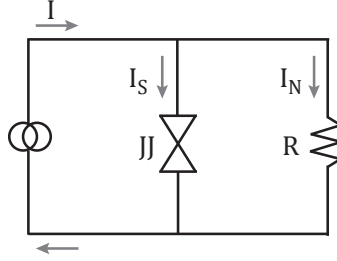


Figure 2.1: Resistively shunted junction model.

The supercurrent has amplitude I_c (the critical current) and oscillates as a function of the phase difference between the two superconductors ϕ . In this simple model, the voltage V is given by the magnetic flux quantum ($\hbar/2e$) times the phase ϕ . Summing the two contributions, we obtain

$$I_{RSJ} = I_S + I_N = I_c \sin \phi + \frac{\hbar \phi}{2eR}. \quad (2.1)$$

Because of its simplicity, this model is popular among experimentalists. However, it can only explain the experimental observations to some extent. The RSJ model does not take many physical aspects of the S/N/S junction into account. Especially the quantum properties are left out. For example, whereas the RSJ model gives a smooth I/V curve, experiments show an oscillating sub-harmonic gap structure (i.e. oscillations for $eV < \Delta$, where V is the applied voltage and Δ is the superconducting gap).

The main phenomenon that is responsible for the current in S/N/S junctions is the effect of multiple Andreev reflections (MAR), which will be the main topic of this chapter.

2.2 The S/N/S junction in 1D

Averin and Bardas [40] modelled the current through a S/N/S junction. They start by defining two additional regions I and II inside the superconductors, close to the interface (Fig 2.2). These regions represent the parts of the contact regions that are separated by the scattering region, where the motion of the quasi particles is possibly diffusive. The current through the junction is determined by the interplay of two effects: Andreev reflection at the interfaces with the superconductors, and scattering in the middle region. A short review of the work done by Averin and Bardas is discussed in this section.

We assume an incoming electron-like quasi particle from the left superconductor, which we model as $J\delta_{n0}$. There is only one source at $n = 0$, which is why we use the Kronecker δ -function. The amplitude is given by $J = \sqrt{1 - a_0^2}$. When the electron-like quasi particle reaches the interface,

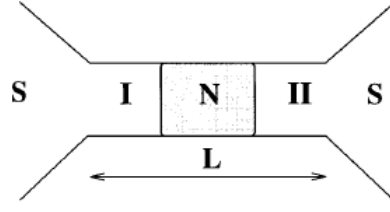


Figure 2.2: Schematic diagram of S/N/S junction. Image from [40].

there are four possible processes:

- | | |
|--|-------|
| 1. Reflection as an electron-like particle (normal reflection) | B_n |
| 2. Reflection as a hole-like particle (Andreev reflection) | A_n |
| 3. Transmission as an electron-like particle | C_n |
| 4. Transmission as a hole-like particle | D_n |

The letters behind these processes are the probabilities assigned to the occurrence of each process. After one of these processes has taken place, there will be a new particle approaching an interface and the same four processes can happen again. This is why we introduced the subscript n . From Fig 1.12b, it becomes clear that in the case of Andreev reflection, the particle goes to a different energy level. This is taken into account by the Andreev coefficient a_n , which is defined as $a_n = a(\varepsilon + neV)$, where a is given by Eq. (1.20). The full process that takes place in the S/N/S junction is illustrated in Fig 2.3.

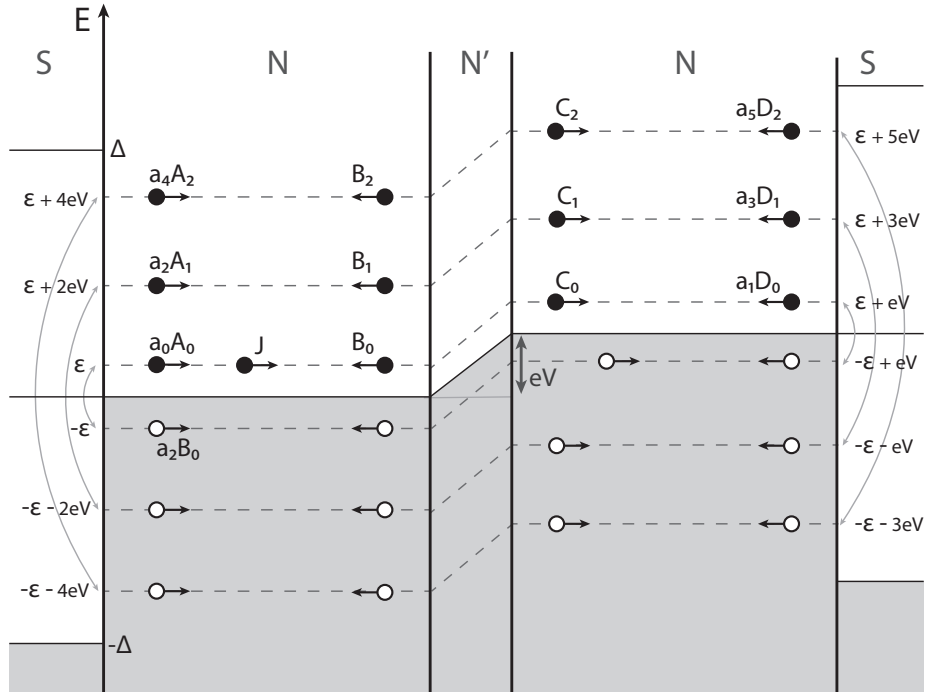


Figure 2.3: Schematic diagram of the Averin Bardas coefficients.

2.2.1 Wave functions

We are interested in the wave functions for holes and electrons in the regions I and II. We first consider the electrons in region I.



In this region, we have the source term J , which is a right-going particle with momentum k . Since we assume a propagating particle, we multiply the source term by e^{ikx} . The reflected electron-like particle B_n goes in the opposite direction, $-k$, hence, it is multiplied by e^{-ikx} . To take all reflected electron-like particles into account, we sum over n . After an even number of Andreev reflections, we get another right-going electron-like particle with amplitude $a_{2n}A_n$ and momentum k .

What we discussed until now are all position dependent contributions to the wave function. However, the differential equation that we are dealing with also has a time derivative. Since the position dependent part and the time dependent part can be separated, we write the solution as $\psi(x, t) = \psi(x)\psi(t)$. For the most standard form of the Schrödinger equation, the time dependent part is $e^{-iEt/\hbar}$, where E is the energy and t denotes the time. In this case, every Andreev reflection shifts the energy level. The energy of an electron is increased by eV each time it passes through the channel from left to right. The energy of holes increases in the opposite direction; from right to left. Taking this together, we obtain the energy difference $2eV$. Hence, the electron and hole wave functions are sums of components with different energies shifted $2eV$. Taking all of these aspects into account, the electron wave function in region I can be written as

$$\psi_e^I(x, t) = \sum_n [(a_{2n}A_n + J\delta_{n0})e^{ikx} + B_ne^{-ikx}] e^{-i(\varepsilon+2neV)t/\hbar}. \quad (2.2)$$

We can do the same for hole-like quasi particles in region I.



We have the Andreev reflected hole-like particles A_n that are propagating in the $-k$ direction. If a particle that was originally reflected as an electron (B_n) is then Andreev reflected at the next interface, we obtain the right-going hole-like particle $a_{2n}B_n$. Similar to the previous case, the wave function is given by the sum over all Andreev levels n , multiplied by the same time dependent part. The wave functions becomes

$$\psi_h^I(x, t) = \sum_n [A_ne^{ikx} + a_{2n}B_ne^{-ikx}] e^{-i(\varepsilon+2neV)t/\hbar}. \quad (2.3)$$

We move on to the electrons in region II.



If the source particle J is normally transmitted, it ends up in region II as a right-going electron-like particle with amplitude C_n . An Andreev reflected hole at the right interface ends up as an electron-like particle in region II as well. This particle is denoted by $a_{2n+1}D_n$. Because of the energy difference eV in the middle (as seen in Fig 2.2), we now have to take the odd Andreev coefficients a_{2n+1} . This is also taken into account in the time dependent part. The electron wave function in region II is given by

$$\psi_e^{II}(x, t) = \sum_n [C_ne^{ikx} + a_{2n+1}D_ne^{-ikx}] e^{-i(\varepsilon+(2n+1)eV)t/\hbar}. \quad (2.4)$$



Finally, we have to consider the holes in region II.

If the source particle J is transmitted as a hole-like particle, we obtain the particle denoted by D_n , with momentum k . Andreev reflected electrons at the right interface become left-going hole-like particles $a_{2n+1}C_n$. The wave function we obtain is

$$\psi_h^{II}(x, t) = \sum_n [a_{2n+1}C_n e^{ikx} + D_n e^{-ikx}] e^{-i(\varepsilon + (2n+1)eV)t/\hbar}. \quad (2.5)$$

To summarize, the wave functions in region I and II can be written as

$$\begin{aligned} \text{(I)} \quad \psi_e &= \sum_n [(a_{2n}A_n + J\delta_{n0})e^{ikx} + B_n e^{-ikx}] e^{-i(\varepsilon + 2neV)t/\hbar}, \\ \psi_h &= \sum_n [A_n e^{ikx} + a_{2n}B_n e^{-ikx}] e^{-i(\varepsilon + 2neV)t/\hbar}, \\ \text{(II)} \quad \psi_e &= \sum_n [C_n e^{ikx} + a_{2n+1}D_n e^{-ikx}] e^{-i(\varepsilon + (2n+1)eV)t/\hbar}, \\ \psi_h &= \sum_n [a_{2n+1}C_n e^{ikx} + D_n e^{-ikx}] e^{-i(\varepsilon + (2n+1)eV)t/\hbar}. \end{aligned}$$

2.2.2 Recurrence relations

The next step is to match the wave functions. We assume the wave functions Eqs. (2.2)-(2.5) are known. Because we do this, we can neglect the superconductors and focus only on the N/N'/N structure in the middle. Since we do not want to define the wave function in the middle N' layer, we use the technique of scattering matrices. A vector with the amplitudes of the outgoing particles (away from the middle N' layer) is expressed as the multiplication of the scattering matrix with a vector consisting of the incoming particles (towards the middle N' layer). The scattering matrix consists of the reflection and transmission coefficients r and t , respectively. The reflection and transmission probabilities are then given by $|r|^2$ and $|t|^2$, respectively. Because of probability conservation, we have $|r|^2 + |t|^2 = 1$. The factor $|t|^2$ has an additional interpretation; it describes the transparency of the interface, which is defined as $D \equiv |t|^2$. We note that the r and t coefficients are independent of the A_n , B_n , C_n , D_n coefficients, since the latter depend on the superconductors (which we do not take into account here).

For electron-like particles, the relation between incoming and outgoing particles is given by

$$\begin{bmatrix} B_n \\ C_n \end{bmatrix} = S_e \begin{bmatrix} \delta_{n0} + a_{2n}A_n \\ a_{2n+1}D_n \end{bmatrix}, \quad S_e = \begin{bmatrix} r & t \\ t & -r^*t/t^* \end{bmatrix}. \quad (2.6)$$

Similarly, for hole-like particles, we obtain

$$\begin{bmatrix} A_n \\ D_{n-1} \end{bmatrix} = S_h \begin{bmatrix} a_{2n}B_n \\ a_{2n-1}C_{n-1} \end{bmatrix}, \quad S_h = S_e^* = \begin{bmatrix} r^* & t^* \\ t^* & -rt^*/t \end{bmatrix}, \quad (2.7)$$

where $S_h = S_e^*$ can be interpreted as the fact that holes are the time-reverse of electrons.

The matrix vector equations (2.6) and (2.7) simply describe a system of four equations with four unknowns (A_n , B_n , C_n and D_n). In appendix A, we show that by substituting these equations into one another, we obtain the recurrence relations

$$D \frac{a_{2n+2}a_{2n+1}}{1-a_{2n+1}^2} B_{n+1} - \left[D \left(\frac{a_{2n+1}^2}{1-a_{2n+1}^2} + \frac{a_{2n}^2}{1-a_{2n-1}^2} \right) + 1 - a_{2n}^2 \right] B_n + D \frac{a_{2n}a_{2n-1}}{1-a_{2n-1}^2} B_{n-1} = -\sqrt{1-D}\delta_{n0}, \quad (2.8)$$

$$A_{n+1} - a_{2n+1}a_{2n}A_n = \sqrt{1-D}(a_{2n+2}B_{n+1} - a_{2n+1}B_n) + a_1\delta_{n0}. \quad (2.9)$$

These equations can be solved numerically to find expressions for the amplitudes B_n and A_n .

2.2.3 The DC current

The A_n and B_n coefficients determine the Fourier components of the current $I(t)$ through the junction,

$$I(t) = \sum_k I_k e^{2ikeVt/\hbar}.$$

At zero temperature ($T = 0$), the Fourier components I_k are given by

$$I_k = \frac{e}{\pi\hbar} \left[eVD\delta_{k0} - \int J(\varepsilon) \left\{ a_{2k}^* A_k^* + a_{-2k} A_{-k} + \sum_n \left(1 + a_{2n} a_{2(n+k)}^* \right) (A_n A_{n+k}^* - B_n B_{n+k}^*) \right\} d\varepsilon \right], \quad (2.10)$$

where $J(\varepsilon) = \sqrt{1-a_0^2}$. We recall that $a_n = a(\varepsilon + neV)$, where a is given by Eq. (1.20). The DC component can be obtained by setting $k = 0$, i.e.

$$I_0 = \frac{e}{\pi\hbar} \left[eVD - \int J(\varepsilon) \left\{ a_0^* A_0^* + a_0 A_0 + \sum_n (1 + |a_{2n}|^2) (|A_n|^2 - |B_n|^2) \right\} d\varepsilon \right], \quad (2.11)$$

whereas the AC components are described by the higher harmonics ($k > 0$) as

$$I_k = -\frac{e}{\pi\hbar} \int J(\varepsilon) \left\{ a_{2k}^* A_k^* + a_{-2k} A_{-k} + \sum_n \left(1 + a_{2n} a_{2(n+k)}^* \right) (A_n A_{n+k}^* - B_n B_{n+k}^*) \right\} d\varepsilon.$$

We focus on the DC current I_0 (as described by eq. (2.11)), which is plotted for varying interface transparencies D in Fig 2.4. (The current is normalised by I_Δ , which is simply the transparency D . For low transparencies ($D \sim 0.001$), the current starts flowing at $eV = 2\Delta$. Superconductors have an energy gap in the density of states of 2Δ . Inside this gap, there are no available states and therefore, charge transfer is not possible (Fig 2.5a). When applying a voltage, the densities of states start to shift with respect to one another. For convention, we assume that a positive voltage shifts the density of states of the right superconductor upwards. When the top band of the left superconductor is aligned with the bottom band of the right superconductor, electrons from the right superconductor transfer to the vacant states in the left superconductor (Fig 2.5b), because the states on the left have a lower energy. Hence, current starts to flow from right to left as soon as the gap has been overcome, which happens at $eV = 2\Delta$.

MAR give rise to characteristic oscillations in the current (most visible in the green curves for $D = 0.4$ and $D = 0.7$). These oscillations are a result of singularities. It follows directly from

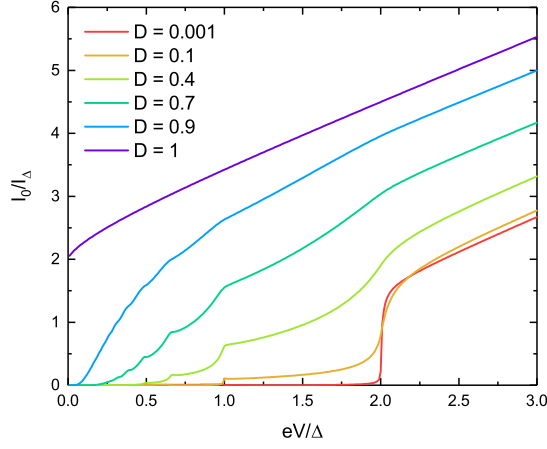


Figure 2.4: The DC current I_0 through an S/N/S junction as a function of eV/Δ .

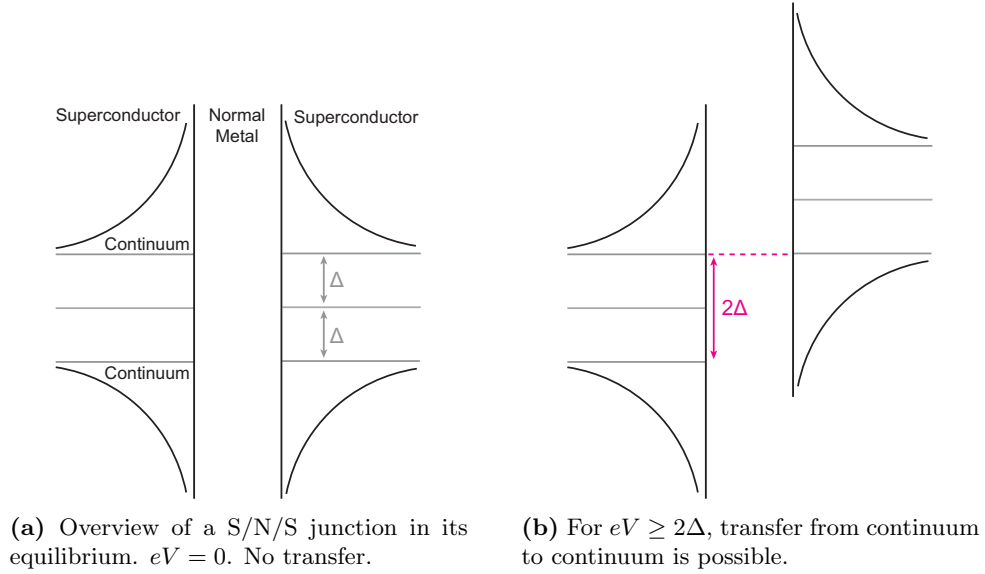


Figure 2.5

Eq. (2.8) that if one of the denominators becomes zero (i.e., $1 - a_{2n\pm 1}^2 = 0$), the recurrence relation diverges. For abbreviation, we use $q = 2n \pm 1$. The equation $1 - a_q^2 = 0$ is equivalent to

$$a_q = a(\varepsilon + qeV) = \frac{\varepsilon + qeV - \text{sgn}(\varepsilon + qeV)\sqrt{(\varepsilon + qeV)^2 - \Delta^2}}{\Delta} = \pm 1.$$

We square the equation in order to remove the square root and the sign function. Rewriting the result, we find

$$\begin{aligned} (\varepsilon + qeV)^2 - \Delta^2 &= (\varepsilon + qeV \pm \Delta)^2 \\ &= (\varepsilon + qeV)^2 \pm 2\Delta(\varepsilon + qeV) + \Delta^2. \end{aligned}$$

The $(\varepsilon + qeV)^2$ term cancels. We divide by 2Δ to obtain

$$\varepsilon + qeV = \pm\Delta.$$

The energy is defined to be zero in the middle of the gap. The gap has size 2Δ . Hence, we are interested in the values $\varepsilon = \pm\Delta$. When ε and Δ have the same sign, we simply get $eV = 0$. In the other case, where they have opposite signs, we find

$$eV = \pm \frac{2\Delta}{q}, \quad q = 2n \pm 1, \quad n \in \mathbb{N}. \quad (2.12)$$

This can be interpreted as the particle overcoming the energy gap 2Δ after $q-1$ Andreev reflections. We note that $q = 2n \pm 1$ implies that q is an odd integer. This can be attributed to the fact that the voltage eV is taken with respect to the left superconductor. However, since we integrate over the energy, we also get the singularities from the other interface, i.e.

$$eV = \pm \frac{2\Delta}{q}, \quad q \in \mathbb{N}. \quad (2.13)$$

2.3 The S/TI/S junction in 1D

Badiane et al. [41] replaced the normal layer in the middle by a TI. With a TI in the middle layer, one expects the transparency D to always be equal to 1. Badiane et al. introduce magnetisation into their system to consider cases where $D \neq 1$. The only change they made in the model was adding an additional minus sign for the reflection coefficient for holes ($r' = -r$), such that the scattering matrices change to

$$\begin{aligned} \begin{bmatrix} B_n \\ C_n \end{bmatrix} &= S_e \begin{bmatrix} \delta_{n0} + a_{2n}A_n \\ a_{2n+1}D_n \end{bmatrix}, & S_e &= \begin{bmatrix} r & t \\ t & -r^*t/t^* \end{bmatrix}, \\ \begin{bmatrix} A_n \\ D_{n-1} \end{bmatrix} &= S_h \begin{bmatrix} a_{2n}B_n \\ a_{2n-1}C_{n-1} \end{bmatrix}, & S_h &= \begin{bmatrix} -r^* & t^* \\ t^* & rt^*/t \end{bmatrix}. \end{aligned}$$

The signs that are different from the previous case are marked in red. In a similar way as before, the recurrence relations can be derived from here. This is shown in appendix B. The recurrence relations are

$$D \left[\frac{a_{2n+2}a_{2n+1}}{1 + a_{2n+1}^2} B_{n+1} + \left(\frac{a_{2n+1}^2}{1 + a_{2n+1}^2} + \frac{a_{2n}^2}{1 + a_{2n-1}^2} \right) B_n + \frac{a_{2n}a_{2n-1}}{1 + a_{2n-1}^2} B_{n-1} \right] - (1 + a_{2n}^2) B_n = -\sqrt{1-D}\delta_{n0}, \quad (2.14)$$

$$A_{n+1} - a_{2n+1}a_{2n}A_n = -\sqrt{R}(a_{2n+2}B_{n+1} + a_{2n+1}B_n) + a_1\delta_{n0}. \quad (2.15)$$

Solving (2.14) and (2.15) yields expressions for B_n and A_n . The definition of the current through a junction remains unchanged. Hence, we can calculate the corresponding current using eq. (2.11), which is shown in Fig 2.6.

Comparing Fig 2.6 to Fig 2.4, we note that current starts to flow at $eV = \Delta$ (instead of $eV = 2\Delta$ from before). This can be explained by considering a Majorana state in the middle of the gap (Fig 2.7a). [41] When we shift the density of states of the right superconductor by $eV = \Delta$, the continuum of the right superconductor is aligned with the mid gap state of the left superconductor (Fig 2.7b). Therefore, the current starts to flow from $eV \geq \Delta$. For higher transparencies ($D \sim 1$), the two systems give the same results.

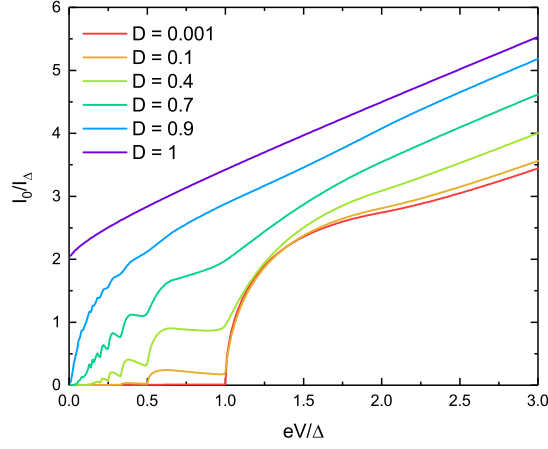


Figure 2.6: The DC current I_0 through an S/TI/S junction.

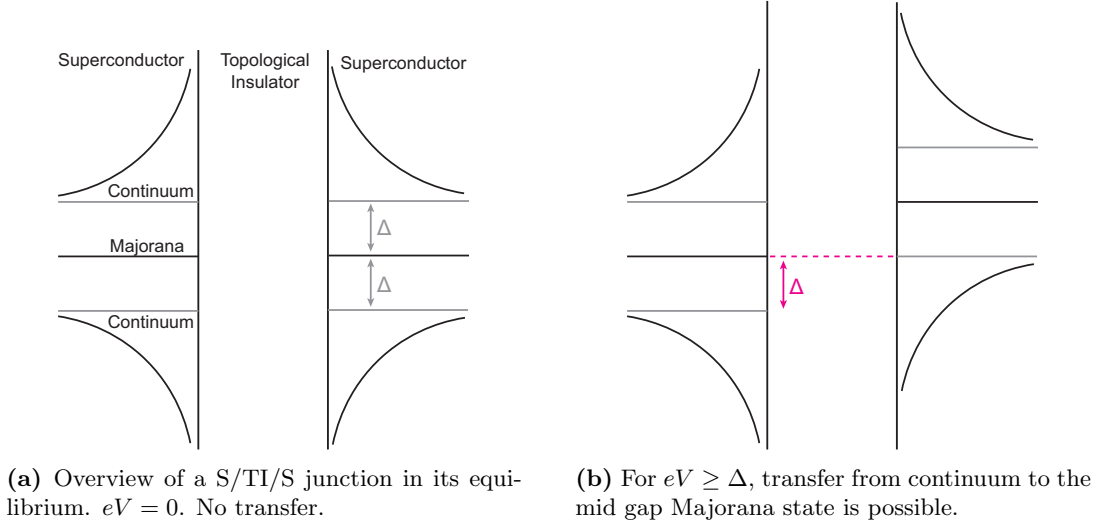


Figure 2.7

Transport to the mid gap state also follows from the singularities. Eq. (2.14) has singularities when $1 + a_q^2 = 0$, with $q = 2n \pm 1$. This is the case when $a_q = \pm i$. Squaring the equation, we obtain

$$\begin{aligned} (\varepsilon + qeV)^2 - \Delta^2 &= (\varepsilon + qeV \pm i\Delta)^2 \\ &= (\varepsilon + qeV)^2 \pm 2i\Delta(\varepsilon + qeV) - \Delta^2. \end{aligned}$$

Both the $(\varepsilon + qeV)^2$ and the Δ^2 term cancel. What remains is

$$\pm 2i\Delta(\varepsilon + qeV) = 0.$$

Considering again the case where $\varepsilon = \pm\Delta$, this reduces to

$$eV = \pm \frac{\Delta}{q}, \quad q \in \mathbb{N}, \quad (2.16)$$

which differs by a factor 2 from Eq. (2.12) for the conventional S/N/S case.

2.4 The S/TI/S junction in 2D

Up until now we only considered 1D junctions, corresponding to a single mode channel. In actual experiments, a flake of a topological material is used, which is a couple μm in width and length. On top of it, two superconducting leads are placed. The leads have to cover the whole width of the flake, which implies they are several μm in width as well. This is shown in Fig. 2.8a. Because of this non-negligible dimension, the current will not only flow perpendicular between the leads, but also under an angle. This is illustrated by the arrows in the figure. In experiments, it is not possible to filter out only one angle (the perpendicular direction). Instead, a superposition of the contributions of all angles is observed. Therefore, we expect that an angle dependent model will fit the experimental data better than the 1D model from the previous section. The aim of this section is to model the S/TI/S junction in 2D, where the two dimensions are the in-plane dimensions as shown in Fig. 2.8a. We refer to them as x and y and define θ as the in-plane angle.

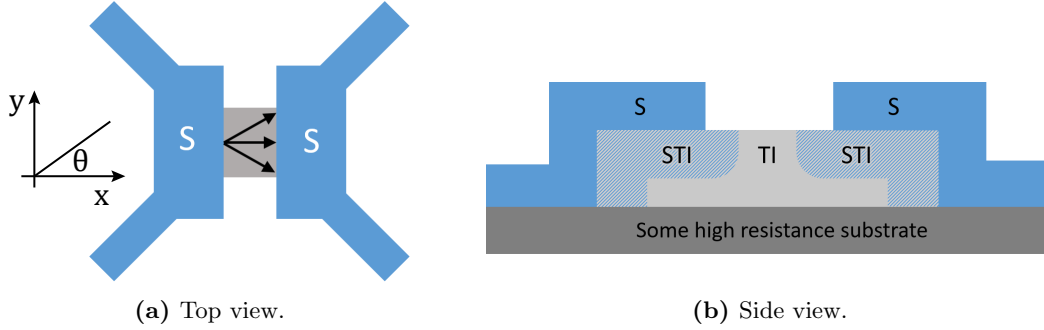


Figure 2.8: S/TI/S junction. [42]

Considering the side view of the same junction (Fig. 2.8b), we see the the superconducting leads are placed on top of the TI. At the interface of the S and the TI, some of the superconductivity leaks into the TI, making the TI locally superconducting as well. This effect is known as the superconducting proximity effect. The region in the TI that becomes superconducting is called STI. As a side note, the S/TI/S junction is placed on top of a high resistance substrate. This implies that the substrate does not contribute to the current and we can consider the S/TI/S junction as an isolated system.

We are only interested in the STI/TI/STI junction and neglect the S parts from now on. This has the additional advantage that we do not have to take the z -direction into account. There is an applied voltage V over the junction. For the purpose of modelling, we assume the potential drop eV to be located in the middle of the TI region. Using this, we are able to split the TI into three regions: two regular TIs and a scattering region TI' in between them (similar to the S/N/S case from Section 2.2).

Our junction is now divided into five parts: STI/TI/TI'/TI/STI. An overview of the structure, the corresponding dispersion relations and Fermi surfaces is shown in Fig 2.9. Since the STIs are superconducting, there is an induced gap in the linear dispersion. The applied voltage in the TI' region results in an offset in the dispersion. Therefore, its Fermi surface is smaller.

To make the system two dimensional, we give our source particle J an angle θ , which is the angle with respect to the normal to the interface. The angle dependency enters in two ways. Firstly, in the transport coefficients r and t in the scattering matrix. These coefficients then determine the angle dependent transparency D . This is discussed in Section 2.4.1. Secondly, the Andreev reflection at the interface with the superconductor becomes angle dependent as well, i.e. the Andreev coefficients

a_n will depend on θ , which is derived in Section 2.4.2. Since these processes happen at different locations in the junction, we can focus on different parts of our STI/TI/TI'/TI/STI junction (and neglect the others). This is also illustrated in Fig 2.9.

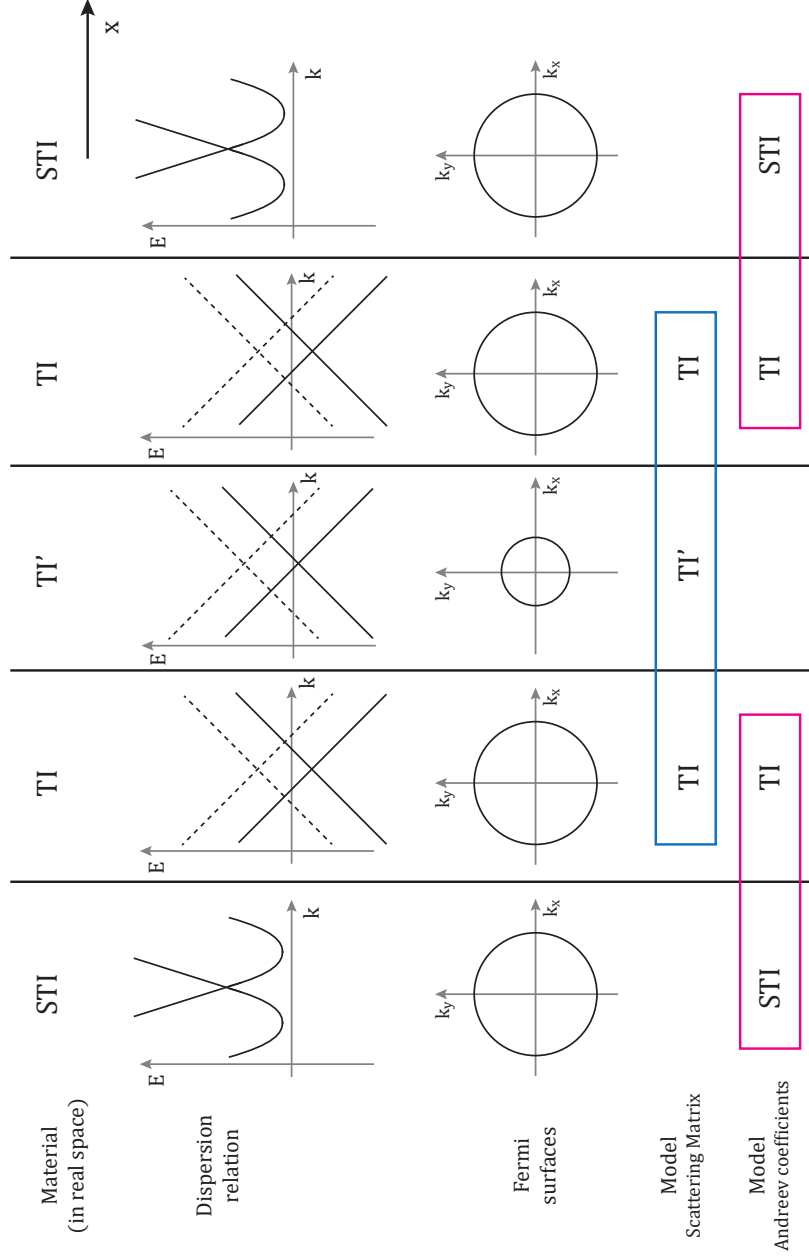


Figure 2.9: Overview of the STI/TI/TI'/TI/STI structure, including the dispersion relations and Fermi surfaces. The bottom of the figure shows which parts are used for which model.

2.4.1 Scattering matrix

In this system, scattering is a result of the potential difference that is located in the TI' layer. Hence, to determine the scattering matrix, we can neglect the superconductivity and focus only on the TI/TI'/TI junction. This is also depicted in blue at the bottom of Fig 2.9.

The scattering matrix relates the outgoing to the incoming wave function amplitudes. We have to be careful which basis we take here. We define $\psi_{L(R)\pm}$ as the wave function amplitudes of quasi particles carrying the charge current in the $\pm x$ -direction for $x < 0$ ($x > L$).

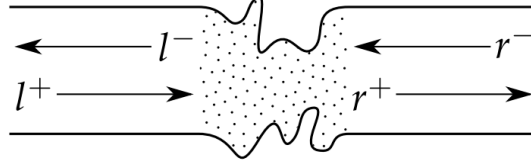


Figure 2.10: The scattering region ($0 < x < L$) is described in terms of the incoming and outgoing particles. They are labeled by l^\pm and r^\pm , depending on their propagation direction. Image from [43].

In this basis, the scattering matrix is defined by

$$\begin{bmatrix} \psi_{L-} \\ \psi_{R+} \end{bmatrix} = \begin{bmatrix} r & t \\ \underline{t} & \underline{r} \end{bmatrix} \begin{bmatrix} \psi_{L+} \\ \psi_{R-} \end{bmatrix}. \quad (2.17)$$

Here, r and t correspond to an incoming particle from the left and \underline{r} and \underline{t} are for a particle from the right. We are mainly interested in the reflection coefficient r . The reflection probability R is equal to $R = |r|^2$. Because of probability conservation, the transmission probability (the transparency) is $D = 1 - R$. This D appears in the recurrence relations. In this section, we will derive an expression for r . For completeness, the full scattering matrix is derived in Appendix C.

Since all three regions are topological insulators, all of them are described by the Dirac equation

$$i\hbar \frac{\partial}{\partial t} \psi = \hat{H} \psi. \quad (2.18)$$

The left-hand side is the time dependent part. In the stationary limit (which we use here), Eq. (2.18) reduces to the standard eigenvalue equation $\hat{H} \psi = E \psi$. The right-hand side is the position dependent part, where \hat{H} is the Hamiltonian given by

$$\hat{H} = \hbar v \hat{\sigma} \cdot \vec{k} = \hbar v \begin{bmatrix} 0 & k_x - ik_y \\ k_x + ik_y & 0 \end{bmatrix} = \hbar v |k| \begin{bmatrix} 0 & e^{-i\theta} \\ e^{i\theta} & 0 \end{bmatrix}, \quad (2.19)$$

where we used that $k_x = |k| \cos \theta$ and $k_y = |k| \sin \theta$. The inner product used here is known as “spin-momentum locking”, since it couples the spin ($\hat{\sigma}$) to the momentum (\vec{k}). This Hamiltonian has energies $E = \pm \hbar v |k|$ and spinors $\psi = \frac{1}{\sqrt{2}} [1 \quad \pm e^{i\theta}]^T$.

The potential difference in the TI’ layer is assumed to be constant and can be described as

$$V(x) = \begin{cases} V & \text{for } 0 < x < L, \\ 0 & \text{otherwise,} \end{cases} \quad (2.20)$$

where L is the thickness of the TI’ layer. This is illustrated in Fig 2.11.

Due to the potential in the TI’ layer, we expect the momentum to be different there. In the middle layer, we define our momentum in the x -direction as k_x and the angle as θ . Since the TI regions ($x < 0$ and $x > L$) are adjacent to the STI, we define the momentum as k_x^S and the angle as θ_S . Since we assumed the potential drop to be in the x -direction, we take a simple propagating wave

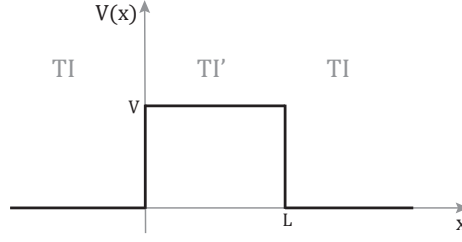


Figure 2.11: TI/TI'/TI junction modelled as a quantum well.

in the y -direction. Hence, the wave function in the three regions is given by

$$\psi(x, y) = \begin{cases} \frac{1}{\sqrt{2}} \left(\begin{bmatrix} 1 \\ e^{i\theta_S} \end{bmatrix} e^{ik_x^S x} + r \begin{bmatrix} 1 \\ -e^{-i\theta_S} \end{bmatrix} e^{-ik_x^S x} \right) e^{ik_y y} & \text{for } x < 0, \\ \frac{1}{\sqrt{2}} \left(a \begin{bmatrix} 1 \\ e^{i\theta} \end{bmatrix} e^{ik_x x} + b \begin{bmatrix} 1 \\ -e^{-i\theta} \end{bmatrix} e^{-ik_x x} \right) e^{ik_y y} & \text{for } 0 < x < L, \\ \frac{t}{\sqrt{2}} \begin{bmatrix} 1 \\ e^{i\theta_S} \end{bmatrix} e^{ik_x^S x} e^{ik_y y} & \text{for } x > L. \end{cases} \quad (2.21)$$

In order to match these wave functions at $x = 0$ and $x = L$, we have to impose appropriate boundary conditions. A “physical” solution describes a state that can be prepared with finite energy in finite time. The very minimum condition for a wave function to be physically acceptable is that it should be square integrable, i.e.

$$\int |\psi(x)|^2 dx < \infty, \quad (2.22)$$

independent of the integration limits. This integral is interpreted as the probability of finding the particle within these integration limits. Physicists argue that this probability cannot change abruptly, i.e. $\int |\psi(x)|^2 dx$ should not have discontinuities. This implies that $|\psi(x)|^2$ itself should be continuous. Since $|\psi|^2 = \psi\psi^*$, it follows that the wave function ψ itself has to be continuous. This can be proven mathematically via the construction of rigged Hilbert spaces, as explained in [44]. The continuity at $x = 0$ and $x = L$ is imposed as

$$\lim_{x \uparrow 0} \psi(x, y) = \lim_{x \downarrow 0} \psi(x, y), \quad \lim_{x \uparrow L} \psi(x, y) = \lim_{x \downarrow L} \psi(x, y). \quad (2.23)$$

Note that in systems described by higher order differential equations (such as the regular Schrödinger equation), more boundary conditions are needed. The simple case of the Dirac equation (Eq. (2.18)) is a first order equation and therefore, imposing continuity at $x = 0$ and $x = L$ is sufficient.

Substituting the wave functions (Eq. (2.21)) into the boundary conditions (Eq. (2.23)) yields a system of four equations with four unknowns (r , a , b and t). Solving this system, we find the expressions for r to be equal to

$$r = 2e^{i\theta_S} \sin(k_x L) \frac{\sin \theta_S - \sin \theta}{e^{-ik_x L} \cos(\theta_S + \theta) + e^{ik_x L} \cos(\theta_S - \theta) - 2i \sin(k_x L)}. \quad (2.24)$$

The same expression has been found before for Klein tunneling in graphene [45] and in Dirac semimetals. [38] As mentioned before, we will use that the transparency of the junction is equal to $D = 1 - |r|^2$. The full scattering matrix for electrons is derived in Appendix C.

It is insightful to keep in mind the situation with a normal metal in the middle. In this case, the Hamiltonian is given by

$$\hat{H} = \begin{bmatrix} -\frac{\hbar^2}{2m} \left(\frac{\partial^2}{\partial x^2} + \frac{\partial^2}{\partial y^2} \right) & 0 \\ 0 & \frac{\hbar^2}{2m} \left(\frac{\partial^2}{\partial x^2} + \frac{\partial^2}{\partial y^2} \right) \end{bmatrix}, \quad (2.25)$$

which has eigenvalues $E = \pm \hbar k^2/2m$ and eigenvectors $\psi = [1 \ 0]^T$ and $[0 \ 1]^T$. These spinors are orthogonal, i.e. there is no mixing and no angle dependency. **The angle dependency of the scattering matrix is a result of the spin-momentum locking in the topological insulator.**

2.4.2 Andreev coefficients

The model used in this section is based on Ref. [46]. Since Andreev reflection happens at the interface with the superconductor, we focus on the topological insulator/superconductor interfaces. This is illustrated at the bottom of Fig 2.9 in pink. Since superconductivity mixes electrons and holes, we will use the four component spinors. In the topological insulator, the spinors for electrons (e) and holes (h) are given by

$$\psi_e(\theta) = \frac{1}{\sqrt{2}} \begin{bmatrix} 1 \\ e^{i\theta} \\ 0 \\ 0 \end{bmatrix}, \quad \psi_h(\theta) = \frac{1}{\sqrt{2}} \begin{bmatrix} 0 \\ 0 \\ 1 \\ -e^{-i\theta} \end{bmatrix}. \quad (2.26)$$

Neglecting the superconducting phase, the spinors in the superconductor are given by

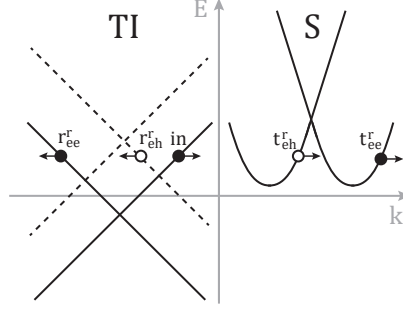
$$\psi_{Se}(E, \theta_S) = \frac{\chi_e(E)}{2\sqrt{2}\Delta} \begin{bmatrix} 1 \\ e^{i\theta_S} \\ -\frac{\Delta}{\chi_e(E)^2} e^{i\theta_S} \\ \frac{\Delta}{\chi_e(E)^2} \end{bmatrix}, \quad \psi_{Sh}(E, \theta_S) = \frac{\chi_h(E)}{2\sqrt{2}\Delta} \begin{bmatrix} 1 \\ e^{i\theta_S} \\ -\frac{\Delta}{\chi_h(E)^2} e^{i\theta_S} \\ \frac{\Delta}{\chi_h(E)^2} \end{bmatrix}, \quad (2.27)$$

with $\chi_e(E) = \sqrt{E + \sqrt{E^2 - \Delta^2}}$ and $\chi_h(E) = \sqrt{E - \sqrt{E^2 - \Delta^2}}$.

In Section 2.2, we discussed the four possible processes that can take place. Since we will consider the same situation four times, introducing super- and subscripts comes in handy when naming the coefficients. The notation is as follows: all reflections are called r , all transmissions are named t . The superscript is either r or l , which represents the right or left interface, respectively. The subscripts consist of two letters, which can be either e (electron-like) or h (hole-like). The first letter is the incoming particle, while the second letter corresponds to the outgoing particle.

We start by considering an incoming electron-like quasi particle at the right interface. The names of the coefficients are

r_{ee}^r	Normal reflection (electron \rightarrow electron),
r_{eh}^r	Andreev reflection (electron \rightarrow hole),
t_{ee}^r	Transmission as an electron-like particle (electron \rightarrow electron),
t_{eh}^r	Transmission as a hole-like particle (electron \rightarrow hole).

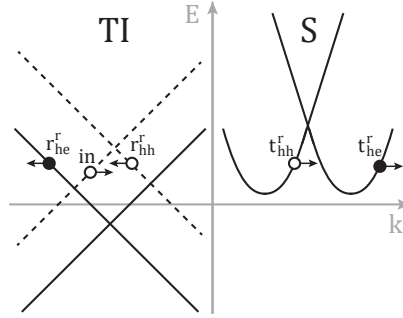


The corresponding boundary condition is

$$\psi_e(\theta) + r_{ee}^r \psi_e(\pi - \theta) + r_{eh}^r \psi_h(\theta) = t_{ee}^r \psi_{Se}(E, \theta_S) + t_{eh}^r \psi_{Sh}(E, \pi - \theta_S). \quad (2.28)$$

An incoming hole at the right interface has the same for processes with coefficients

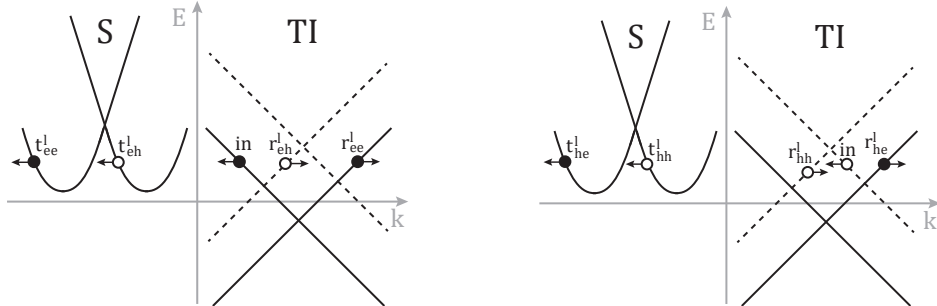
r_{hh}^r	Normal reflection (hole \rightarrow hole),
r_{he}^r	Andreev reflection (hole \rightarrow electron),
t_{hh}^r	Transmission as a hole-like particle (hole \rightarrow hole),
t_{he}^r	Transmission as an electron-like particle (hole \rightarrow electron).



The incoming hole-like quasi particle at the right interface gives the boundary condition

$$\psi_h(\pi - \theta) + r_{hh}^r \psi_h(\theta) + r_{he}^r \psi_h(\pi - \theta) = t_{he}^r \psi_{Se}(E, \theta_S) + t_{hh}^r \psi_{Sh}(E, \pi - \theta_S). \quad (2.29)$$

We can do the same for the left interface. The names of the coefficients are the same as before, but the superscript r (right) changes to l (left). In the boundary conditions, all angles change by a factor π because the direction of incoming, reflected and transmitted quasi particles is opposite.



An incoming electron at the left interface yields the boundary condition

$$\psi_e(\pi - \theta) + r_{ee}^l \psi_e(\theta) + r_{eh}^l \psi_h(\pi - \theta) = t_{ee}^l \psi_{Se}(E, \pi - \theta_S) + t_{eh}^l \psi_{Sh}(E, \theta_S). \quad (2.30)$$

Finally, from the incoming hole at the left interface, we obtain

$$\psi_h(\theta) + r_{hh}^l \psi_h(\pi - \theta) + r_{eh}^l \psi_e(\theta) = t_{he}^l \psi_{Se}(E, \pi - \theta_S) + t_{hh}^l \psi_{Sh}(E, \theta_S). \quad (2.31)$$

Solving this system of equations, we find that the reflection coefficients from electron to electron (r_{ee}) and from hole to hole (r_{hh}) are equal. However, they differ for the left and right interface. They are given by

$$r_{ee}^r = r_{hh}^r = \frac{2e^{i\theta}(e^{i\theta} - e^{i\theta_S})(1 + e^{i(\theta+\theta_S)})\sqrt{E^2 - \Delta^2}}{(1 + e^{2i\theta})(1 + e^{2i\theta_S})E + (1 - e^{2i\theta} - e^{2i\theta_S} + 4e^{i(\theta+\theta_S)} + e^{2i(\theta+\theta_S)})\sqrt{E^2 - \Delta^2}}, \quad (2.32)$$

$$r_{ee}^l = r_{hh}^l = \frac{2(e^{-i(\theta-\theta_S)} + e^{2i\theta_S} - e^{i(\theta+\theta_S)} - 1)\sqrt{E^2 - \Delta^2}}{(1 + e^{2i\theta})(1 + e^{2i\theta_S})E + (1 - e^{2i\theta} - e^{2i\theta_S} + 4e^{i(\theta+\theta_S)} + e^{2i(\theta+\theta_S)})\sqrt{E^2 - \Delta^2}}. \quad (2.33)$$

The reflection coefficients from electron to hole (r_{eh}) and from hole to electron (r_{he}) are

$$\begin{aligned} r_{eh}^r &= -e^{i\theta} X, & r_{eh}^l &= e^{-i\theta} X, \\ r_{he}^r &= e^{i\theta} X, & r_{he}^l &= -e^{-i\theta} X, \end{aligned} \quad (2.34)$$

with

$$X = \frac{\Delta \cos \theta \cos \theta_S}{E \cos \theta \cos \theta_S + \sqrt{E^2 - \Delta^2}(1 - \sin \theta \sin \theta_S)}. \quad (2.35)$$

From the relations given by Eq. (C.2), we see a difference between scattering at the right and left interface. However, substituting $\theta \rightarrow \pi - \theta$ at the left interface, we find the same results as for the right interface, as a result of the different orientation. Hence, scattering at the right and the left interface is the same, which is what we would expect, since there is no physical difference between the two.

The minus sign difference between r_{eh} and r_{he} on the other hand is a real difference, which is crucial here:

$$\boxed{r_{eh} = -r_{he}}. \quad (2.36)$$

We chose the names of these coefficients for convenience, but what they actually represent are the Andreev coefficients a_n that we have seen in the previous sections. We use that $a_n \equiv r_{eh}$. This implies that when we consider holes, we get a minus sign in front of our Andreev coefficient a_n . We obtain

$$\begin{bmatrix} B_n \\ C_n \end{bmatrix} = S_e \begin{bmatrix} \delta_{n0} + a_{2n} A_n \\ a_{2n+1} D_n \end{bmatrix} \quad S_e = \begin{bmatrix} r & t \\ t & -r^* t / t^* \end{bmatrix}, \quad (2.37)$$

$$\begin{bmatrix} A_n \\ D_{n-1} \end{bmatrix} = S_h \begin{bmatrix} -a_{2n} B_n \\ -a_{2n-1} C_{n-1} \end{bmatrix} \quad S_h = S_e^*. \quad (2.38)$$

As can be seen from Fig 2.9, we assume that regions we are considering (TI and STI) have the same Fermi surface. This implies that we have to take the angles the same ($\theta = \theta_S$). The electron to hole and hole to electron coefficients reduce to

$$\begin{aligned} r_{eh}^r &= -e^{i\theta_S} \frac{\Delta}{E + \sqrt{E^2 - \Delta^2}}, & r_{eh}^l &= e^{-i\theta_S} \frac{\Delta}{E + \sqrt{E^2 - \Delta^2}}, \\ r_{he}^r &= e^{i\theta_S} \frac{\Delta}{E + \sqrt{E^2 - \Delta^2}}, & r_{he}^l &= -e^{-i\theta_S} \frac{\Delta}{E + \sqrt{E^2 - \Delta^2}}, \end{aligned} \quad (2.39)$$

which is just the standard Andreev coefficient multiplied by an angle dependent factor. This is the same as how the superconducting phase is normally taken into account (which we neglected in this model), which means that the angle dependency acts as a phase.

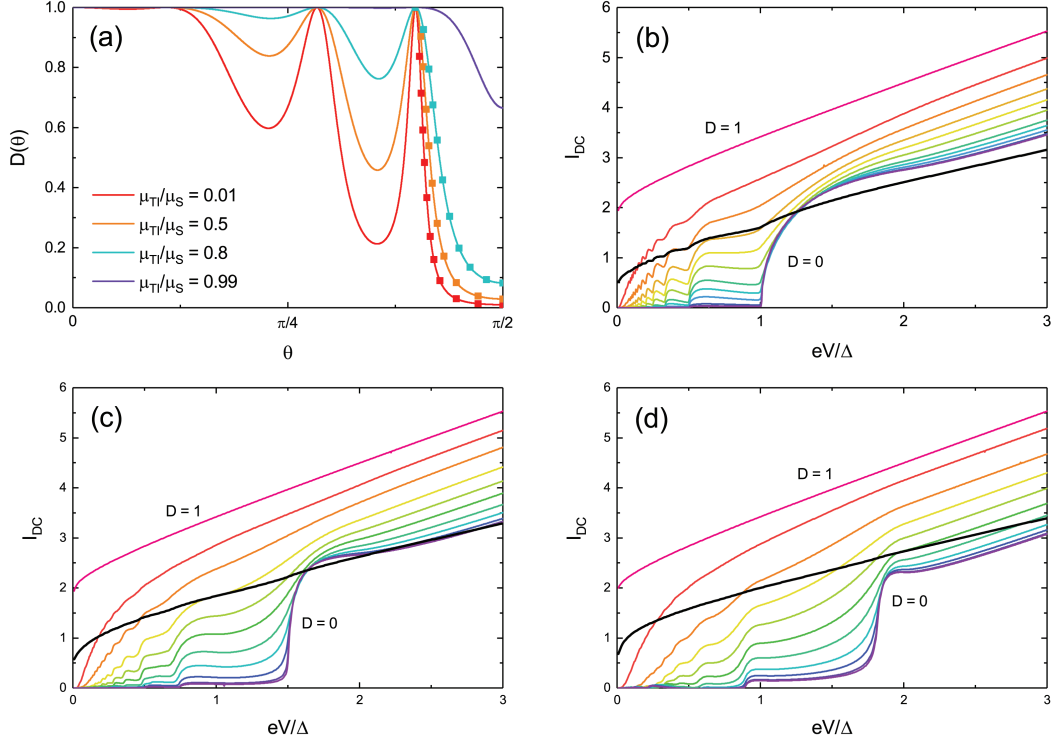


Figure 2.13: (a) Angle dependent transparency $D(\theta) = 1 - |r|^2$ for different values of the Fermi surface mismatch μ_{TI}/μ_S , for $k_FL = 10$. $D = 1$ corresponds to the fully transparent case, while $D = 0$ represents the reflective limit. The squares denote the values of D for which the current in the other panels is plotted. The angle-resolved (colour) and angle-averaged DC current (black) as a function of bias voltage for (b) $\mu_{TI}/\mu_S = 0.01$, (c) $\mu_{TI}/\mu_S = 0.5$ and (d) $\mu_{TI}/\mu_S = 0.8$.

2.4.3 The DC current

In the 2D case, the recurrence relations (2.14) and (2.15) still hold. The DC current is a function of the angle θ , the ratio of chemical potentials μ_{TI}/μ_S (which is effectively the Fermi surface mismatch) and of the scattering length k_FL . Eventually, we will consider the angle-averaged current, which is no longer a function of θ (it is integrated out), but first we will focus on the effect of θ as well.

We keep the length constant at $k_FL = 10$. For this length, the reflection probability $R = |r|^2$ oscillates as a function of θ (Fig. 2.13a). The longer the length, the more oscillations occur (Fabry-Perot). Therefore, considering the current as a function of the angle θ is meaningless. Instead, we display it as a function of the transparency $D = 1 - R$.

The Fermi surface mismatch μ_{TI}/μ_S is taken between 0.01 (Fig 2.13b) and 0.8 (Fig 2.13d). Theoretically, the ratio can become larger than 1, in which case a Brewster angle will be introduced. This implies that for some angles, there are no available states, so they do not contribute to the current. In experiments however, μ_S is usually much larger than μ_{TI} , which is why we focus on values between 0 and 1.

In the first case, where $\mu_{TI}/\mu_S = 0.01$ (Fig 2.13b), the Fermi surface of the TI is much smaller than the Fermi surface of the S. Due to the mismatch, the transport is very limited and becomes quasi-one dimensional. Therefore, the corresponding graphs look very much like the 1D S/TI/S junction from Fig. 2.6. Increasing the μ_{TI}/μ_S ratio, the full spectrum shifts to the right.

In order to determine how much it shifts exactly, we can calculate where we expect the singularities (corresponding to the oscillations) to be located. We are still dealing with recurrence relation (2.14), which implies singularities occur when $1 + a_q^2 = 0$, which is equivalent to $a_q = \pm i$. Recalling the Andreev coefficients from Eq. (2.39), we obtain

$$a_q = \frac{\varepsilon + qeV - \text{sgn}(\varepsilon + qeV)\sqrt{(\varepsilon + qeV)^2 - \Delta^2}}{\Delta} e^{i\theta_S} = \pm i. \quad (2.40)$$

Doing some rewriting and squaring the equation, we obtain

$$\begin{aligned} (\varepsilon + qeV)^2 - \Delta^2 &= (\varepsilon + qeV \pm i\Delta e^{-i\theta_S})^2 \\ &= (\varepsilon + qeV)^2 \pm 2i\Delta(\varepsilon + qeV)e^{-i\theta_S} - \Delta^2 e^{-2i\theta_S}. \end{aligned}$$

The $(\varepsilon + qeV)^2$ terms cancel. We divide by Δ and sort the terms. What remains is

$$\pm 2i(\varepsilon + qeV)e^{-i\theta_S} = \Delta(1 - e^{-2i\theta_S}).$$

We can rewrite this as

$$\varepsilon + qeV = \pm \frac{\Delta(1 - e^{-2i\theta_S})}{2ie^{-i\theta_S}} = \pm \Delta \sin \theta_S,$$

where we used that $(1 - e^{-2i\theta_S})/e^{-i\theta_S} = e^{i\theta_S} - e^{-i\theta_S} = 2i \sin \theta_S$. Setting $\varepsilon = \pm \Delta$, we get

$$eV = \frac{\pm \Delta(1 + \sin \theta_S)}{q} = \pm \frac{\Delta}{q} \left(1 + \frac{\mu_{TI}}{\mu_S} \sin \theta \right), \quad q \in \mathbb{N}. \quad (2.41)$$

It follows directly that the oscillations in eV are shifted by the Fermi surface mismatch μ_{TI}/μ_S . Finally, we note the slope of the current becomes concave for μ_{TI}/μ_S large. This was also observed in the S/N/S case in Fig. 2.4, which indicates the spectrum is approaching the conventional case.

2.4.4 Angle integration

At the beginning of Section 2.4, we argued that the experimentally observed current through a S/TI/S junction is the current integrated over all possible angles. The integrand is the angle resolved current $I_0(eV, \theta)$, given by Eq. (2.11). Averaging over the angle is done by

$$I_0(eV) = \frac{1}{\pi} \int_{-\pi/2}^{\pi/2} I_0(eV, \theta) \cos \theta \, d\theta. \quad (2.42)$$

The angle-averaged DC current is shown in black in Fig. 2.13. These graphs all look quite smooth and similar. Structures from the MAR are hardly visible. This is why it is difficult to observe MAR experimentally. It is remarkable that the black curve lies at the lower side of the spectrum of I-V curves (in the case of $\mu_{TI}/\mu_S = 0.01$ the black curve lies partly under the coloured curves). This has two reasons. Firstly, the angle averaging is scaled by a factor $\cos \theta$ which is always less than, or equal to, 1. Secondly, we integrate the angle from $-\pi/2$ to $\pi/2$. The graphs in Fig. 2.13 are taken for positive angles. The graphs for negative angles are slightly different, which is shown in the case of $\mu_{TI}/\mu_S = 0.5$ in Fig. 2.14. We recall that there are two angle dependent processes; the scattering in the middle region and Andreev reflection at the interfaces. The transparency of the scatter region, $D(\theta)$, is completely symmetric around θ . Hence, the difference for positive and negative θ is caused by the Andreev reflection, as a result of the Fermi surface mismatch. The current is symmetric with respect to the applied voltage V .

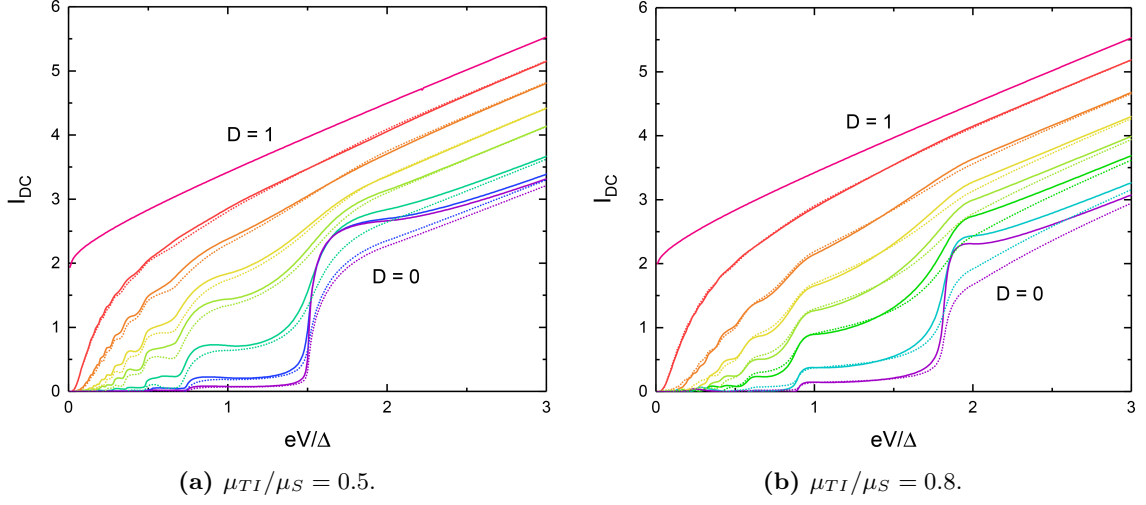


Figure 2.14: Angle resolved DC current from Fig. 2.13c for positive (solid) and negative (dotted) values of θ . For $k_F L = 10$.

2.4.5 Bound state energy

In the one dimensional S/TI/S junction introduced by Badiane et al. [41], it was shown that there is a bound state at zero energy, which was attributed to the existence of a Majorana bound state in this system. In two dimensions, we can show that we can have a bound state at nonzero energy as well, depending on the angle of the incident particle, and on the Fermi surface mismatch between the topological insulator and the superconductor.

In the original BTK formalism [47], the electron and hole wave functions amplitudes u and v were defined as

$$u^2 = 1 - v^2 = \frac{1}{2} \left(1 + \frac{\sqrt{\varepsilon^2 - \Delta^2}}{\varepsilon} \right) = \frac{\varepsilon + \sqrt{\varepsilon^2 - \Delta^2}}{2\varepsilon}, \quad (2.43)$$

such that the ratios between u and v are

$$\frac{u}{v} = \frac{\varepsilon + \sqrt{\varepsilon^2 - \Delta^2}}{\Delta}, \quad \frac{v}{u} = \frac{\varepsilon - \sqrt{\varepsilon^2 - \Delta^2}}{\Delta}. \quad (2.44)$$

For our bound state calculation, we are interested in the bound state inside the STI. We consider the left STI/TI interface separately. We take the electron to hole reflection coefficient r_{eh} from Eq. (2.39) and rewrite it in terms of u and v as

$$r_{eh} = e^{-i\theta_S} \frac{\Delta}{\varepsilon + \sqrt{\varepsilon^2 - \Delta^2}} = e^{-i\theta_S} \frac{\varepsilon - \sqrt{\varepsilon^2 - \Delta^2}}{\Delta} = e^{-i\theta_S} \frac{v}{u} = \frac{v}{ue^{i\theta_S}}. \quad (2.45)$$

From this we can conclude that, compared to the conventional case with the normal metal, u gets an additional factor $e^{i\theta_S}$ and v remains the same. We note that changing the orientation of the two materials (i.e. the right TI/STI interface), gives the same result.

Using this observation, we can rewrite the wave function in the STI from Eq. (2.27) as

$$\psi_{Se}(\varepsilon, \theta_S) = \frac{1}{\sqrt{2}} \begin{bmatrix} u \\ ue^{i\theta_S} \\ -ve^{i\theta_S} \\ v \end{bmatrix}, \quad \psi_{Sh}(\varepsilon, \theta_S) = \frac{1}{\sqrt{2}} \begin{bmatrix} v \\ ve^{i\theta_S} \\ -ue^{i\theta_S} \\ u \end{bmatrix}. \quad (2.46)$$

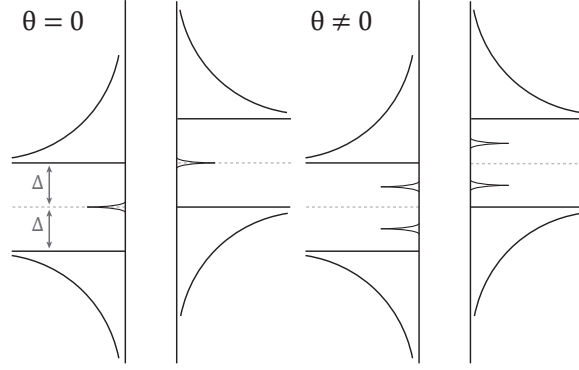


Figure 2.15: Subgap states in the density of states for perpendicular incidence (left) and incidence under an angle (right).

Following Nagato et al [48], we can construct an artificial system consisting of a STI for $x < 0$ and an infinitely high barrier located at $x = 0$. This causes a completely reflective interface, which implies that the wave function has to be set to zero at $x = 0$. We wave function is a superposition of an left-going electron (with momentum $-k$ and angle $\pi - \theta_S$) and a right-going hole (with momentum $+k$ and angle θ_S). The two states with arbitrary coefficients c_+ and c_- . We are not interested in them, since we will eliminate them later on. The completely reflective boundary condition is

$$\frac{c_+}{\sqrt{2}} \begin{bmatrix} u \\ -ue^{-i\theta_S} \\ ve^{-i\theta_S} \\ v \end{bmatrix} + \frac{c_-}{\sqrt{2}} \begin{bmatrix} v \\ ve^{i\theta_S} \\ -ue^{i\theta_S} \\ u \end{bmatrix} = \begin{bmatrix} 0 \\ 0 \\ 0 \\ 0 \end{bmatrix}. \quad (2.47)$$

We note that the system of equations generated by the first two rows is the same as the system resulting from the third and fourth row. Eliminating the c_+ and c_- coefficients, we obtain the relation between u and v

$$u^2 e^{2i\theta_S} + v^2 = 0,$$

which is equivalent to

$$r_{eh} = \frac{ue^{i\theta_S}}{v} = \pm i.$$

This is almost the same relation that we found in Eq. (2.40), when we investigated the poles of the recurrence relation. We are interested in the bound state energy. In order to have a bound state, we must have $|\varepsilon| < \Delta$. Using the definition of r_{eh} from Eq. (2.45), with $|\varepsilon| < \Delta$, and setting it equal to $\pm i$, we get

$$e^{-i\theta_S} \frac{\Delta}{\varepsilon + i\sqrt{\Delta^2 - \varepsilon^2}} = \pm i.$$

Solving for ε , we obtain the bound state energy

$$\varepsilon = \pm \Delta \sin \theta_S. \quad (2.48)$$

We note that for perpendicular incidence (i.e. $\theta = 0$ and therefore, $\theta_S = 0$), the bound state is located at zero energy, just as Badiane et al. found for their one dimensional case. [41] We find that for incidence under an angle, the bound state splits into two bound states that go away from zero energy. This is illustrated in Fig. 2.15.

The bound state spectrum from Eq. (2.48) is almost the same as the bound states found in chiral p -wave superconductors. [49, 50, 51, 52, 53, 54, 55] However, in these cases, there is only one

bound state, while we find two of them. Which bound state is found depends on the chirality of the superconductor, i.e. in which direction the conserved momentum k_y is defined.

The last thing that is left to do is to figure out whether we truly have two bound states in our system, or whether one of them is invalid. In the previous section, we showed that the current is asymmetric with respect to the incoming angle θ , which might be an indication for the presence of only one bound state. The simple infinite boundary condition that we used here is probably too simplistic to determine which one of the obtained bound states (if any) is invalid. A more thorough approach would be to follow the edge state calculations by Tkachov. [25]

Numerical methods

The goal of the previous section was to calculate the current through S/N/S and S/TI/S junctions, in one or two dimensions. This section describes the numerical methods that were used to obtain these results. The current is defined as the integral over the sum of all reflection probabilities. There are two types of reflections we consider: the regular reflections B_n and the Andreev reflections A_n . The B_n coefficients depend on the previous two reflections and can therefore be described by three-term recurrence relations. These recurrence relations have two different solutions and finding the desired one numerically is not trivial. This is a well-known issue in calculating the famous Bessel functions. We briefly go over the theory of the two solutions for the recurrence relation (Section 3.1.1) and investigate the behaviour for $n \rightarrow \infty$ to gain more insight in what we are working with (Section 3.1.2). Different algorithms for solving recurrence relations are discussed in Sections 3.1.3 to 3.3. The Andreev reflection coefficients A_n only depend on the previous Andreev reflection and are described by two-term recurrence relations. The way to solve them is considered in Section 3.2. After the reflection probabilities B_n and A_n are obtained, we have to integrate over them to find the current. This is done using an adaptive Simpson method (Section 3.4.1). The integrands contain many singularities. Section 3.4.2 describes a simple, yet effective method to avoid them. In the two dimensional case, an angle dependency was introduced (Section 2.4). The relevant physical quantity is the average over the various angles. The numerical averaging is briefly discussed in Section 3.5.

3.1 Three-term recurrence relations

3.1.1 Minimal solutions

A three-term linear recurrence relation can be written as

$$y_{n+1} + \gamma_n y_n + \chi_n y_{n-1} = 0, \quad n \in \mathbb{N}, \quad (3.1)$$

where γ_n and χ_n are sequences of real or complex numbers and $\chi_n \neq 0$. Since this is a second order equation, it has two linearly independent solutions f_n and g_n . Hence, the general solution of Eq. (3.1) can be spanned by a pair of linearly independent solutions f_n and g_n , i.e.

$$y_n = a f_n + b g_n. \quad (3.2)$$

Only one of them, say f_n , is the solution we are trying to find. The other function, g_n , may or may not diverge with increasing n . Therefore, we are interested in a pair of solutions (f_n, g_n) with the property [56, 57]

$$\lim_{n \rightarrow \infty} \frac{f_n}{g_n} = 0. \quad (3.3)$$

We can see that f_n is “minimal at infinity” and therefore, it is referred to as the *minimal* solution. Non-minimal solutions such as g_n are called *dominant* solutions. The minimal solution f_n is unique, whereas dominant solutions are not. To see why the minimal solution is unique, we assume there exist two minimal solutions f_n and f'_n . This would imply that both f_n/f'_n and f'_n/f_n have the limit zero as $n \rightarrow \infty$, which is not possible. Since the general solution can be written as a linear combination (Eq. (3.2)), arbitrary multiples of f_n can be added to g_n to generate more dominant solutions (solutions asymptotically proportional to g_n). [56]

In the case of a dominant solution (i.e. $b \neq 0$), Eq. (3.3) implies that

$$\lim_{n \rightarrow \infty} \frac{f_n}{y_n} = 0. \quad (3.4)$$

Suppose we are trying to find the desired solution f_n by setting approximate initial values $y_0 \doteq f_0$ and $y_1 \doteq f_1$ (due to rounding errors) and recurring with infinite precision. We can still obtain a solution which is linearly independent of f_n , due to the g_n component. Let ϵ_r be the relative error, i.e. the absolute error divided by the actual quantity. Because of the relation Eq. (3.4), we find that [56]

$$\epsilon_r = \left| \frac{y_n - f_n}{f_n} \right| \rightarrow \infty \quad \text{as } n \rightarrow \infty, \quad (3.5)$$

which implies that the relative error diverges. Therefore, computing f_n in this simple, straightforward way is not very useful. Instead, to find f_n we have to use backward recursion. This procedure will be explained in Section 3.1.3. Before considering the actual algorithm, it is good to know what we are dealing with. Hence, we will first have a look at the asymptotic behaviour of the solutions g_n and f_n as $n \rightarrow \infty$.

3.1.2 Asymptotic behaviour

We consider again the recurrence relation $y_{n+1} + \gamma_n y_n + \chi_n y_{n-1} = 0$ and assume the coefficients γ_n and χ_n obey the asymptotic structure

$$\gamma_n \sim \gamma n^\alpha, \quad \chi_n \sim \chi n^\beta, \quad \gamma \neq 0, \quad \chi \neq 0, \quad \alpha, \beta \in \mathbb{R}, \quad n \rightarrow \infty. \quad (3.6)$$

Using this structure, we can construct a *Newton-Puiseux* diagram formed by the points $P_0(0, 0)$, $P_1(1, \alpha)$ and $P_2(2, \beta)$, as shown in Fig 3.1.

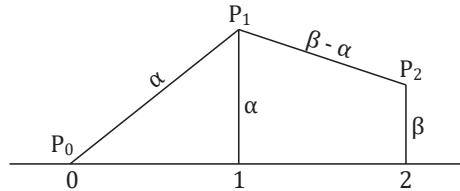


Figure 3.1: Newton-Puiseux diagram.

Perron Kreuser Theorem [56, 57]

(a) If the point P_1 is above the line segment $\overline{P_0P_2}$ (i.e. $\alpha > \beta - \alpha$ or $\beta < 2\alpha$), the recurrence relation (3.1) has two linearly independent solutions g_n and f_n for which

$$\lim_{n \rightarrow \infty} \frac{g_{n+1}}{g_n} \sim -\gamma n^\alpha \quad \text{and} \quad \lim_{n \rightarrow \infty} \frac{f_{n+1}}{f_n} \sim -\left(\frac{\chi}{\gamma}\right) n^{\beta-\alpha} \quad (3.7)$$

and f_n is the minimal solution to (3.1).

(b) If the points P_0, P_1, P_2 are collinear (i.e. $\beta = 2\alpha$), let t_1, t_2 be roots of $t^2 + \gamma t + \chi = 0$ and $|t_1| \geq |t_2|$. Then (3.1) has two linearly independent solutions g_n and f_n , such that

$$\lim_{n \rightarrow \infty} \frac{g_{n+1}}{g_n} \sim t_1 n^\alpha \quad \text{and} \quad \lim_{n \rightarrow \infty} \frac{f_{n+1}}{f_n} \sim t_2 n^\alpha, \quad (3.8)$$

provided $|t_1| > |t_2|$. If $|t_1| = |t_2|$ (in particular, if t_1, t_2 are complex conjugates) then

$$\limsup_{n \rightarrow \infty} \left[\frac{|y_n|}{(n!)^\alpha} \right]^{1/n} = |t_1| \quad (3.9)$$

for all non-trivial solutions of (3.1).

(c) If the point P_1 lies below the line segment $\overline{P_0P_2}$ then

$$\limsup_{n \rightarrow \infty} \left[\frac{|y_n|}{(n!)^{\beta/2}} \right]^{1/n} = \sqrt{|\chi|} \quad (3.10)$$

for all non-trivial solutions of (3.1).

The recurrence relation of interest is

$$D \frac{a_{2n+2} a_{2n+1}}{1 - a_{2n+1}^2} B_{n+1} - \left[D \left(\frac{a_{2n+1}^2}{1 - a_{2n+1}^2} + \frac{a_{2n}^2}{1 - a_{2n-1}^2} \right) + 1 - a_{2n}^2 \right] B_n + D \frac{a_{2n} a_{2n-1}}{1 - a_{2n-1}^2} B_{n-1} = 0, \quad (3.11)$$

where D is the transparency. Since this is a probability, it satisfies $0 \leq D \leq 1$. The Andreev coefficients are defined as $a_n = a(\varepsilon + neV)$, with

$$a(\varepsilon) = \frac{1}{\Delta} \begin{cases} \varepsilon - \operatorname{sgn}(\varepsilon) \sqrt{\varepsilon^2 - \Delta^2} & |\varepsilon| > \Delta, \\ \varepsilon - i \sqrt{\Delta^2 - \varepsilon^2} & |\varepsilon| < \Delta, \end{cases} \quad (3.12)$$

where $i \equiv \sqrt{-1}$. In order to rewrite this relation in the standard form $y_{n+1} + \gamma_n y_n + \chi_n y_{n-1} = 0$, we divide the whole equation by the first term and simplify the result. The coefficients are given by

$$\gamma_n = - \left[\frac{a_{2n+1}}{a_{2n+2}} + \frac{a_{2n}^2 (1 - a_{2n+1}^2)}{a_{2n+2} a_{2n+1} (1 - a_{2n-1}^2)} + \frac{1}{D} \frac{(1 - a_{2n+1}^2)(1 - a_{2n}^2)}{a_{2n+2} a_{2n+1}} \right], \quad (3.13)$$

$$\chi_n = \frac{a_{2n} a_{2n-1} (1 - a_{2n+1}^2)}{a_{2n+2} a_{2n+1} (1 - a_{2n-1}^2)}. \quad (3.14)$$

Using the computer program Wolfram Mathematica, we can find the Taylor expansions for $n \rightarrow \infty$ using the command `Series[func, {n, Infinity, order}]`, where `func` is the function (depending

on \mathbf{n}) and **order** is the order of the expansion. The Taylor expansions for both coefficients are given by

$$\gamma_n = \frac{16n^2}{D} + \frac{8(3+2\varepsilon)n}{D} + \frac{2(2+D+6\varepsilon+2\varepsilon^2)}{D} + \mathcal{O}\left(\frac{1}{n}\right), \quad (3.15)$$

$$\chi_n = 1 + \frac{2}{n} + \frac{3-2\varepsilon}{2n^2} + \mathcal{O}\left(\frac{1}{n^3}\right), \quad (3.16)$$

hence the asymptotic behaviour of the coefficients can be described by

$$\gamma_n \sim \frac{16}{D}n^2, \quad \chi_n \sim 1. \quad (3.17)$$

It is remarkable that in the first approximation, the coefficients are independent of the energy ε . This can be interpreted as the spectrum of reflections becoming continuous for $n \rightarrow \infty$. Therefore, it does not matter which value of the energy we consider.

The corresponding Newton-Puiseux diagram has slopes $+2$ and -2 . Hence, by the Perron Kreuser Theorem, part (a), there are two solutions with different asymptotic behaviour

$$\lim_{n \rightarrow \infty} \frac{g_{n+1}}{g_n} \sim -\frac{16n^2}{D}, \quad \lim_{n \rightarrow \infty} \frac{f_{n+1}}{f_n} \sim -\frac{D}{16n^2}, \quad n \rightarrow \infty. \quad (3.18)$$

A well-known recurrence relation with similar stability issues is the generation of Bessel functions. In that case, the dominant solution grows with $\sim n$, while the minimal solution decreases with $\sim 1/n$. [56] The dominant solution in (3.18) is even more dominant than the one in the Bessel functions case. This implies that we have to treat it carefully.

3.1.3 Backward recurrence algorithm

Assume we want to compute the sequence

$$f_0, f_1, \dots, f_N,$$

where N is a large, positive integer. We start the backward recurrence for a large $\nu \gg N$ and generate the sequence y_n , $n = \nu, \nu - 1, \dots, 0$. Since f_n is minimal, the ratios y_N/y_{N-1} will approach the ratios of the minimal solution f_N/f_{N-1} . Since the procedure is based on ratios, we define

$$r_n = \frac{f_{n+1}}{f_n}. \quad (3.19)$$

The use of ratios has the additional advantage that the risk of overflow in the numerical calculation is minimized. By plugging f_{n+1} and f_n into (3.19), we find that we can write the ratio r_n as a continued fraction

$$r_{n-1} = \frac{-\chi_n}{\gamma_n - \frac{\chi_{n+1}}{\gamma_{n+1} - \frac{\chi_{n+2}}{\gamma_{n+2} - \dots}}}, \quad n = 1, 2, 3, \dots \quad (3.20)$$

Suppose r_n is known for some value $\nu \geq N$. Then, the ratios r_n can be generated backwards for $0 \leq n < \nu$ by

$$r_{n-1} = \frac{-\chi_n}{\gamma_n + r_n}, \quad n = \nu, \nu - 1, \dots, 1. \quad (3.21)$$

Another consequence of working with ratios is that the solution is defined up to a normalisation constant. The most general normalisation condition can be obtained by defining a sum of minimal solutions

$$s = \sum_{m=0}^{\infty} \lambda_m f_m, \quad (3.22)$$

where $s \neq 0$ and $s, \lambda_0, \lambda_1, \dots$ are given quantities and the series converges. The simplest case one can imagine is $\lambda_m = 0$ for $m > 0$, which means that the condition reduces to prescribing only f_0 . The advantage of using the infinite series is that it does not require any value of f_n to be known. Since f_n is unique (Section 3.1.1), we will converge to f_n anyway.

In order to conveniently use s simultaneously with our recurrence, we define

$$s_n = \frac{1}{f_n} \sum_{m=n+1}^{\infty} \lambda_m f_m. \quad (3.23)$$

Substituting our definition of the ratios r_n from (3.19), we can rewrite s_n as

$$\begin{aligned} s_{n-1} &= \frac{1}{f_{n-1}} \sum_{m=n}^{\infty} \lambda_m f_m = \frac{1}{f_{n-1}} \left(\lambda_n f_n + \sum_{m=n+1}^{\infty} \lambda_m f_m \right) \\ &= \lambda_n r_{n-1} + r_{n-1} \left(\frac{1}{f_n} \sum_{m=n+1}^{\infty} \lambda_m f_m \right) \\ &= r_{n-1} (\lambda_n + s_n), \end{aligned} \quad n = \nu, \nu - 1, \dots, 1. \quad (3.24)$$

In particular, for $n = 0$, we find

$$s_0 = \frac{1}{f_0} \sum_{m=1}^{\infty} \lambda_m f_m = \frac{1}{f_0} (s - \lambda_0 f_0), \quad (3.25)$$

and so

$$f_0 = \frac{s}{\lambda_0 + s_0}, \quad (3.26)$$

which gives the initial value of the solution. The remaining values can be obtained from

$$f_n = r_{n-1} f_{n-1}, \quad n = 1, 2, \dots, N. \quad (3.27)$$

Up until now, we have been discussing an infinite continued fraction r_{n-1} and an infinite series s_n . In the actual algorithm, the use of infinite fractions and series is not possible, so we truncate them at a value $\nu \geq n$. We define the truncated continued fraction $r_{n-1}^{(\nu)}$ and the truncated series $s_n^{(\nu)}$ as

$$r_{\nu}^{(\nu)} = 0, \quad r_{n-1}^{(\nu)} = \frac{-\chi_n}{\gamma_n - \frac{\chi_{n+1}}{\gamma_{n+1} - \frac{\chi_{n+2}}{\gamma_{n+2} - \dots \chi_{\nu}/\gamma_{\nu}}}}, \quad 1 \leq n \leq \nu, \quad (3.28)$$

$$s_{\nu}^{(\nu)} = 0, \quad s_n^{(\nu)} = \sum_{m=n+1}^{\nu} \lambda_m r_n^{(\nu)} r_{n+1}^{(\nu)} \dots r_{m-1}^{(\nu)}, \quad 0 \leq n < \nu. \quad (3.29)$$

Since (3.21) and (3.24) still hold for the truncated case, we can rewrite this as

$$r_{\nu}^{(\nu)} = 0, \quad r_{n-1}^{(\nu)} = \frac{-\chi_n}{\gamma_n - r_n^{(\nu)}}, \quad n = \nu, \nu - 1, \dots, 1, \quad (3.30)$$

$$s_{\nu}^{(\nu)} = 0, \quad s_{n-1}^{(\nu)} = r_{n-1}^{(\nu)} (\lambda_n + s_n^{(\nu)}), \quad n = \nu, \nu - 1, \dots, 1. \quad (3.31)$$

The solution $f_n^{(\nu)}$ can then be obtained via

$$f_0^{(\nu)} = \frac{s}{\lambda_0 + s_0^{(\nu)}}, \quad f_n^{(\nu)} = r_{n-1}^{(\nu)} f_{n-1}^{(\nu)}, \quad n = 1, 2, \dots, N. \quad (3.32)$$

We can now construct an algorithm for computing $f_n^{(\nu)}$ using (3.30)-(3.32). The original equations (with infinite fractions and infinite series) gave the exact solutions f_n . The quantities $f_n^{(\nu)}$ are (at best) approximations to f_n . The larger the value of ν , the better the approximation. However, we do not know how large ν should be. Therefore, we keep computing $f_n^{(\nu)}$ for increasing values of ν until the approximation is within the desired accuracy.

The desired accuracy means the number of digits that we take into account. An accuracy of x digits corresponds to a tolerance $\epsilon = 10^{-x}$.

Backward recurrence algorithm [56]

Input: ϵ (tolerance), N , λ_n , s .

Output: sequence $f_0^{(\nu)}, f_1^{(\nu)}, \dots, f_N^{(\nu)}$.

1. Select an integer $\nu \geq N$. Set $\phi_n^{(\nu)} = 0$ for $n = 0, 1, \dots, N$.
2. Calculate $f_n^{(\nu)}$ as follows:
 Set $r_\nu^{(\nu)} = 0$, $s_\nu^{(\nu)} = 0$.
 For $n = \nu, \nu - 1, \dots, 1$

$$r_{n-1}^{(\nu)} = \frac{-\chi_n}{\gamma_n - r_n^{(\nu)}},$$

$$s_{n-1}^{(\nu)} = r_{n-1}^{(\nu)} (\lambda_n + s_n^{(\nu)}).$$
 Set $f_0^{(\nu)} = \frac{s}{\lambda_0 + s_0^{(\nu)}}$.
 For $n = 1, 2, \dots, N$

$$f_n^{(\nu)} = r_{n-1}^{(\nu)} f_{n-1}^{(\nu)}.$$
3. If $|f_n^{(\nu)} - \phi_n^{(\nu)}| > \epsilon$
 Set $\phi_n^{(\nu)} = f_n^{(\nu)}$,
 Set $\nu = \nu + 5$,
 Repeat from step 2.

Step 3 can be executed by creating a while loop around step 2, with the condition “While $|f_n^{(\nu)} - \phi_n^{(\nu)}| > \epsilon$ ”.

The algorithm described here is written in the most general form. Note that if we want to switch from the S/N/S case to the S/TI/S case, the only thing we have to change are the coefficients γ_n and χ_n .

Testing the algorithm

Before actually implementing the algorithm for our coefficients, it was tested using the simple case of the Bessel functions. The Bessel functions of the first type $J_n(x)$ (the minimal solution) and the Bessel functions of the second type $Y_n(x)$ (the dominant solution) both obey the same recurrence relation

$$y_{n+1} - \frac{2n}{x}y_n + y_{n-1} = 0. \quad (3.33)$$

The exact values can be found using Matlab's Bessel function `besselj(n,x)`. For comparison, we start by calculating the Bessel function using a simple forward recurrence algorithm. We give the values $J_1(1)$ and $J_2(1)$ up to ten decimals as initial conditions. The values $y_{n+1} = (2n/x)y_n - y_{n-1}$ were calculated in a forward for-loop. Values obtained by testing the algorithm are shown in Table 3.1. We can see that already after one iteration of the forward algorithm, the solution starts growing and converges to the dominant solution.

For the backward algorithm, we set the coefficients $\gamma_n = -2n/x$ and $\chi_n = 1$ and run the algorithm described earlier in this section. We first tested the algorithm by setting f_0 equal to the first ten decimals of the exact value $J_1(1)$ and ignoring Eq. (3.26). We checked what happens when we varied the number of iterations ν . Comparing $\nu = 200$ and $\nu = 100$, the value of y_{100} is the same up to the first three decimals.

n	Exact value	Forward recurrence	Backward recurrence $\nu = 200, f_0 = J_1(1)$
1	$4.4005058574 \cdot 10^{-1}$	$4.4005058574 \cdot 10^{-1}$	$4.4005058574 \cdot 10^{-1}$
2	$1.1490348493 \cdot 10^{-1}$	$1.1490348493 \cdot 10^{-1}$	$1.1490348493 \cdot 10^{-1}$
3	$1.9563353982 \cdot 10^{-2}$	$2.2865793501 \cdot 10^1$	$1.9563353982 \cdot 10^{-2}$
4	$2.4766389641 \cdot 10^{-3}$	$4.5502929067 \cdot 10^3$	$2.4766389641 \cdot 10^{-3}$
5	$2.4975773021 \cdot 10^{-4}$	$9.0550828844 \cdot 10^5$	$2.4975773021 \cdot 10^{-4}$
6	$2.0938338002 \cdot 10^{-5}$	$1.8019614940 \cdot 10^8$	$2.0938338002 \cdot 10^{-5}$
...
20	$3.8735939985 \cdot 10^{-25}$	$2.7522544087 \cdot 10^{40}$	$3.8735030084 \cdot 10^{-25}$
...
100	$8.4318287896 \cdot 10^{-189}$	$2.2281000524 \cdot 10^{224}$	$8.4318287895 \cdot 10^{-189}$

n	Backward recurrence $\nu = 100, f_0 = J_1(1)$	Backward recurrence $\lambda_1 = 1, s = 0.4401$	Backward recurrence $\lambda_{2m} = 2, s = 0.0396$
1	$4.4005058574 \cdot 10^{-1}$	$4.4010000000 \cdot 10^{-1}$	$4.3972591478 \cdot 10^{-1}$
2	$1.1490348493 \cdot 10^{-1}$	$1.1491638770 \cdot 10^{-1}$	$1.1481879870 \cdot 10^{-1}$
3	$1.9563353982 \cdot 10^{-2}$	$1.9565550795 \cdot 10^{-2}$	$1.9548920067 \cdot 10^{-2}$
4	$2.4766389641 \cdot 10^{-3}$	$2.4769170714 \cdot 10^{-3}$	$2.4748116907 \cdot 10^{-3}$
5	$2.4975773021 \cdot 10^{-4}$	$2.4978577606 \cdot 10^{-4}$	$2.4957345803 \cdot 10^{-4}$
6	$2.0938338002 \cdot 10^{-5}$	$2.0940689215 \cdot 10^{-5}$	$2.0922889619 \cdot 10^{-5}$
...
20	$3.8735030084 \cdot 10^{-25}$	$3.8739372758 \cdot 10^{-25}$	$3.8706451236 \cdot 10^{-25}$
...
100	$8.4316200706 \cdot 10^{-189}$	$8.4327756184 \cdot 10^{-189}$	$8.4256077549 \cdot 10^{-189}$

Table 3.1: The Bessel function of the first kind $J_n(1)$; its exact value, the value obtained by a simple forward recurrence and values from the backward recurrence algorithm using different numbers of iterations ν and different normalisation conditions.

Next, we wanted to implement Eq. (3.26), for which we have to choose values for λ_n and s . We kept ν constant at 200. We started by the simplest case where we put $s = 1$, $\lambda_0 = 1$ and $\lambda_m = 0$, for $m > 0$. We noticed that the sequence went down at the same rate as the exact Bessel function, however, the value for $n = 100$ was slightly off (we found $y_{100} = 1.916 \cdot 10^{-188}$). This is a consequence of randomly setting the value of s equal to 1. To fix this, we took the exact value, $J_{100}(1)$ and divided it by the obtained value y_{100} , from which we get $s = 0.4401$. By using this value, we found a new approximation for the Bessel function which is already much closer to the exact value.

Finally, we wanted to use the normalising sum from Eq. (3.22). We followed Section 5 from Ref. [56], where $a = 0$ (a parameter we did not use) and x is real. In this case, the normalisation condition was chosen as $\lambda_{2m} = 2$ and 0 otherwise. Again, we started with $s = 1$, from which we obtained $y_{100} = 9.8183 \cdot 10^{-188}$, which is again slightly off. By doing the same trick as before, we obtained $s = 0.0396$, which gave results that are much closer to the exact values.

In these examples, we only specified s up to four decimals. By increasing the number of decimals, the values would be even closer to the exact values of the Bessel function. An important observation is that we used the exact values of the Bessel function to obtain the value for s . This exact value could, in general, be unknown. In Ref. [56], the so-called Sonine's formula is used to estimate s . The Sonine's formula is based on the properties of the Bessel functions, which means that it still assumes that something is known about the desired solution. We do not have a similar formula for our case, so this method is not very useful either.

3.1.4 The non-homogeneous case

Up until now, we have considered only the homogeneous recurrence relation (3.11), where the right hand side of the equation is equal to zero. Suppose we have a non-homogeneous recurrence relation

$$y_{n+1} + \gamma_n y_n + \chi_n y_{n-1} = f(n), \quad (3.34)$$

where $f(n)$ solely depends on n . Its solution is the sum of the homogeneous recurrence, y_n^h , and a particular solution, y_n^p , i.e.

$$y_n = y_n^h + y_n^p. \quad (3.35)$$

The homogeneous solution can be found by setting $f(n)$ to zero and solving the recurrence relation using the backward recurrence algorithm from the previous section. In order to obtain a particular solution, we guess an Ansatz in the same form as $f(n)$ with unknown coefficients. By simply substituting the Ansatz into the recurrence (3.34), we obtain the coefficients. If all coefficients turn out to be zero, we have to take a different Ansatz. Since the particular solution is based on an Ansatz, it is not unique.

The system under consideration has a source term described by a Kronecker δ -function. The non-homogeneous recurrence relation is given by

$$D \frac{a_{2n+2} a_{2n+1}}{1 - a_{2n+1}^2} B_{n+1} - \left[D \left(\frac{a_{2n+1}^2}{1 - a_{2n+1}^2} + \frac{a_{2n}^2}{1 - a_{2n-1}^2} \right) + 1 - a_{2n}^2 \right] B_n + D \frac{a_{2n} a_{2n-1}}{1 - a_{2n-1}^2} B_{n-1} = -\sqrt{1 - D} \delta_{n0}. \quad (2.8)$$

Similar to Section 3.1.2, we divide the full equation by the first term and write it in a compact manner as

$$y_{n+1} + \gamma_n y_n + \chi_n y_{n-1} = \zeta_n \delta_{n0}, \quad (3.36)$$

where γ_n and χ_n are given by Eqs. (3.13) and (3.14), respectively. The coefficient on the right hand side is defined as

$$\zeta_n = -\frac{\sqrt{1 - D}}{D} \frac{1 - a_{2n+1}^2}{a_{2n+2} a_{2n+1}}. \quad (3.37)$$

Since the non-homogeneous part is given by $f(n) = \zeta_n \delta_{n0}$, we take our Ansatz to be of the same form, i.e.

$$y_n^p = c \delta_{n0},$$

where c is the coefficient that we have to find. Substituting the Ansatz into Eq. (3.36), we obtain

$$c(\delta_{n+1,0} + \gamma_n \delta_{n0} + \chi_n \delta_{n-1,0}) = \zeta_n \delta_{n0}.$$

If $n = 0$, we find that $c = \zeta_0/\gamma_0$. The Ansatz from (3.1.4) vanishes when $n \neq 0$. Hence, the particular solution becomes

$$y_n^p = \frac{\zeta_n}{\gamma_n} \delta_{n0}. \quad (3.38)$$

Using the expressions for γ_n and ζ_n given by Eqs. (3.13) and (3.37), we can simplify the coefficient to

$$\frac{\zeta_0}{\gamma_0} = \frac{\sqrt{1-D}}{D} \left[\frac{1}{1-a_1^2} + \frac{a_0^2}{(1-a_{-1}^2)} + \frac{(1-a_0^2)}{D} \right]^{-1}. \quad (3.39)$$

3.2 Two-term recurrence relations

After the B_n coefficients are obtained, we can use them to calculate the A_n coefficients. The A_n coefficients are described by the two-term recurrence

$$A_{n+1} - a_{2n+1}a_{2n}A_n = \sqrt{1-D}(B_{n+1}a_{2n+2} - B_na_{2n+1}) + Ja_1\delta_{n0}. \quad (2.9)$$

Since a two-term recurrence is of the first order, it only has one solution. This implies that we do not have to consider minimal and dominant solutions. However, it can still happen that the solution is unstable. This can be tested by the following theorem:

Root Condition Theorem [58]

Consider the recurrence $y_{n+k} + a_1y_{n+k-1} + \dots + a_ky_n = 0$. The corresponding characteristic polynomial is $\phi(u) = u^k + a_1u^{k-1} + \dots + a_k$. Necessary and sufficient for boundedness (stability) of all solutions of the recurrence relation for all positive n is the following root condition:

- (i) All roots of the characteristic equation are located inside or on the unit circle $|z| \leq 1$.
- (ii) The roots on the unit circle are simple.

The homogeneous recurrence relation corresponding to (2.9) is $A_{n+1} - a_{2n+1}a_{2n}A_n = 0$, which has characteristic polynomial $\phi(u) = u - a_{2n+1}a_{2n}$. Setting $\phi(u) = 0$, we find that the characteristic polynomial has the root $u = a_{2n+1}a_{2n}$. Since $|a_n| \leq 1$, for all n , we have that also $|a_{2n+1}a_{2n}| = |a_{2n+1}||a_{2n}| \leq 1$ and therefore, by the root condition, the recurrence relation is stable. Hence, we can simply use a forward recurrence to solve for the coefficients A_n .

3.3 Comparison of algorithms for recurrence relations

3.3.1 Matlab backslash operator

Another way of solving recurrence relations is by putting it in matrix-vector notation. However, for the top left and bottom right cell, we have to impose boundary conditions. We assume $B_{-N-1} = 0$ and $B_{N+1} = 0$. Since we are aiming to find the minimal solution, this is a very reasonable assumption. From a physical point of view, it can be interpreted as the reflection probability going to zero after $N+1$ reflections, which sounds probable as well. Note that in the backward recurrence algorithm, it is not necessary to make any assumptions. In matrix-vector notation, the recurrence relation can be written as

$$\begin{bmatrix} \gamma_{-N} & 1 & & & & & \\ \chi_{-N+1} & \gamma_{-N+1} & 1 & & & & \\ & \ddots & \ddots & & & & \\ & & \chi_{-1} & \gamma_{-1} & 1 & & \\ & & & \chi_0 & \gamma_0 & 1 & \\ & & & & \chi_1 & \gamma_1 & 1 \\ & & & & & \ddots & \ddots \\ & & & & & \chi_{N+1} & \gamma_{N+1} & 1 \\ & & & & & & \chi_N & \gamma_N \end{bmatrix} \begin{bmatrix} B_{-N} \\ B_{-N+1} \\ \vdots \\ B_{-1} \\ B_0 \\ B_1 \\ \vdots \\ B_{N-1} \\ B_N \end{bmatrix} = \begin{bmatrix} 0 \\ 0 \\ \vdots \\ 0 \\ \zeta_0 \\ 0 \\ \vdots \\ 0 \\ 0 \end{bmatrix}, \quad (3.40)$$

where ζ_0 is the source term, given by

$$\zeta_n = \frac{\sqrt{1-D}}{D} \delta_{n0} \cdot \frac{1-a_{2n+1}^2}{a_{2n+2}a_{2n+1}} = \begin{cases} \frac{\sqrt{1-D}}{D} \cdot \frac{1-a_1^2}{a_2a_1} & \text{if } n=0, \\ 0 & \text{if } n \neq 0. \end{cases} \quad (3.41)$$

After solving for the coefficients B_n , we can consider them as known. We can do the same for the recurrence relation for A_n , which is given by $A_{n+1} - a_{2n+1}a_{2n}A_n = \sqrt{R}(B_{n+1}a_{2n+2} - B_na_{2n+1}) + Ja_1\delta_{n0}$. Writing this in matrix vector notation, we obtain

$$\begin{bmatrix} -a_{-2N+1}a_{-2N} & 1 & & & & & \\ & \ddots & & & & & \\ & & -a_1a_0 & 1 & & & \\ & & & \ddots & & & \\ & & & & -a_{2N-1}a_{2N-2} & 1 & \\ & & & & & -a_{2N+1}a_{2N} \end{bmatrix} \begin{bmatrix} A_{-N} \\ A_{-N+1} \\ \vdots \\ A_0 \\ \vdots \\ A_{N-1} \\ A_N \end{bmatrix} = \begin{bmatrix} B_{-N} \\ B_{-N+1} \\ \vdots \\ B_0 \\ \vdots \\ B_{N-1} \\ B_N \end{bmatrix} + \begin{bmatrix} 0 \\ 0 \\ \vdots \\ -\sqrt{R}J \\ \vdots \\ 0 \\ 0 \end{bmatrix}.$$

Suppose we want to solve $Ax = B$ for x , where A is an $n \times n$ matrix and B is $n \times m$ (usually, $m = 1$). In order to find x , we simply have to do $x = A^{-1}B$. Since this is an implicit way of solving ($Ax = B$ is solved as a system of equations, all at the same time), we do not expect any stability issues. Computation of $x = A^{-1}B$ is done using Matlab's built-in backslash operator, i.e. $A \setminus B$. This is a highly optimized code of order n (while computing the inverse explicitly is of order n^2 , and this is not necessarily numerically stable either).

To make the algorithm even more efficient, we utilize the sparsity of the matrix. The matrices we use have only a few non-zero elements, located at the three diagonals. Therefore, it is useful to store them as sparse matrices with the Matlab command `sparse`. This implies that only the non-zero

elements and their row indices are stored (the large amount of zeros is not stored). Therefore, using a sparse matrix instead of a regular matrix reduces the amount of required memory and makes the computation much faster.

3.3.2 Comparison

We have introduced two algorithms to solve the three term recurrence (2.8) and obtain the coefficients B_n . We did this using both the backward recurrence algorithm (Section 3.1.3) and using the Matlab backslash operator (Section 3.3.1). In the backward recurrence algorithm, we set the number of iterations to $\nu = N + 20$. When testing the algorithm using the Bessel functions, we noticed that increasing the value of ν does not change the values significantly (see Table 3.1). The same is the case when calculating B_n . The algorithm converges quite fast, usually only one iteration is required. As a result, the value of ν does not really influence the system. Also, the tolerance ϵ did not seem to change anything, both in the results and the computation time. Tolerances 10^{-2} and 10^{-12} require almost the same computation time (the difference for $N = 10000$ is less than a second). The computation time of backward recurrence algorithm is $\mathcal{O}(N^2)$, while the backslash operator only takes $\mathcal{O}(n)$. This is shown in the table and figure below.

N	Backward recurrence	Backslash operator
50	0.021 s	0.0045 s
100	0.027 s	0.0045 s
500	0.13 s	0.0052 s
1000	0.40 s	0.0060 s
5000	7.31 s	0.012 s
10000	30.39 s	0.018 s

Table 3.2: Computation time of B_n coefficients

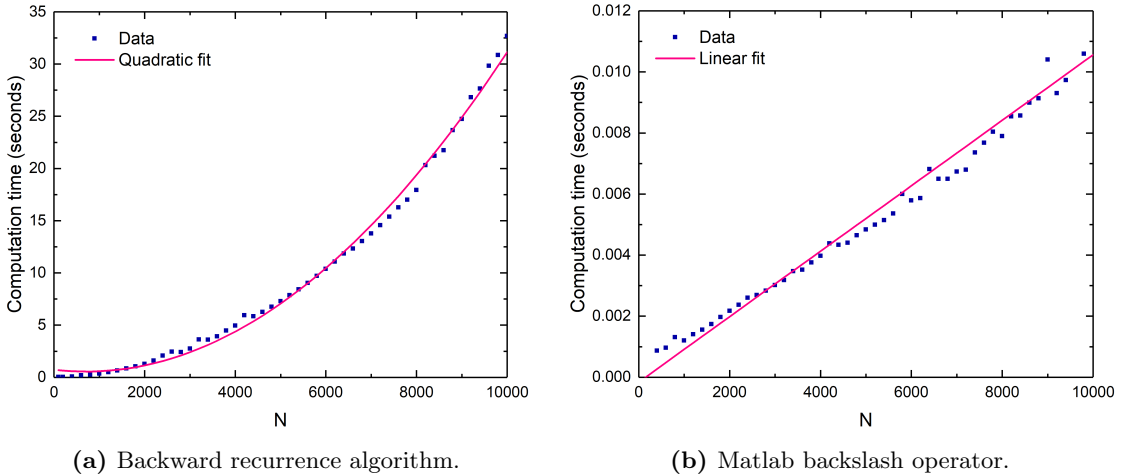


Figure 3.2: Computation time of B_n coefficients as a function of the number of Andreev reflections N . Parameters were fixed to some intermediate values: $D = 0.4$, $\theta_S = 0.8$, $eV = 0.5$ and $\varepsilon = 0.1$.

The downside of using the backslash operator is that we had to assume that $B_{-N-1} = B_{N+1} = 0$. Although this is what we would expect from the physics, these boundary conditions that were not dictated by the problem. The backward recurrence algorithm uses a normalising sum and does

therefore not require any of the values to be known in advance.

Even more remarkable was that the values of B_n obtained using the backward recurrence did not depend on the normalisation conditions at all (contrary to what we saw with the Bessel functions in Section 3.1.3). The reason for this is that the full homogeneous solution is practically zero. Only the particular solution had a value significantly larger than zero, which is independent of the normalisation. The particular solution does depend on ζ and γ (see Section 3.1.4), which are parameters related to the physics of the problem.

An example for a certain set of parameters is shown in Fig. 3.3. The particular solution is the source term, which consists of a Kronecker δ -function at $N + 1$. Therefore, the coefficient B_n is expected to only have a non-zero value at $N + 1$. For the backward recurrence algorithm, this is indeed the case. For the backslash operator, the value of B_n can become negative and/or imaginary. For some parameters, the imaginary part can even be much larger than the real part. Considering the physical interpretation, a negative and/or imaginary value of B_n is not necessarily wrong, since B_n represents a complex probability amplitude (the actual probability is found by taking the absolute valued squared). Although a negative and/or imaginary is not expected here, since the source is real and positive.

On top of that, the B_n obtained by the backslash operator has three non-zero values instead of one. This is most likely because the matrix that was used has three diagonals (see Eq. (3.40)), all of which contributed to B_n . This is wrong, because it implies that the source is not a true Kronecker δ -function.

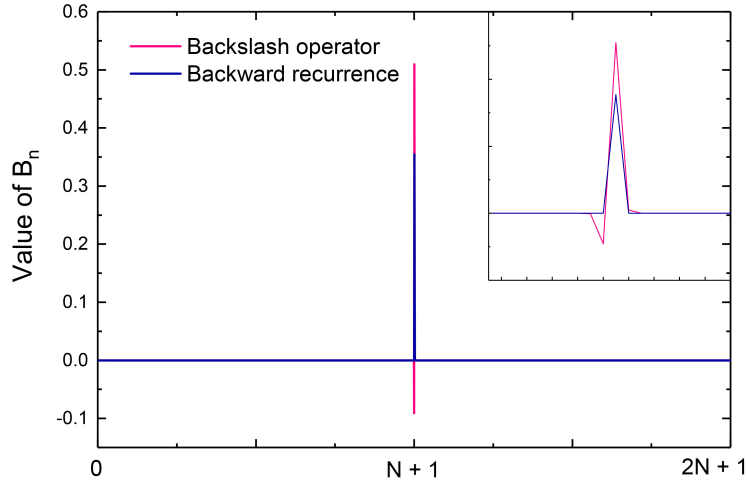


Figure 3.3: The value of coefficient B_n , obtained using the backslash operator and the backward recurrence algorithm. The peak at $N + 1$ corresponds to the source term. Its value is $0.5095 + 0.0766i$ using the backslash operator and 0.3543 using the backward recurrence. The inset shows a zoomed-in view of the peak. Parameters related to the physics were chosen as $\theta = \pi/4$, $\mu_{TI}/\mu_S = 0.5$, $eV = 2$, $\Delta = 1$ and $\varepsilon = 0$. Parameters related to the backward recurrence algorithm are $N = 1000$, $\nu = N + 100$, $\epsilon = 10^{-16}$, $s = 1$, $\lambda_0 = 1$, $\lambda_m = 0$, for $m > 0$.

To conclude: Matlab is specifically designed to work with matrices and therefore, the backslash operator algorithm turns out to be much faster than the backward recurrence algorithm. However, the backslash operator requires some known values, while the backward recurrence algorithm does not. Also, when using the backward recurrence algorithm, we can be absolutely sure that the solution is the solution we are looking for. The backslash operator might still give a diverging solution for certain (unknown) parameter sets. For testing and playing around, the backslash operator is preferred because of its computation speed. However, when we want to be certain that we are considering the true value of B_n , the backward recurrence algorithm is recommended.

3.4 Numerical integration

3.4.1 Adaptive Simpson's method

To do the numerical integration, the Matlab function `integral` was used. This function was chosen because of its simplicity, its easy adaptivity to a required tolerance and its effective way of taking care of singularities (Section 3.4.2). Suppose we want to calculate

$$\int_a^b f(x) dx.$$

The syntax that Matlab uses for this is

`integral(f,a,b,'RelTol',1e-6),`

where `RelTol` is an abbreviation for “relative tolerance”. In this example, it is set to $1 \cdot 10^{-6}$ (which is its default value). The `integral` algorithm follows the so-called adaptive Simpson's method. The algorithm divides the interval $[a, b]$ into subintervals and works on them recursively. It calculates the value of the integral using both the regular 3-point Simpson's rule and the 5-point composite Simpson's rule (illustrated in Fig 3.4). If the values agree within the given tolerance, the algorithm extrapolates between the two values and uses this as the value of the subinterval. If it does not agree with the tolerance, the subinterval is split in half and the procedure is repeated on these newly defined, smaller subintervals. [59]

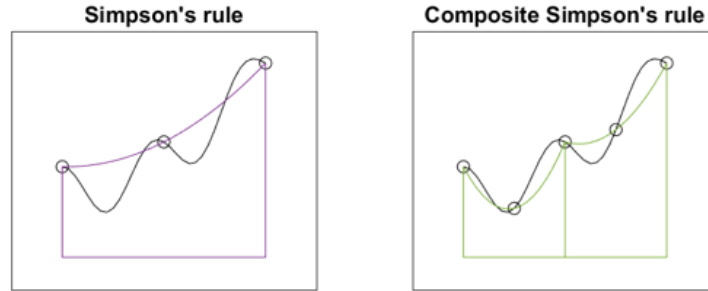


Figure 3.4: The regular 3-point Simpson's rule (left) and the 5-point composite Simpson's rule (right). Image from [59].

The `integral` function is used to calculate the DC current through the junctions, which is given by (see Section 2.2.3 for details)

$$I_0 = \frac{e}{\pi \hbar} \left[eVD - \int J(\varepsilon) \left\{ a_0^* A_0^* + a_0 A_0 + \sum_n (1 + |a_{2n}|^2) (|A_n|^2 - |B_n|^2) \right\} d\varepsilon \right], \quad (2.11)$$

where A_n and B_n were obtained from the recurrence relations, $J(\varepsilon) = \sqrt{1 - a_0^2}$ and $a_n = a(\varepsilon + neV)$ with

$$a(\varepsilon) = \frac{1}{\Delta} \begin{cases} \varepsilon - \operatorname{sgn}(\varepsilon) \sqrt{\varepsilon^2 - \Delta^2} & |\varepsilon| > \Delta, \\ \varepsilon - i \sqrt{\Delta^2 - \varepsilon^2} & |\varepsilon| < \Delta. \end{cases} \quad (1.20)$$

For testing purposes, the relative tolerance was set to 10^{-2} , which gives results very fast. The actual graphs were calculated with a tolerance of 10^{-8} in order to get nice smooth graphs.

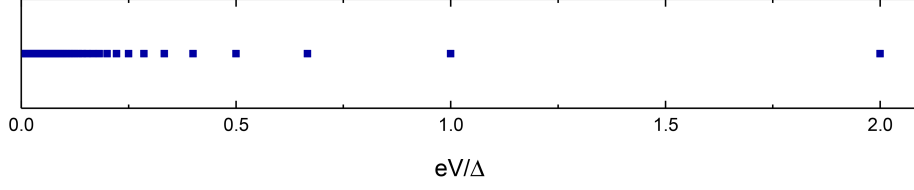


Figure 3.5: Waypoints $eV = 2\Delta/q$, $q \in \mathbb{N}$.

3.4.2 Avoiding singularities

As already explained in Sections 2.2.3, 2.3 and 2.4.3, the recurrence relations exhibit singularities in the applied voltage. Considering the positive side of the eV spectrum, these singularities are located at

$$\begin{aligned}
 \text{S/N/S junction in 1D} & \quad eV = \frac{2\Delta}{q}, \\
 \text{S/TI/S junction in 1D} & \quad eV = \frac{\Delta}{q}, \\
 \text{S/TI/S junction in 2D} & \quad eV = \frac{\Delta(1 + \sin \theta_S)}{q}, \quad q = 2n + 1, \quad n \in \mathbb{N}.
 \end{aligned}$$

The Matlab function `integral` already splits the interval $[a, b]$ into subintervals. The points where the interval $[a, b]$ is split are called “waypoints”. By defining the singularities as waypoints, we integrate in between them and avoid integrating over them. This sounds very straightforward, but there is a little more to it.

First of all, it is not always necessary to use waypoints. More often than not, `integral` manages just fine (especially with a small tolerance). Therefore, an if-statement was used that checks if the value of `integral` is NaN (abbreviation for “not a number”). This is a numeric data type value that corresponds to an undefined or unrepresentable value (for example $0/0$). Checking if something is NaN in Matlab can be done easily using the command `isnan`. Only if this is the case, we define waypoints.

Secondly, note that the singularities specified at the beginning of this section are singularities in the applied voltage eV , while the integration is over the energy ε . Singularities only occur for odd q . Therefore, we have to distinguish between even and odd N (by using an if-statement). In the denominators of the coefficients in the recurrence relation, both a_{2n+1} and a_{2n-1} occur. To take this into account, we make two vectors “waypoints1” and “waypoints2” to store both. However, some of them may overlap. Using the Matlab command `unique`, we can filter them. Finally, the endpoints of the interval $[-V_m, V_m]$ have to be added to our waypoints vector.

After the waypoints vector is defined, we can do the integration again. The output of the `integral` function is called `integralOut`. We set the value of `integralOut` back to zero and use the `integral` function to integrate from one waypoint to the next. A simplified version of the code to calculate is shown on the next page.

```

if isnan(integralOut)
    if round(N/2) == N/2                                (N is even)
        waypoints1 = (-N-1:2:N+1)*eV - Δ
        waypoints2 = (-N-1:2:N+1)*eV + Δ
    else                                                  (N is odd)
        waypoints1 = (-N-2:2:N+2)*eV - Δ
        waypoints2 = (-N-2:2:N+2)*eV + Δ
    end
    waypoints = unique([-Vm,waypoints1,waypoints2,Vm])
    integralOut = 0;
    for i = 1:length(waypoints)-1
        integralOut = integralOut +
            integral(func,waypoint(i),waypoints(i+1),'RelTol',1e-8)
    end
end
end

```

In Matlab, it is also possible to give the function `integral` the additional option to work with waypoints, which is even easier. The Matlab syntax is

```
integral(f,a,b,'RelTol',1e-6,'Waypoints',vector),
```

where `vector` should be replaced by a vector that contains real or complex numbers, separated by commas. However, according to the Matlab documentation, this is mainly used to integrate efficiently across discontinuities of the integrand. The documentation warns that it is not advisable to use the `Waypoints` option for avoiding singularities and recommends splitting the interval instead, as was done here.

3.5 Angle averaging

In the two dimensional case, the current as a function of the incoming angle θ and of the applied voltage eV , i.e. $I = I(eV, \theta)$. The goal is to calculate the current for every value of θ and take the average over all θ . We can reduce the two dimensional case to the one dimensional case by setting $\theta = 0$ (which corresponds to perpendicular incidence).

The first step is to define a list of angles ranging from $-\pi/2$ to $\pi/2$. This is done using the Matlab command `linspace(-pi/2,pi/2,p)`, where p is the number of steps in θ . Let q be the number of steps in the applied voltage eV . Whereas the current was stored as a vector of length q in the one dimensional cases, we store it as a $q \times p$ matrix in the two dimensional case. For robust computation, it is advisable to predefine a “current matrix”, which is an empty $q \times p$ matrix.

For fast computation, a parallel for loop (Matlab command `parfor`) is used to calculate the current $I(eV, \theta)$ for every value of θ . Every iteration generates a current vector $I(eV, \theta_{index})$ for a fixed value of θ . These current vectors are stored as the columns of the current matrix and multiplied by $\cos \theta$. After the parallel for loop has filled the current matrix, we can obtain the average current $I(eV)$ by taking the sum over all columns and divide by p . This is done using the Matlab command `sum(currentmatrix,2)/p`. In pseudo-code, this process can be written as

```

Parfor  $\theta_{index} = 1, \dots, p$ 
  For  $eV_{index} = 1, \dots, q$ 
    Calculate matrix element  $I(eV_{index}, \theta_{index})$ .
  end
  Store current vector  $I(eV, \theta_{index}) \cos \theta$  as column  $\theta_{index}$  of current matrix.
end

$$I(eV) = \frac{1}{p} \sum_{\theta_{index}=1}^p I(eV, \theta_{index}).$$


```

Experimental observation of the zero bias conductance peak

This section is dedicated to the experimental work. We start with a brief literature review on what has already been done in Section 4.1. A couple of possible designs were discussed, as explained in Section 4.2. The fabrication of the structures that we chose is shown step by step in Section 4.3. At the end of this section, an overview of all samples is given, including an explanation on what we changed compared to the previous sample. The sections that follow show the results of the measurements. Some intuitive discussions, as well as a small calculation in order to explain the experimental data, are also included.

4.1 Brief review of previous work

Over the past couple of years, there have been two main trends in the experimental detection of a Majorana particle: 4π periodic current-phase relations in topological Josephson junctions (i.e. junctions of two superconductors with a topological material in between them) and the observation of a zero bias conductance peak (ZBCP) in nanowires. We will briefly discuss both of them.

4.1.1 Zero bias conductance peak in nanowires

In Section 1.4, we have seen that a Majorana particle can be considered as half electron and half hole. Since an electron has energy E and a hole has energy $-E$, the only way this is possible is for the Majorana particle to be located at zero energy, which would result in a ZBCP. To observe the ZBCP, one can measure a current (I)-voltage (V) current spectrum. From this, the differential conductance (dI/dV) can be extracted as a function of the applied voltage. In the tunnel limit, the differential conductance is proportional to the density of states (see Appendix E). This implies that the zero energy peak in the density of states translates to a ZBCP (that is, a peak at zero applied voltage) in the conductance spectrum. This type of measurement has been done in Delft, using indium antimonide (InAs) nanowires. [60]

InAs is a semiconductor with strong spin-orbit coupling. A semiconductor has a standard parabolic dispersion. The spin-orbit coupling splits the parabola into two parabolas; one for spin up, the other for spin down. This is drawn in Fig. 4.1b. An in-plane magnetic field can open up

a gap. We can then tune the Fermi level such that it is inside the gap and only two states are available, as shown in Fig. 4.1c. Since these two states originate from bands with opposite spin, there will be no scattering from one to the other.

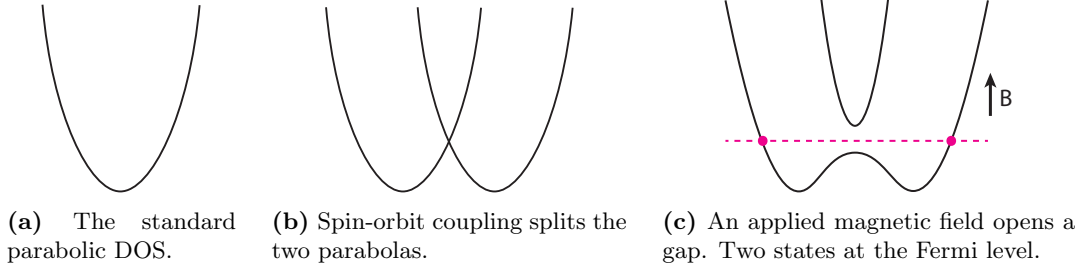


Figure 4.1: Construction of the density of states of InAs.

The nanowire is coupled to an *s*-wave superconductor, such that the combination of only two states inside the gap and the proximity induced superconductivity result in a topological superconductor (see Section 1.4.3). Their results are depicted in Fig. 4.2. We can see the superconducting conductance spectrum, characterised by the coherence peaks at $\sim \pm 250 \mu\text{V}$. At a certain applied magnetic field, the gap opening allows for a ZBCP. When the applied field becomes too high, it destroys the superconductivity (see section 1.2.1) and the conductance spectrum becomes almost flat (indicating the superconductor is in its normal state).

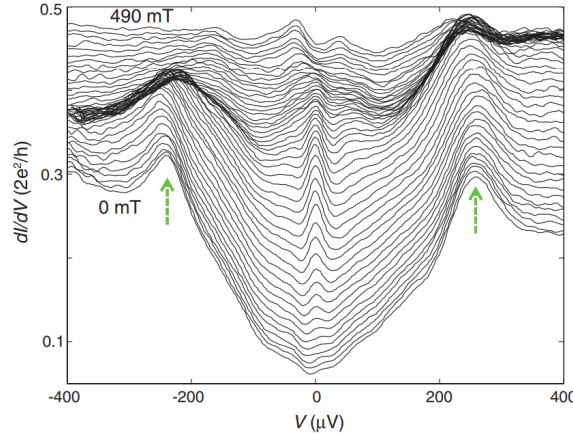


Figure 4.2: Differential conductance measured through a nanowire coupled to an *s*-wave superconductor. The graphs from bottom to top correspond to increasing magnetic field. Green arrows point at the coherence peaks of the superconducting gap. The peak in the middle is the ZBCP. From [60].

It should be noted here that opening a gap before destroying the superconductivity is not trivial. Besides having strong spin-orbit coupling, InAs has another property that makes this possible. InAs is known to have a relatively large *g*-factor, which is the factor with which the gap in Fig. 4.1c opens as a function of magnetic field. This implies that for a small magnetic field, a sizeable gap can be opened without suppressing the superconductivity. [60]

4.1.2 4π periodicity in topological Josephson junctions

In Chapter 2, we calculated the DC current through a topological Josephson junction. We did not take any phase difference between the two superconductors into account. The phase difference is

called ϕ and was already briefly discussed at the beginning of Chapter 2. This phase difference turns out to be the crucial parameter here.

In a conventional Josephson junction (without any topological effects), the energy spectrum of the ABS is given by [61]

$$E_{\pm} = \pm \Delta \sqrt{1 - D \sin^2(\phi/2)}, \quad (4.1)$$

where D is the interface transparency. This relation is shown in Fig. 4.3. As explained in section 1.4.3, usually the transparency is not perfect, such that $D < 1$. In this case, a gap opens in the energy-phase relation. If we have perfect transmission, i.e. $D = 1$, it is possible to have a MBS. Note that the energy-relation becomes 4π periodic in this case (instead of 2π which was the case for the regular ABS). This was first claimed by Kitaev. [34]

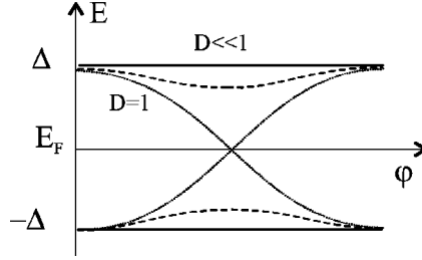


Figure 4.3: Energy-phase relation. From [61].

Recall the supercurrent that we introduced in the beginning of section 2. We simply assumed the expression that we gave in Eq. (2.1), but where it comes from is [61]

$$I_S = \frac{2e}{\hbar} \frac{dE(\phi)}{d\phi}. \quad (4.2)$$

Hence, it follows that the current-phase relation for Majorana particles is 4π periodic as well. This can be interpreted as follows: in the conventional 2π periodic case, Cooper pairs (charge $2e$) tunnel. Majorana particles enable single electron (charge e) tunnelling, which doubles the periodicity. The experimental realisation of the 4π periodic current-phase relation is discussed comprehensively in Refs. [62, 38]. We will briefly summarize the procedure here. When a radio frequency (RF) current is applied to a Josephson junction, the supercurrent synchronises with this frequency, which gives rise to steps in the I-V curve. [63] In a conventional Josephson junction, these steps are located at voltages $V_n = n\hbar f/2e$, where $n \in \mathbb{Z}$ and f is the frequency. In a topological junction, only the even steps are visible as a result of the 4π periodic current-phase relation. In practice, there are both 2π periodic and a 4π periodic signals present in a topological Josephson junction. The 2π periodic signal results from extra Andreev modes and quasiparticle poisoning. [64] This signal dominates in the case of high frequency and high voltage, [62] such that only the $n = 1$ step is missing (and therefore, the first visible step has a doubled step height). The missing first step has been observed in Josephson junctions with HgTe [62] and with $\text{Bi}_{0.97}\text{Sb}_{0.03}$ [38] as the middle layer.

4.1.3 Goal of this project

The ZBCP in nanowires and the 4π periodic state in topological Josephson junctions might be the results of the same Majorana physics. Up until now, these two fields were disconnected and there was no way to compare them. The purpose of our experiments is to check whether these phenomena could indeed be a result of the same physics. We aim to measure a ZBCP with the use of a topological insulator.

In a nanowire, a magnetic field was needed to make sure that there are only two states available at the Fermi level. A topological insulator, on the other hand, has only two states available at the Fermi level due to its spin-momentum locking. Therefore, the experiments with a topological insulator are, in principle, even easier than those with the nanowires, since the magnetic field is not needed.

4.2 Sample design

The goal of the experimental part of this project was to detect a ZBCP in a junction consisting of a topological insulator and a superconductor. The materials that we were aiming to use were the topological insulator bismuth antimony tellurium selenium (BiSbTeSe_2 , or “BSTS” for short) and the superconductor niobium (Nb). To make a tunnel barrier, we used the insulator aluminium oxide (Al_2O_3). For the normal metal contacts we used gold (Au). We came up with five possible setups, as shown in Fig. 4.4.

The first setup (Fig. 4.4a), has a double tunnel junction which is completely symmetric. With this setup, we probe the Majorana bound states at both sides of the BSTS/Nb interface, such that the resulting signal is the sum of both Majorana bound states. However, the BSTS flake is never completely symmetric, and therefore, neither is the tunnel signal. Suppose we were to observe a ZBCP. The peak height is quite important (more on this in Section 4.4.1), but it is impossible to determine how much of the peak height originates from each tunnel junction. Therefore, this is not an absolute way to measure the signal and we discard this setup.

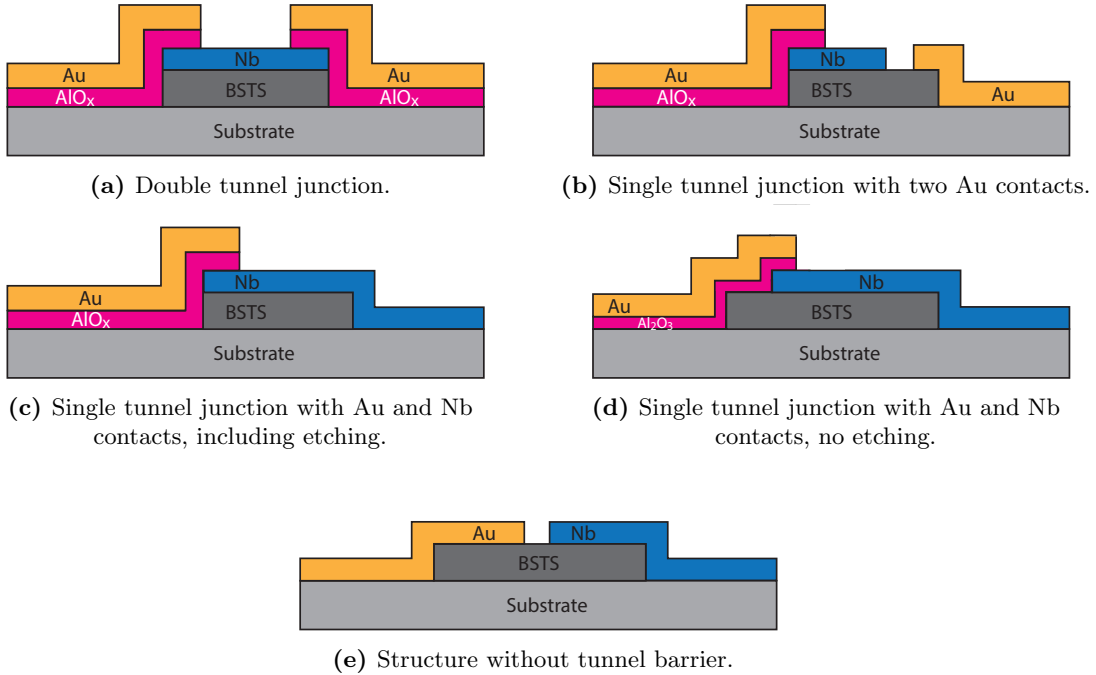


Figure 4.4: All possible structures that we considered.

The second setup (Fig. 4.4b) has a single tunnel junction and two Au contacts. The problem with this setup is that BSTS has a sheet resistance of $\sim \text{k}\Omega/\square$. If the tunnel junction is “far away” from the Au contact (such that they are isolated from each other), the Au contact will give a high resistance due to this high sheet resistance. This completely dominates the signal and it is not possible to observe a ZBCP. When putting the Au closer to the tunnel junction, the current might go into the Au directly, which does not give the desired signal either.

The third and fourth setup (Fig. 4.4c, d) have a single tunnel junction as well. The Nb that we used to create the BSTS/Nb interface is extended into a contact. This solves the problem of the high sheet resistance. Additionally, this setup requires one less electron beam lithography step, which makes the fabrication process slightly easier. The difference between them is that in Fig. 4.4c, we etch through the BSTS before depositing the Al_2O_3 and the Au layers. This is supposed to create a better side contact. In Fig. 4.4d, there is no additional etching involved.

Finally, we also consider a setup without tunnel barrier (Fig. 4.4e). In this case, the resistance is determined by the distance between the contacts. Note that there is no explicit tunnel barrier, but there will most likely still be a small interface barrier due to an imperfect interface (resulting from, e.g., lattice mismatch, dirt, oxidation).

4.3 Sample fabrication

This section gives a detailed explanation of all steps of the sample fabrication, including all relevant parameters. We start by discussing the structure including tunnel barrier of Fig. 4.4c and d.

4.3.1 Structure including tunnel barrier

All steps explained below are accompanied by schematic images shown in Fig. 4.5.

Step 1: BSTS flakes

We start with a silicon (Si) substrate with a thin, insulating silicon oxide (SiO_x). We would like to use BSTS as our topological insulator. Since it is not possible to grow a layer of this material, we use a BSTS crystal, stick tape to it and use that to exfoliate BSTS flakes. By subsequently sticking the tape on top of the substrate, the flakes are transferred to the substrate. In general, this method produces a large amount of flakes, which is inconvenient to work with. We then put the substrate in acetone, in the sonicator for a fraction of a second. This removes the flakes that do not stick to the substrate very well, such that we lose them before fabrication rather than after. This leaves us with a good amount of BSTS flakes on top of the substrate.

The substrate is $7 \text{ mm} \times 7 \text{ mm}$ in size. On top of it is a grid with gridpoints, which makes it easier to find the flakes we are looking for. We put the substrate underneath a microscope that is connected to a camera. We search for flakes that have dimensions of a few micrometers in length and width, that look flat (i.e. no relief on them) and thin (this can be tested by bringing the camera slightly out of focus). We take pictures of them with the camera and make sure to note their coordinates on the grid. On the computer, we trace the images of the flakes and, using designated software, we draw a design on them for the Nb and the Au contacts. This design is used in steps 3 and 7. Some examples of pictures of flakes and their corresponding designs are shown in Fig. 4.6 at the end of this section.

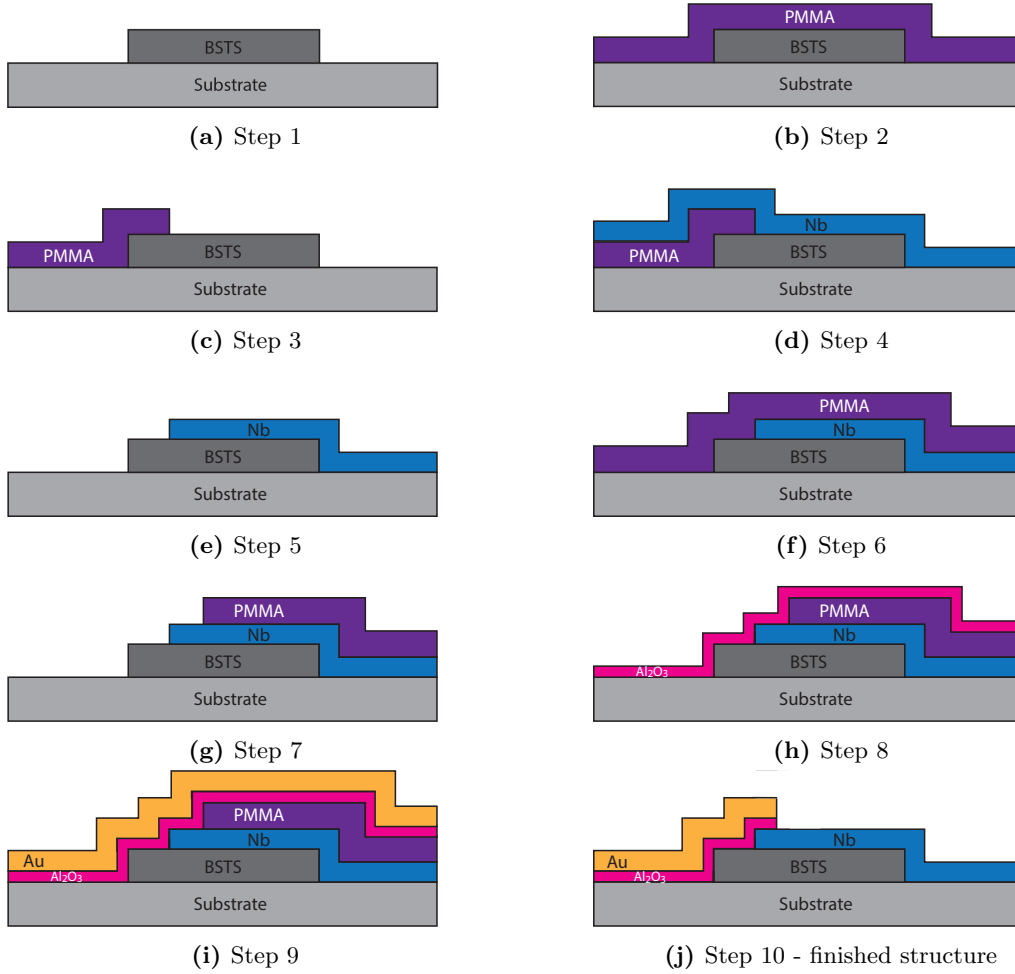


Figure 4.5: Schematic pictures of the steps that are necessary to construct the structure shown in (j).

Step 2: spinning PMMA

We put a layer of polymethyl methacrylate (or “PMMA” for short) on our structure. This is done by putting a 40 μL droplet of PMMA on top of the substrate and spinning the sample in a photoresist spincoater with 3000 rpm for 45 seconds. This gives a layer of approximately 255 nm of PMMA. The sample is transferred to a hot plate where we bake it for 5 minutes at 160°C.

Step 3: e-beam lithography

We use electron beam lithography (e-beam) to expose very small parts of the PMMA, according to a predefined design. The small structures are exposed with a dose of 200 $\mu\text{C}/\text{cm}^2$, while the large structures require 300 $\mu\text{C}/\text{cm}^2$. After exposure, the sample is put in methyl isobutyl ketone (MIBK) for 40 seconds. This develops the PMMA, which means that the exposed parts are removed. Immediately afterwards, the sample is put in isopropyl alcohol (IPA) for 30 seconds. This stops the development and prevents the structure from overdeveloping. We now have a mask, made of PMMA, that protects the parts of the BSTS where we do not want to deposit any material.

Step 4: sputter deposition of Nb

We want to deposit a layer of the superconductor Nb on top of the sample. We start by RF substrate cleaning, which is done for 30 seconds at a voltage of 60 V and Ar pressure of $1.33 \cdot 10^{-2}$ mbar. Using DC sputtering, we deposit 80 nm of Nb at a power of 250 W and a pressure of $7.3 \cdot 10^{-3}$ mbar. When it gets into contact with air, Nb will oxidise. In order to prevent this, we deposit a 2 nm palladium (Pd) capping layer (not shown in the pictures). This is done by RF sputtering at a power of 300 W and Ar pressure of $1.33 \cdot 10^{-2}$ mbar.

Step 5: lift-off

The sample is rinsed with acetone. This dissolves the PMMA and removes the Nb that was on top of it. Since the acetone stains when drying, we subsequently rinse it with ethanol and blow it off with a nitrogen gun. This leaves us with Nb only partly covering the BSTS flake.

Step 6: spinning PMMA

Another layer of PMMA is spun on the sample. This is done exactly the same as in step 2.

Step 7: e-beam lithography

Using the e-beam, we expose the bare part of the substrate and make sure to slightly overlap the flake and the Nb. The e-beam lithography and the development is done the same way as in step 3.

Step 7b: etching (optional)

In the structure Fig. 4.4c, etching is included in the process. The fabrication of Fig. 4.4d skips this step. The schematic pictures in Fig. 4.5 do not show the etching. Etching is done using an argon etcher with the following settings:

beam voltage	500 V
beam current	100 mA
accelerator voltage	100 V
accelerator current	5 mA
discharge voltage	50 V
etch angle	45°
sample rotation	4 rpm

We chose these settings because the etch rates of BSTS and SiO_x were already calibrated at these settings. We calibrated the etch rates of PMMA and Nb ourselves. An explanation of the calibration is given in appendix D.

The goal is to etch completely through the Nb, while still keeping enough PMMA in order to be able to remove it. When the PMMA is damaged too much (by the etching), the chemical structure changes, making it stick firmly to the sample and making the sample useless. After a couple of test runs, we decided to grow 80 nm of Nb, such that we have to etch for 6 minutes. For the other materials, we obtain

	etch rate	after 6 minutes
Nb	14 nm/min	84 nm
BSTS	80 nm/min	480 nm
PMMA	30 nm/min	180 nm
SiO_x	22.8 nm/min	137 nm

From this, we can also see that we have to take care of the SiO_x layer thickness. We have to select a substrate with at least 137 nm SiO_x (preferably thicker), in order to prevent shorting the circuit.

Step 8: insulating barrier

Using atomic layer deposition (ALD), a layer of approximately 1.2 nm of Al_2O_3 is deposited on the substrate. This is done at a temperature of 100°C, which is unusual for ALD. Normally, ALD is

done at 300°C, but this would destroy the BSTS. The materials that BSTS consists of are volatile, e.g. tellurium evaporates at 180°C.

Step 9: sputter deposition of Au

We want to deposit a layer of the normal metal Au on top of the sample by means of RF sputter deposition. Since sputter deposition at a high power damages the delicately thin AlO_x layer, we do the deposition in two steps. We start with a slow deposition. We increase the spacing between the sample and the target to 3 inches and regulate the Ar pressure to be $\sim 8 \cdot 10^{-2}$ mbar. This high pressure is caused by increasing the argon flow as much as possible. The argon ions decelerate the Au atoms. Increasing the spacing makes the distance the Au atoms have to travel longer, which enhances the deceleration. We sputter for 25 minutes, at a voltage of 200 V and a power of 0 W. This results in a 22 nm Au layer. We then switch to the standard deposition. The spacing is 1.6 inch and the pressure is $\sim 2 \cdot 10^{-2}$ mbar. We sputter at these settings for 4 minutes, at 1000 V and 150 W, resulting in a 160 nm Au layer. Hence, the total Au thickness is 182 nm.

Step 10: lift-off

The lift-off is similar to step 5, but Au is harder to remove. Therefore, the sample is put in acetone for a couple of hours. What we are left with is the structure in Fig. 4.5j.

Some pictures of what this looks like underneath a microscope are shown in Fig. 4.6. The flake that was chosen is shown in panel d. The design is shown in panels a-c. During the first e-beam session, the blue parts, which correspond to Nb are exposed (step 3). During a second e-beam session, the orange and pink parts, which represent Au, are written (step 7). In the actual pictures in panels e and f, Nb has a silver colour and Au is, obviously, gold. During one session, the structure is written in two steps, which is why two colours per session are used. First we expose the small writefield, which is 100 μm in size and marked by the crosses. The small writefield is coloured light blue for Nb and orange for Au in the design. This is written very precisely (which takes relatively long). Then the large structures are written using a large writefield of 1000 μm , which is less precise and faster. Large writefield structure are coloured dark blue for Nb and pink for Au. The crosses are used to align the second layer (Au) with respect to the first layer (Nb). The large squares in panels c and f are the contact pads, they are 200 by 200 μm in size and we use them to glue the wires onto. Some residue of the glue is still visible in panel f (the black spots).

4.3.2 Destruction of the tunnel barrier due to static charge

After we successfully fabricated a sample, we put it in the probe station to check its resistance. This is done by simply sending a small current through the structure and measuring the voltage. It is done at room temperature and takes approximately half an hour. When the resistance has the expected order of magnitude, the sample can be bonded and prepared for low temperature measurements.

The first sample that did not have any fabrication issues (e.g. misalignment or trouble with lift-off) was BSTS4. At room temperature, the resistance values were reasonable (see Table 4.1). We decided to prepare three of the structures for low temperature measurements in the Triton dilution fridge. The names of the structures indicate their locations on the grid, i.e. $7 \circ 4$, $4 \circ 2$ and $8 \circ 7$. After cooling down, we quickly checked the resistance again. The first two structures gave no signal at all. The third structure had a very high resistance of 2.8 M Ω . We applied a voltage, measured the current and extracted the differential conductance (dI/dV) from structure $8 \circ 7$ (see Fig. 4.7). The superconducting gap from Nb was visible and of the right order of magnitude, but the resistance was too high to do any useful measurements. A small structure inside the gap that we hope to see would be completely dominated by the high resistance of the structure.

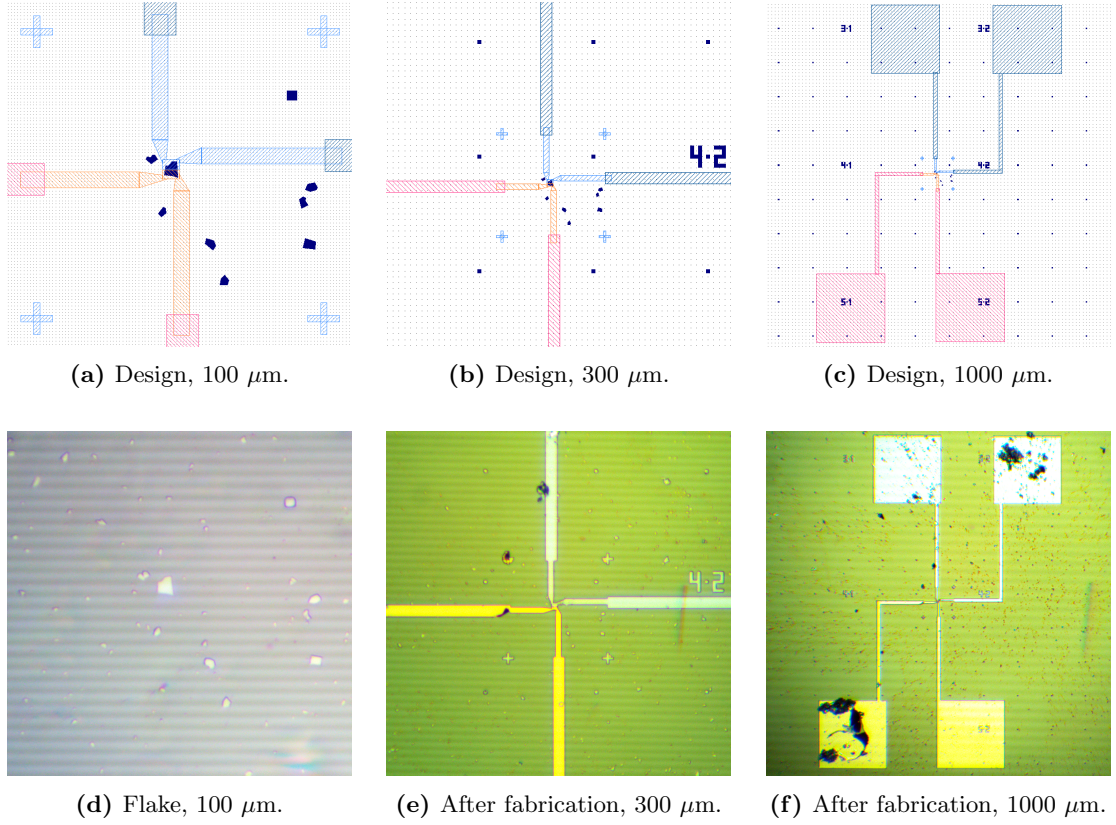


Figure 4.6: E-beam design and optical images of BSTS4 at different scales.

Sample	Before bonding	After bonding
7 ◦ 4	6 kΩ	overload
4 ◦ 2	700 kΩ	overload
8 ◦ 7	430 kΩ	2.8 MΩ

Table 4.1: Values of the resistance of three structures on BSTS4, before and after bonding.

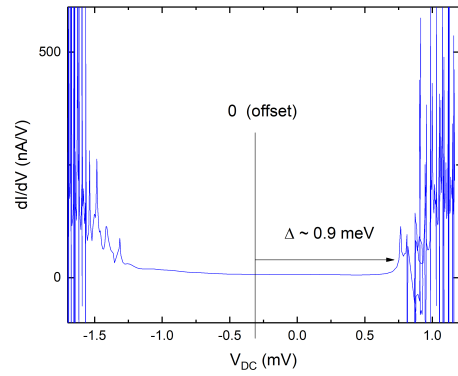
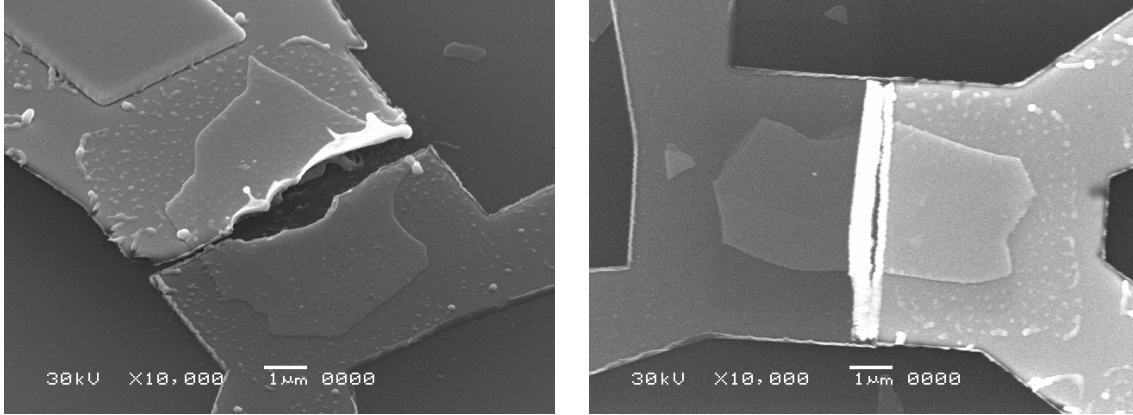


Figure 4.7: Differential resistance of 8 ◦ 7.

We decided to put the sample inside a scanning electron microscope (SEM), which can take pictures of a surface by using a focused beam of electrons. We found that the tunnel barriers of 7 ◦ 4 and 4 ◦ 2 were completely destroyed. The flake underneath had disappeared, such that the Nb and Au contacts were disconnected, which explains why we could not send a signal through the structure. Although this was quite frustrating, it resulted in beautiful pictures, for instance the one in Fig. 4.8a. The other structure, with the high resistance, still had a part of the structure that was

touching, although it was severely damaged as well, as can be seen in Fig. 4.8b.



(a) Completely exploded tunnel barrier of 7×4 .

(b) Partially exploded tunnel barrier of 8×7 .

Figure 4.8: SEM images of the structures on BSTS4 confirmed why we could not measure a proper signal. The dark contacts are Nb (bottom right in (a), left in (b)) and the lighter contacts are Au.

The reason why these tunnel barriers exploded is most likely because they are very thin (1.2 nm) and very sensitive to static electricity. Just after fabrication, we could still measure the resistance. The samples were stored in a box that might have been statically charged. When preparing for the low temperature measurements, we have to glue wires to the Nb and Au contacts (bonding). Most likely, either the air, the wires or the gloves gave some static electricity as well. Wearing a woollen cardigan with rubber gloves does not help either.

To solve the problems related to static electricity, precautionary measures were taken when bonding the next samples. The samples were stored in an AFM tip box, which has a conducting surface. Bonding was done with bare hands, without woollen clothing and while wearing a bracelet that was connect to the ground of a wall outlet (such that the bonder is grounded).

4.3.3 Structure without tunnel barrier

Because we had so much trouble with the tunnel barriers, we decided to make a structure without a tunnel barrier first. There could, however, still be a barrier due to an imperfect interface. Instead of a tunnel barrier, we placed the Nb and Au contacts 200 nm apart from each other, as shown in Fig. 4.4e. The deposition of the Nb layer remains unchanged and therefore, the first six steps are the same as for the previous structure. The e-beam design in step 7 is changed such that there is some space in between the Nb and the Au. Since we do not need the tunnel barrier, we skip step 8. Before, we had to deposit Au carefully in order not to damage the tunnel barrier. But since there is none, the deposition of Au (step 9) is even easier for this structure. First we etch (in the sputter machine) at 150 W for half a minute to clean the sample. We then deposit a thin 6 nm layer of titanium (Ti) at 150 W in one minute. The reason for this is that Ti sticks better to the sample and this results in a better contact. We then deposit 100 nm of Au at 150 W in 2.5 minutes. During all the steps, the pressure is kept constant at $2 \cdot 10^{-2}$ mbar.

4.3.4 Sample overview

In total, ten samples were made during this project. An overview of them and what we changed between them is written in Table 4.2.

Sample	Barrier	Etching	Comments
BSTS1	Yes	Yes	We etched as described in step 7b. This severely damaged the PMMA, which made it impossible to do lift-off.
BSTS2	Yes	Yes	We decided to do the etching during a separate step (i.e. an additional e-beam step). The PMMA layer turned out to be uneven during spinning, which resulted in lift-off issues.
BSTS3	Yes	Yes	The etching was done during a separate step. This resulted in alignment issues between the etched parts and the Au contact.
BSTS4	Yes	No	We decided to leave out the etching step. No fabrication issues. When measuring, the tunnel barriers exploded due to static electricity (see Section 4.3.2).
BSTS5	Yes	No	Bonding was done more carefully than with the previous sample. There were no issues, but no interesting results either. We could measure the gap, but there were no signs of Majorana particles.
BSTS6	Yes	No	Disappeared during a cleanroom accident.
BSTS7	No	No	We decided to try structure without barrier. The distance between the contacts was kept constant at 200 nm. Observed zero bias conductance peak.
BSTS8	No	No	Varied the distance between the contacts from 50 nm to 300 nm. Majorana physics unclear.
BiSb1	No	No	Swapped the BSTS for $\text{Bi}_{0.97}\text{Sb}_{0.03}$ (which is a Dirac semimetal instead of a topological insulator). This structure had a high resistance which gave a very noisy signal.
BiSb2	No	No	Resistance too high to measure anything.

Table 4.2: An overview of the ten samples that were made during this project.

4.4 Zero bias conductance peak

The sample BSTS7 (see Table 4.2) was the first one where we did not include a tunnel barrier. Instead, we placed the Au and Nb contacts 200 nm apart, as shown in Fig. 4.4e. We made eight samples on this specific substrate. Five of them survived the full fabrication process. In only one of them, a ZBCP was observed. The differential conductance for different magnetic fields is shown in Fig. 4.9. Panel a shows the full range from 0 to 0.5 T. Around 0.45 T, we can see a small ZBCP. Panel b gives detailed view of this region. The background of all the other samples that we measured had a very similar shape to this one, except that they did not show a ZBCP.

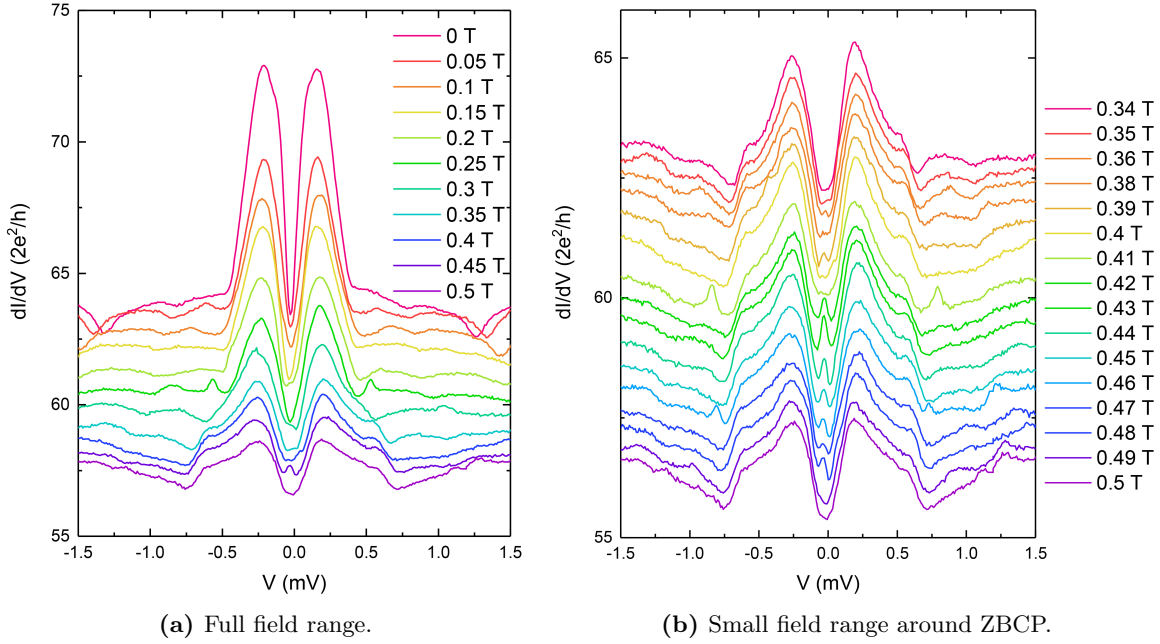


Figure 4.9: Differential conductance in units of conductance quanta.

The top graphs are the true values, the other graphs have an offset to improve the visibility.

The ZBCP reaches its maximum at 0.43 T, where the peak height is $1.4e^2/h$. We will discuss the determination of the height and the meaning of this value in Section 4.4.2. Also for lower field values, there is a very small gap visible sometimes. This will be discussed in Section 4.5.1. Before looking into the details of the ZBCP, we will first consider several candidates that may have caused it.

4.4.1 Origin of the ZBCP

The ZBCP can be caused by several physical phenomena. Obviously, we are hoping to detect a MBS, but there are other contestants that might be able to explain the appearance of a ZBCP. This section starts with an elaboration on a possible MBS in our system. After that, we will discuss a couple of other physical phenomena that can result in a ZBCP and argue whether or not they are probable in our system.

Majorana bound state

In Section 1.4, we already explained why a MBS can result in a ZBCP. In a topological Josephson junction, it is clear where the MBS is located (see Section 1.4.3). In the case with the Au contact, it is not straightforward. The most plausible configuration is shown in Fig. 4.10.

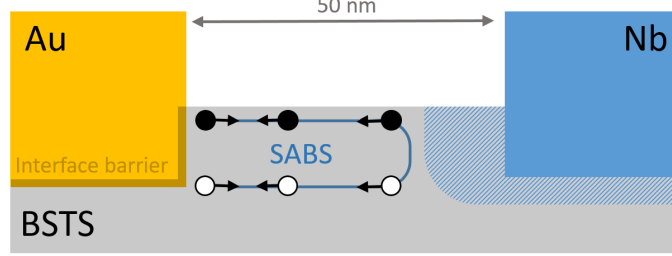


Figure 4.10: Surface Andreev bound state localised between the superconducting BSTS region and the Au. The structure is drawn in real space. The SABS is drawn in momentum space (implying that the electron and hole have different energies, while being at the same location in real space).

The Nb contact causes the BSTS to become locally superconducting by the proximity effect. Therefore, the interface between these two regions is expected to be very transparent. To explain the observation of the ZBCP there should be a way to localise the MBS somewhere in the junction, (this will be elaborated on in the next section) which, then, has to be located at the interface of the Au and the BSTS. This is not an actual tunnel barrier, but most likely a small gap in the dispersion of the Au.

In the design, the distance between the Au and the Nb contact in the original e-beam design was supposed to be 200 nm. Since there are often alignment issues, this distance was checked using an atomic force microscope (AFM). An AFM image of the sample is shown in Fig. 4.11a. From this, we found that the actual distance is only 50 nm. This decreased distance is most likely the result of two effects. Firstly, the aligning issue and, secondly, the AFM image shows a higher region in between the contacts (coloured white in Fig. 4.11a). This is a result of improper lift-off and also decreases the distance. This decreased distance between the contacts turned out to be quite favourable for our measurement. Moreover, it might be the reason why only this sample showed the ZBCP.

The mean free path in BSTS is estimated to be [65]

$$\ell = \frac{\mu m v_F}{e} = \frac{(0.1 \text{ m}^2 \text{V}^{-1} \text{s}^{-1}) \cdot (0.2 \cdot 9.1 \cdot 10^{-31} \text{ kg}) \cdot (3 \cdot 10^5 \text{ ms}^{-1})}{1.6 \cdot 10^{-19} \text{ C}} \approx 35 \text{ nm}. \quad (4.3)$$

The proximity effect in BSTS is very anisotropic. Since BSTS is a topological insulator, it is insulating in the bulk. Along the surface, in the horizontal direction, BSTS behaves metallic and therefore, the induced superconductivity is expected to spread much further. The distance between the contacts is 50 nm. The mean free path is about 35 nm. Therefore, we are in the right order of magnitude to be in the ballistic regime (see Section 1.3.3).

An ABS is expected to be located in between the superconducting BSTS region and the Au. At the Au interface, there will be normal reflection (electrons reflect as electrons and holes reflect as holes), whereas at the interface with the superconducting BSTS, we can also have Andreev reflection. This construction is called a *surface Andreev bound states* (SABS).

The SABS is a MBS if the material that hosts the bound state is in the topological phase, i.e. there is only one spin (see Section 1.3.2) and the transmission is equal to 1 (see Section 1.4.3). If it is in the trivial phase, it is a regular ABS. Further explanation on the topological and trivial phases in nanowires can be found in Ref. [66]. Of course, TIs are always expected to be in the topological phase, but there is a little more to it, which we will elaborate on in Section 4.5.1.

Finally, recall the discussion on topology in the 2D and 3D case from Section 1.4.2. We assume here that the interface barrier of the Au causes a little gap in the dispersion, such that the SABS is localised to 2D.

Regular Andreev bound state

In our system with the topological insulator, we are always in the topological regime and therefore, when the bound state is located at zero energy, we can argue that it is in fact a MBS. In a nanowire, however, there are many different bound states. [66] Therefore, there is a second condition that has to be verified.

Recent theoretical work showed that the regular ABS in a nanowire can also result in a ZBCP which is very similar to the one originating from a MBS. [67] As a response to this, an experimental work compared the two types of bound states. [68] In this experimental work, it was stated that only a stable, quantized ZBCP that is robust against all variations in all gate voltages (back-gate and tunnel barrier) and magnetic field, can be uniquely defined as a MBS. [68]

In a nanowire, we have to be exactly inside the gap (see Fig. 4.1c). The back-gate voltage is used to tune the chemical potential, i.e. move up or down in the Dirac cone. In the topological phase (inside the gap), there are always only two available states, so it should not change. Only when the back-gate voltage becomes negative and large (i.e. below the gap), the wave functions of the two Majorana particles located at each end of the wire start to overlap, effectively making the wire shorter and splitting the peak. The peak height quickly reduces to zero. For voltages that allow the Fermi level to lay inside the gap, the peak height stays at $2e^2/h$. In the trivial phase, on the other hand (above the gap), the peak height depends seemingly linearly on the applied back-gate voltage and does not stay at $2e^2/h$. [68]

Accidental 1D channel

When making an AFM image (Fig. 4.11a), we observed a higher region in between the contacts. At first, it was not clear what this was and we were worried the contacts were touching. If the contacts would be (almost) touching at some point, this could create an accidental 1D channel which could drastically change the transport through the junction. To exclude this possibility, we put the sample in the SEM to get a closer look at the interface, as shown in Fig. 4.11b. We saw that the white part was some Au residue that remained after lift-off, sometimes referred to as “an ear”. It is effectively a thin piece of Au that is standing upright like a wall. This is probably caused by the fact that the e-beam was focused on the substrate, while the BSTS flake is slightly higher. Therefore, the beam might be slightly out of focus here, such that the edges of the PMMA mask are not perfectly sharp. Au is a soft material and most likely stuck to these edges. Ears resulting from the Au lift-off have

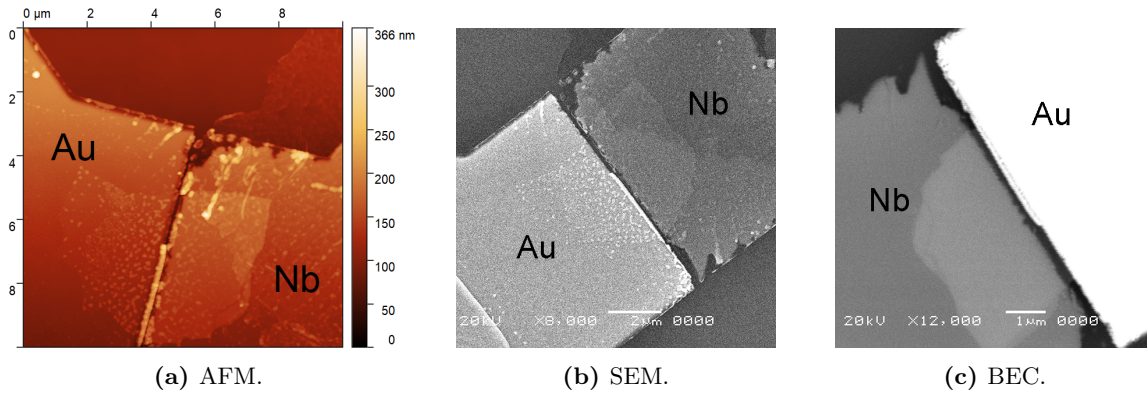


Figure 4.11: Pictures of the sample using different imaging techniques.

been observed on BSTS before. [69] To make absolutely sure nothing was touching, we then used the backscatter electron detector (BEC), in which the colours correspond to the atomic number of the material. Since Au and Nb have atomic numbers 79 and 41, respectively, Au is much heavier and therefore appears much lighter on the BEC images. In Fig. 4.11c we can clearly see that the two materials are not touching.

Weak antilocalisation

A well known phenomenon that often creates ZBCPs in TIs is weak antilocalisation (WAL). As we have seen in Section 1.3.3, this occurs in TIs as a result of spin-orbit coupling. WAL can cause a ZBCP. [70, 71] However, WAL is the strongest at zero magnetic field. In our case, the ZBCP shows up at higher field. Moreover, the peak height seems to oscillate with magnetic field (more on this in Section 4.5.1). This cannot be the case if the ZBCP would originate from WAL.

4.4.2 The peak height

A result of the famous Landauer equation for the current through a junction is that the conductance is proportional to the transparency as [72]

$$G = \frac{2e^2}{h} T(E_F), \quad (4.4)$$

where e^2/h is defined as a *conductance quantum* and $T(E_F)$ is the junction transparency (or the transmission) at the Fermi level. We note that the factor 2 in Eq. (4.4) is a result of the two spins. In the TI, we only have one spin, so it should be a factor 1. However, because of the Andreev reflection, we get an additional factor 2, such that Eq. (4.4) remains effectively unchanged.

In the case of p -wave superconductivity, it was found that that $T = 1$ (see Section 1.4.3), in which case Eq. (4.4) reduces to

$$G = \frac{2e^2}{h} N, \quad (4.5)$$

where N is the number of channels or modes through which electron transport can take place. [72] A MBS is located at zero energy, where only one channel is available. Hence, the peak height of the ZBCP originating from the MBS is always $2e^2/h$. A regular ABS is not related to p -wave pairing and therefore, Eq. (4.5) does not hold, which implies its height is not necessarily $2e^2/h$.

This can be interpreted as follows: any ABS consists of an electron and a hole (see Fig. 1.12a). Since a MBS is located at zero energy, both the electron and hole are at zero energy and both contribute one conductance quantum. Hence, this gives a total of two conductance quanta. Another interpretation is based on the Majorana being half electron and half hole. Since Majorana particles come in pairs, this gives two conductance quanta as well.

The first time the ZBCP in the nanowire experiment was reported [60], the peak height was only $0.1e^2/h$, which is 20 times smaller than the expected value. Some of the authors continued working on this project and explained seven years later that the actual peak height should actually be $2e^2/h$. [68]

In our experiments, the peak height is approximately $1.4e^2/h$. This is already in the right order of magnitude, but still slightly smaller than the required $2e^2/h$. There are, however, a couple of possible explanations.

Liu et al [67] modelled the conductance through a nanowire with spin-orbit coupling in proximity to an s -wave superconductor. Since we are recreating the nanowire experiment with a topological insulator, their theory might be applicable to our experiment as well. What has to be kept in mind is that Liu et al [67] require a certain Zeeman field for their junction to be in the topological phase. The topological insulator is already in this phase.

The main phenomenon discussed in their work is the so-called *soft gap*. As explained in Section 1.2.2, a superconductor has an energy gap. In the presence of a interface barrier, the conductance spectrum of the superconductor takes on the shape of the density of states. [47] If the conductance inside the gap goes to zero, we speak about a “hard gap”. If it has a substantial value inside the gap, this is called a “soft gap”. The condition given for a hard gap is $dI/dV \ll e^2/h$, where e^2/h is a conductance quantum. [67] Hence, we have to remove the soft gap in order for the ZBCP to become visible.

Liu et al. [67] argue that the soft gap could originate from junction transparency (i.e. the tunnel barrier), temperature, dissipation, or a combination of them. We will discuss all three of them.

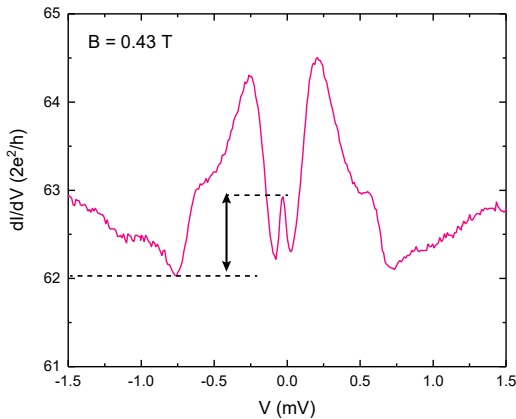
Tunnel barrier

The tunnel barrier does not harm the topological properties and therefore, the ZBCP always stays $2e^2/h$ in height in their model. [67] Tunnelling into a regular ABS on the other hand, can give a conductance between 0 and $4e^2/h$, depending on the tunnel barrier strength. [73] In the MBS case, the tunnel barrier can, however, broaden the peak without affecting the height. Liu et al theoretically show that the height is independent of the background (the soft gap), which means that the ZBCP can be tiny in height if the tunnel barrier is low and the value inside the gap is comparable to $2e^2/h$. This was confirmed experimentally by [68].

We consider the maximum observed ZBCP at 0.43 T as shown in Fig. 4.12. We can take the peak height with respect to the background inside the gap (local minimum), which gives a height of $1.4e^2/h$. However, taking the peak height with respect to the global minimum (around $V = -0.77$ mV), the peak height is $1.8e^2/h$, which is already much closer to the expected $2e^2/h$. This is in agreement with a background caused by a low tunnel barrier. If there is a tunnel barrier in the system, it is definitely expected to be small, since we did not explicitly make a tunnel barrier.

Moreover, the small barrier would also explain why we only observed the ZBCP at this specific structure. We made eight structures on the BSTS7 substrate. The fabrication was identical, but we found that the specific structure that showed the ZBCP had a slightly higher resistance than the others (170Ω as opposed to 50Ω). This indicates that this specific structure has a higher barrier and therefore, the ZBCP could stick out above the background. The values that we stated here are taken from Fig. 4.12. By making a proper fit of the gap in the absence of the ZBCP, a more precise estimate of the peak height could be given.

Experimentally, in order to make a stronger claim about the peak height, it is necessary to be able to control the tunnel barrier strength better. This will be discussed in the outlook in Section 5.3.



	V (mV)	dI/dV ($2e^2/h$)
Global min	-0.77	62.03
Local min	-0.077	62.22
Local max	-0.027	62.93
Peak height w.r.t local min		$1.4e^2/h$
Peak height w.r.t. global min		$1.8e^2/h$

Table 4.3: Values extracted from Fig. 4.12.

Figure 4.12: Maximum ZBCP at $B = 0.43$ T.

Controlling the tunnel barrier has an additional advantage. The Majorana state is defined to be located at zero energy in the density of states, not necessarily at zero voltage in the conductance (although this turns out to be the same). Experimentally, the density of states is obtained by *spectroscopy*, which is effectively probing the conductance with a high tunnel barrier. The concepts of conductance and density of states are often linked to each other, but the validity of this comparison is not trivial. The conductance is related to charge, while the density of states considers particles. In Appendix E, we show mathematically how the two can be linked via the tunnel barrier. In the absence of a tunnel barrier, we can still do spectroscopy, and still draw conclusions related to, e.g., other types of barriers in the system and whether backscattering is possible. [29] Relating the conductance spectrum to the density of states just makes the interpretation more straightforward.

Temperature and dissipation

The other two reasons why the ZBCP is smaller than $2e^2/h$ are temperature and dissipation. Contrary to the tunnel barrier, temperature and dissipation might not preserve topological properties. When increasing temperature and/or dissipation, the area of the ZBCP stays constant, i.e. the height decreases, while the peak broadens. It is difficult to say something about the peak width in our system, since Ref. [68] does not give a criterion for it and the width is likely broadened by the low tunnel barrier (as we just discussed).

Broadening of the spectrum is a well known effect of increasing the temperature, which is known as *thermal smearing*. In Ref. [68] the peak height at zero temperature is $2e^2/h$, while at 0.1 K, it has decreased to $1.7e^2/h$. Our experiments are done at 13 mK. We do not have the temperature dependence at finite field (with ZBCP), but we do have the temperature dependence at zero field, which is shown in Fig. 4.13. Considering the speed with which the peaks shrink, it is not likely that the decrease in peak height is solely caused by thermal smearing.

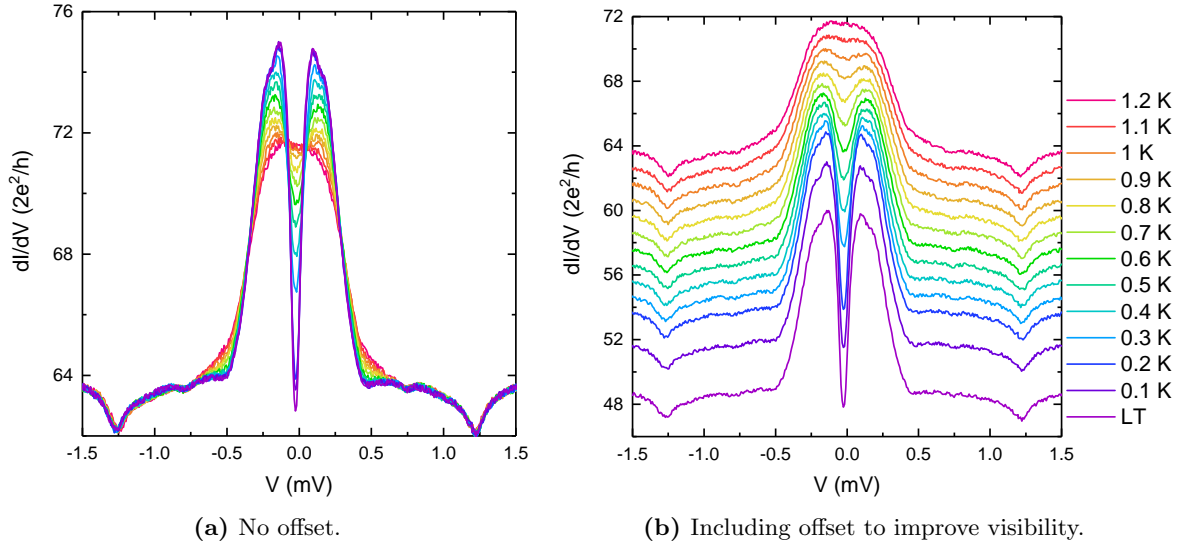


Figure 4.13: Temperature dependence of the differential conductance, at zero applied field.

Liu et al [67] state that the dissipation is of unknown origin, but it is introduced in the model in order to agree better with the experimental values. The dissipation could be explained by vortices (i.e. transport of vortices in a superconductor costs more energy) or quasi particle states in the superconductor. Since the first critical field of Nb (when vortices appear) is between the 100 and 200 mT, [74] this could very well be the case in our system as well. Since the dissipation in [67] is just a fitting parameter, it is very difficult to make a claim about the dissipation. One could imagine that increasing the magnetic field would increase the dissipation and therefore, decrease

the peak height (while increasing the peak width). However, the range where the ZBCP is observed is too small to either reject or verify this possibility.

The main difference between thermal smearing and smearing as a result of dissipation is the symmetry. Temperature effects are always symmetric in voltage, while the dissipation is asymmetric. This can be explained by the fact that temperature conserves particle-hole symmetry (Liu et al [67] show the reflection matrix is unitary), while this symmetry is broken by dissipation. This is only the case at finite voltages. The ZBCP is always particle-hole symmetric. [67] Looking closely at our experimental data in Fig. 4.9b, we could argue that the peaks for positive voltage are indeed slightly higher. If there is dissipation in the system, it is expected to be small, so a small asymmetry would be a logical result.

4.5 Magnetic field effects

In Fig 4.9b, we saw that the ZBCP is most clearly visible around 0.43 T. If we look very closely to the conductance, we can already see some very small peaks at lower fields, e.g. a peak of $0.2e^2/h$ at 0.198 T. Whether this is an actual peak or just noise is debatable. This tiny ZBCP is only visible for three data points and then disappears into the background again. Zooming in at the zero voltage level (Fig. 4.14a), one could believe that the ZBCP appears and disappears periodically as a function of magnetic field. This could be an indication of the Aharonov-Bohm effect which is also commonly seen in nanowires, [75] which will be discussed in Section 4.5.1.

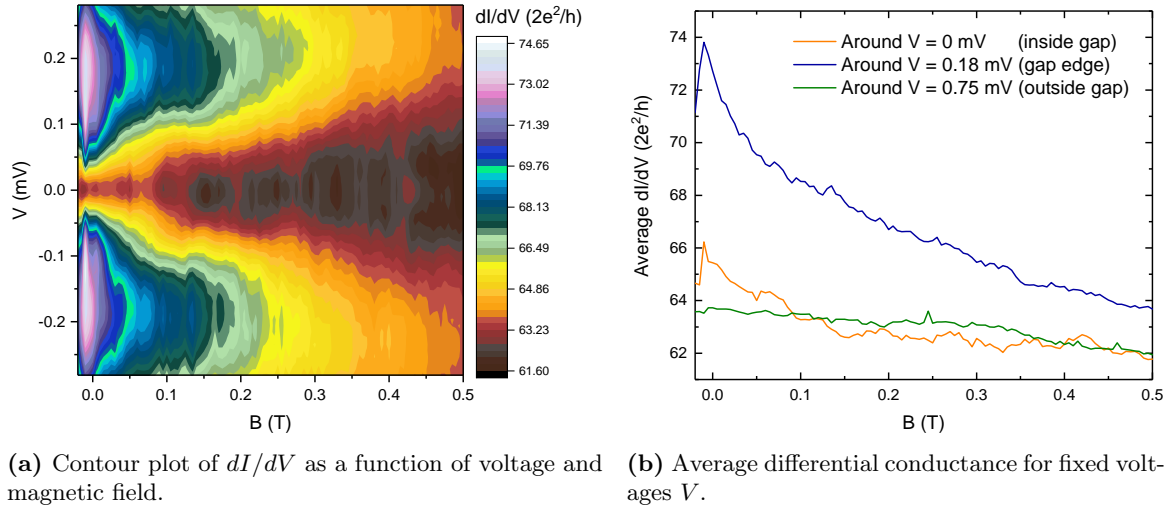


Figure 4.14: Conductance as a function of magnetic field.

The question that remains is why we do not observe the ZBCP for low magnetic fields. In a nanowire, a magnetic field is needed to get in the topological regime. Since a TI always has two states at the Fermi level, this should not be an issue and the Majorana should be visible at zero, or low, magnetic field as well. Since we do observe the ZBCP at higher fields, we expect that there is a phenomenon that simply dominates the ZBCP and this phenomenon should attenuate with increasing magnetic field. This can also be seen in Fig. 4.14b, where we clearly observe a large conductance background that goes down with increasing magnetic field.

In our setup, the resistance (which is the inverse of the differential conductance that we have discussed so far) is caused by many different effects. Transport goes through the BSTS, even though the BSTS is partly superconducting, it is still expected to somehow contribute to the resistance.

The contribution of BSTS is discussed in Section 4.5.3.

The Au contacts in this case were measured while testing the sample and were found to have a resistance of 25Ω (which is small compared to other samples that we tested). Both the BSTS and the Au are independent of the magnetic field and will be a constant offset to the resistance. Since Nb is a superconductor, these contacts do not have resistance. In Fig. 4.6, it can be seen that the samples have two Au contacts and two Nb contacts. This allows us to do four point measurements, which implies that we can eliminate any contributions of the cables or other parts of the setup.

Another field dependent phenomenon that we have already come across a couple of times is WAL (introduced in Section 1.3.3 and briefly discussed in Section 4.4.1). WAL is known to decrease with magnetic field, which is what we are looking for. We note that WAL can only exist in the diffusive regime and it is unclear in which regime we are. For the moment, suppose we have WAL in our system. Both the WAL and the MBS are quantum corrections to the conductance, which means that they are in the order of magnitude of a conductance quantum. Therefore, if the WAL correction is slightly larger than the MBS correction, it is possible that we are not able to observe the MBS at low magnetic field. However, having a look at the order of magnitude with which the conductance goes down (see Fig. 4.14b), we can immediately see that this is much larger than a conductance quantum. Therefore, even if WAL is present in this system, it cannot be responsible for a conductance decrease of this size. The possible contribution of WAL will be discussed in Section 4.5.3.

The only other obvious field dependent effect in this system is the superconductivity itself. The decrease of the coherence peak as a function of magnetic field (blue line in Fig. 4.14b) is a well-known result of superconductivity. To say a little more about how the superconductivity in this system is affected by the magnetic field, we make a simple model of it, which is discussed in Section 4.5.2.

4.5.1 The Aharonov-Bohm effect

A brief introduction to the Aharonov-Bohm effect and flux quantization was given in Section 1.2.4. The Aharonov-Bohm effect can be observed in both the ballistic and the diffusive limit, [76] which implies that we do not have to worry about the length scales mentioned at the beginning of this section.

In a nanowire, the dispersion relation is given by [75]

$$E_{kl} = \pm \hbar v \sqrt{k^2 + \frac{\pi \left(l + \frac{1}{2} - \Phi/\Phi_0\right)^2}{S}}, \quad (4.6)$$

where $l + \frac{1}{2} = \pm \frac{1}{2}, \pm \frac{3}{2}, \pm \frac{5}{2}, \dots$ is the angular momentum and S is the cross-sectional area of the nanowire. In the absence of a magnetic field (i.e. $\Phi = 0$), the nanowire is in the trivial phase, which implies that the dispersion has a gap. Sending a conductance quantum (or two, or three, ...) through the wire cancels the angular momentum contribution in Eq. (4.6), such that the dispersion simply becomes $E_k = \pm \hbar v k$. The gap closes and we are able to have a MBS (see also Section 1.4.3). This is depicted schematically in Fig. 4.15. This happens for every integer amount of conductance quantum. Hence, the appearance of the MBS oscillates with magnetic field in a nanowire. [75]

The next step is to link the nanowire case to our system. To get some insight in the order of magnitude, we want to calculate the flux through our system, which is equal to $\Phi = B \cdot S$ (see Section 1.2.4), where B is the period with which the ZBCP oscillates as function of the applied magnetic field, and S is the area.

We will first make an estimate of the required value for B . Since we do not have many data points, the data looks a bit noisy. The data will profit from some averaging and smoothing. We average over eleven data points centred around $V = 0$ (which corresponds to the range $V = -0.047$ to 0.047 mV). The result looks like a periodic function multiplied with a decreasing function, which

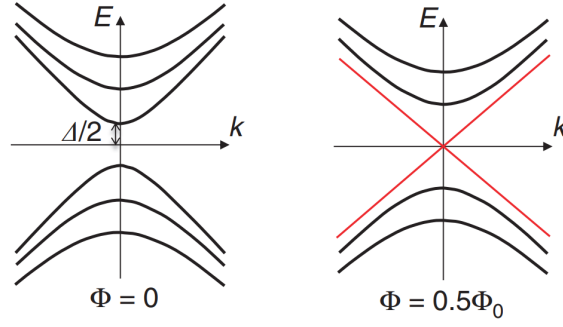
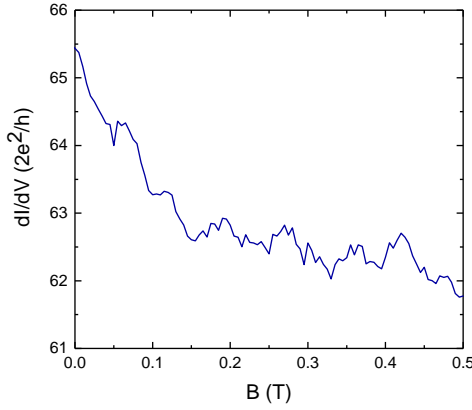
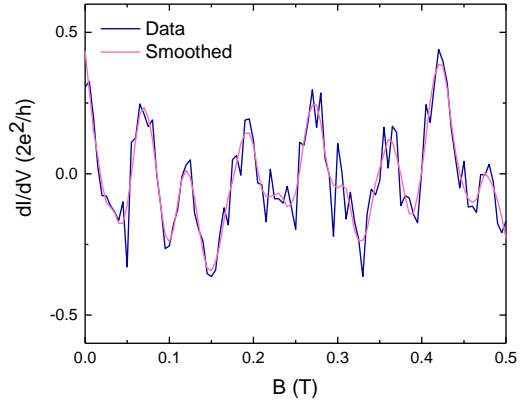


Figure 4.15: The dispersion of a nanowire in the absence of a magnetic field has a gap (left). When sending exactly $\Phi = 0.5\Phi_0$, the gap closes (right). From [75].

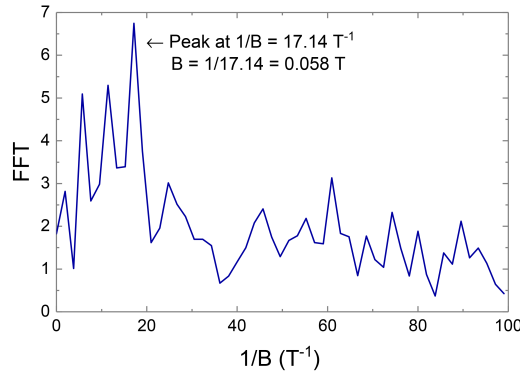
is shown in Fig. 4.16a. We are interested in the periodic component and therefore, we subtract the decreasing background. We do this by severely smoothing the data (which eliminates the periodic part) and subtracting the smoothed graph from the original one. The resulting graph and a smoothed version of it (to emphasize the periodicity) are depicted in Fig. 4.16b. Taking the Fourier transform in Fig. 4.16c, we find a maximum at 0.058 T, which can also be estimated from the smoothed pink graph in Fig. 4.16b.



(a) After averaging.



(b) After averaging + background subtraction.



(c) Fast fourier transform of the data in panel b.

Figure 4.16: Differential conductance averaged around $V = 0$.

We now have to make an estimate of the area S of the MBS. We note that, from the dispersion of the nanowire (Eq. (4.6)), it follows directly that the area S does not influence the closing of the gap. It only determines the size of the gap. The area S in our system is related to the size of the SABS. This is illustrated in Fig. 4.17. From the AFM image, we estimate that the distance between the

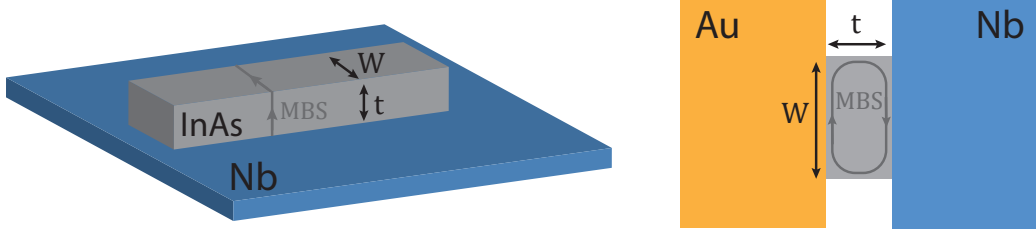


Figure 4.17: The width (W) and thickness (t) in a nanowire (left) and in our system (right).

two contacts (t) is approximately 50 nm. From the SEM image, we estimate the width of the Au wall (W) to be $3 \mu\text{m}$, although it is not clear if the full Au wall is contributing to the conductance.

The flux Φ through our artificial loop is found to be

$$\begin{aligned}\Phi &= B \cdot S = B \cdot t \cdot W = (0.058 \text{ T}) \cdot (50 \cdot 10^{-9} \text{ m}) \cdot (3 \cdot 10^{-6} \text{ m}) \\ &= 9 \cdot 10^{-15} \text{ Tm}^2.\end{aligned}\tag{4.7}$$

The numbers that we used here are very rough estimates and just estimated by eye. Therefore, the value of Φ is a very rough estimate as well. A flux quantum is $\Phi_0 = h/2e = 2 \cdot 10^{-15} \text{ Tm}^2$. Hence, the value that we found for Φ is in the right order of magnitude, although it is still too high. The most probable reason why the obtained value is higher, is because we took $W = 3 \mu\text{m}$, which may be too large. It is very probable that the flake has some terraces. In this case, the MBS would most likely be confined within a terrace, rather than taking an additional step.

Of course, this approach is very speculative and the data is not clear enough to make any claims. The only thing that we can state so far is that the SABS which might cause an artificial loop is a reasonable idea and it is definitely worth it to investigate this theory in more detail. As we already explained in the previous section, by increasing the tunnel barrier, the visibility of the ZBCP should increase, and, therefore, its period as a function of magnetic field will become clearer as well. By intentionally designing structures with a smaller distance between the contacts (around 50 nm), there is a good chance that at least some of the structures will have successful alignment and lift-off, in which case the area of the loop S can be estimated more precisely.

4.5.2 The Doppler shift

Ideally, one would model a superconducting TI and put it in contact with a normal metal. The former has linear dispersion and is described by a first order differential equation, while the latter has quadratic dispersion and therefore corresponds to a second order differential equation. Since the number of required boundary conditions is equal to the order of the differential equation, it remains unclear how to couple the two. Hence, we have to look for an alternative way to model the system.

The first suggestion to model the system was by simply taking the BTK theory which describes a normal metal s -wave superconductor junction. [47] In the absence of a barrier, the resulting conductance spectrum gives a plateau inside the gap. Imposing an interface barrier gives rise to very sharp coherence peaks (located at $E = \pm\Delta$) and suppresses the conductance inside the gap (i.e. a soft gap, as explained in Section 4.4.2). Especially the coherence peaks are very different from the conductance spectra that we experimentally observed. It would not be possible to get an accurate

fit using just the simple BTK model.

In order to improve the model, while still keeping it simple, we used an available code for a normal metal/ferromagnet/superconductor junction with different types of superconductivity, modelled by Olde Olthof et al. [37] We took the ferromagnet to be absent, replaced the s -wave superconductor by a chiral p -wave superconductor and introduced strong SOC to mimic the TI behaviour. We have to take this model with a grain of salt, since it is not specifically made to describe our system. Since we are only interested in the qualitative structure and it is not our goal to perfectly fit the data, we simply assumed all masses to be equal and the system to be isotropic.

We first check the influences of the SOC and the barrier strength separately. Both suppress the conductance and induce a soft gap, as can be seen in Figs. 4.18a,b. The shape is slightly different and the suppression as a result of the barrier is stronger. We are looking for a conductance spectrum where the conductance inside the gap is at approximately the same level as the conductance outside the gap. This can be modelled by several combinations of the SOC and barrier strength. In our system, we expect the SOC to be considerably stronger than the barrier strength. Hence, we fix the SOC to be equal to 1 and found the matching barrier strength to be 0.2, as can be seen in Fig. 4.18c. Both the SOC and interface barrier are normalised by a factor $m/\hbar^2 k_0$, where m is the effective mass and $k_0 = \sqrt{2m\mu}/\hbar$, with μ the chemical potential. [37]

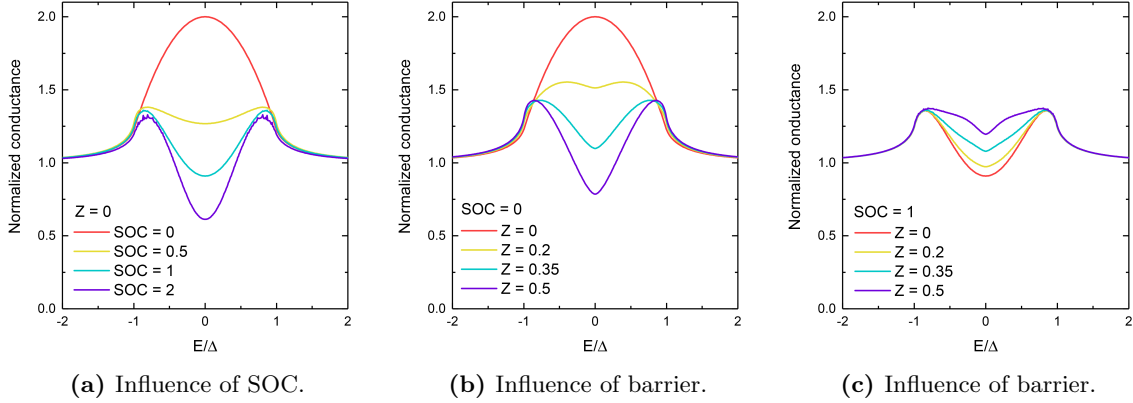


Figure 4.18: Influence of SOC and the barrier strength on the normalized conductance.

Using these parameters, we then model the conductance for increasing magnetic field. The experimental data and the modelled conductance are shown in Figs. 4.19a,b.

The theoretical conductance catches the rounded shape of the peaks much better than the standard BTK model. This indicates possible p -wave pairing in the system. When increasing the field, the coherence peaks become broader and get a shoulder (purple graphs). This feature is mimicked very well by the model. In this model, the SOC is simply a spin dependent barrier, i.e. the barrier is low for one spin and high for the other. Since the model is simply an adjusted model (not made specifically to fit this experiment), this approach is not very accurate. In the case of a TI, we have only one spin, so the barrier should go to infinity. On top of that, it should not be modelled at the interface, but it is present inside the materials in the form of linear dispersion. From Fig. 4.18a, we can see that the SOC does not affect the coherence peaks that much, but mainly suppresses the subgap conductance. Therefore, the formation of the shoulder probably results from the p -wave pairing instead (and is not a direct result of the SOC). This was confirmed by repeating the calculation without SOC, where a shoulder is still vaguely visible for increasing magnetic field (Fig. 4.19c).

However, the problem with the theoretically obtained conductance is that it goes up at zero energy, while the experimental conductance goes down (most clearly visible in Fig. 4.14b).

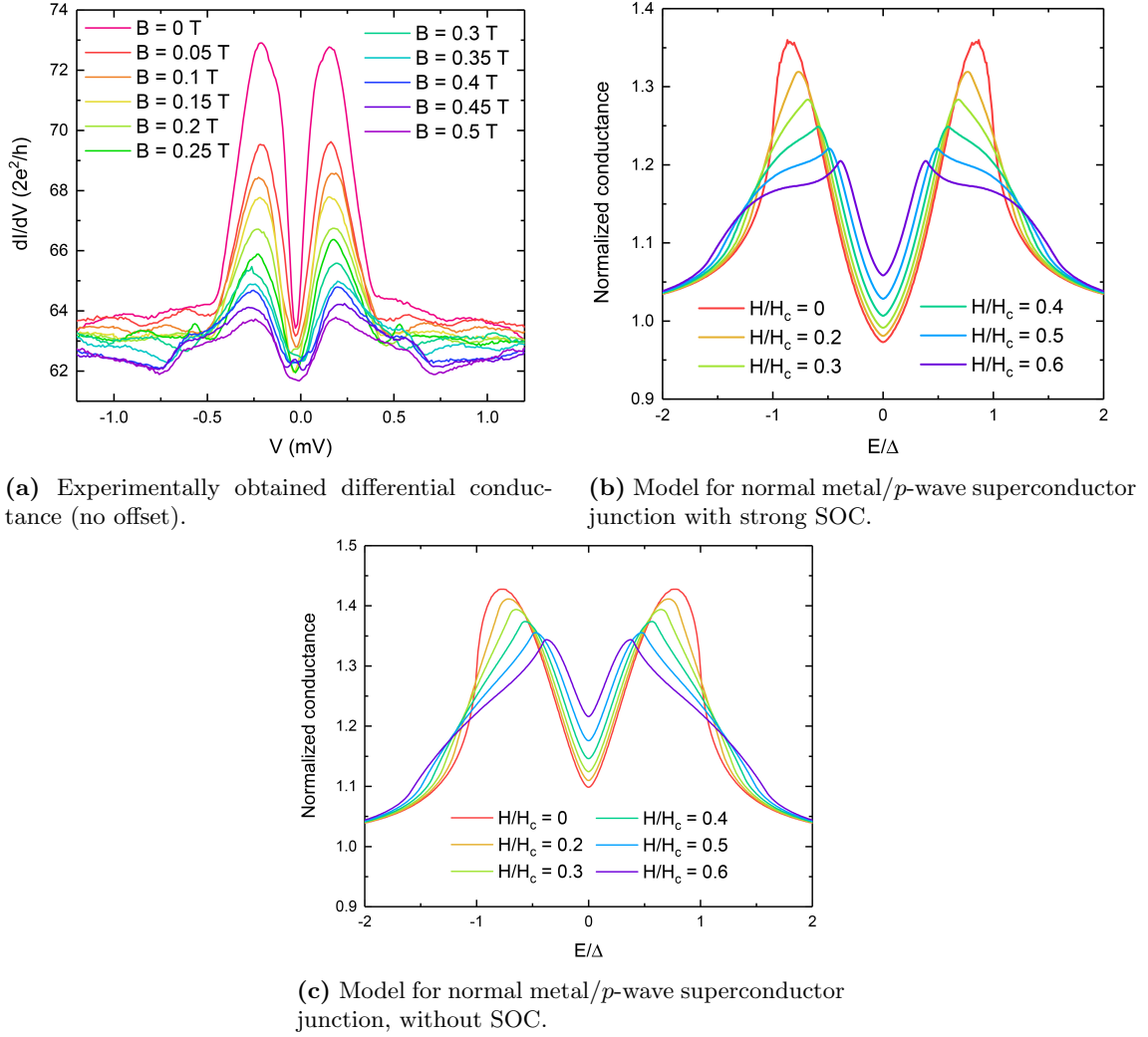


Figure 4.19: Conductance as a function of magnetic field.

The two main effects that the magnetic field can have on the superconductivity are the Doppler shift and the Zeeman effect. The Doppler shift is a magnetic field dependent offset to the kinetic energy. The Zeeman effect splits the energy levels linearly with increasing magnetic field. Which effects is present in a system depends on the material parameters.

Bismuth based topological insulators have a g -factor of approximately 20 along the c -axis, [77] which results in a Zeeman energy of $E_Z = g\mu_B B = 20 \cdot (9.2 \cdot 10^{-24} \text{ JT}^{-1}) \cdot (0.5 \text{ T}) = 0.57 \text{ meV}$. The Doppler effect is of the order of the superconducting gap, [37] which in this case is approximately 0.25 mV. Since the charge carriers are Cooper pairs, we have to multiply by 2e to find that the corresponding energy is 0.5 meV. Hence, the two effects are of the same order and non-negligible.

The model from Ref. [37] only includes the magnetic field via the Doppler shift. Furthermore, it is only suitable for modelling small magnetic fields, since it does not take Abrikosov vortices into account which are expected at higher magnetic fields (see Section 1.2.1). Therefore, the theoretical formation of the shoulder in in Fig. 4.19b in our model solely results from the Doppler shift.

This might also explain why the overall conductance is not going down as a function of the magnetic field. The decreasing conductance could be a result of the Zeeman effect, although further calculations have to be done to confirm this. Alternatively, it can be caused by WAL, which we

will discuss in the next section.

Finally, we can get some additional information from the model. The normalization factor H_c is the thermodynamical critical field. The coherence peaks in the Fig. 4.19a correspond to the induced superconductivity in the BSTS, of which the critical field values are unknown. Comparing the data to the theory, we can estimate that a field of $B = 0.5$ T corresponds to 60% of the critical field, such that H_c of BSTS is estimated to be around 0.8 T.

4.5.3 Weak antilocalisation

In order to say something about WAL in our system, we have to try to stay away from effects resulting from superconductivity. Ideally, we would use data at a slightly higher temperature, when there is no superconductivity in the system any more, for example, at 10 K (since Nb transitions to the normal state around 9 K). Since this data is not available, we consider the conductance outside the BSTS gap (for voltages $|V| > 0.5$ mV). This has the additional risk that sending a larger current through the sample will slightly heat up the electrons (depending on the resistance of the sample), which makes the fit less accurate. This is especially an issue because one of the fitting parameters, the phase-coherence length ℓ_ϕ is temperature dependent. [29] On top of that, we are still dealing with the superconducting Nb, so we do not expect to get a great WAL fit through our data.

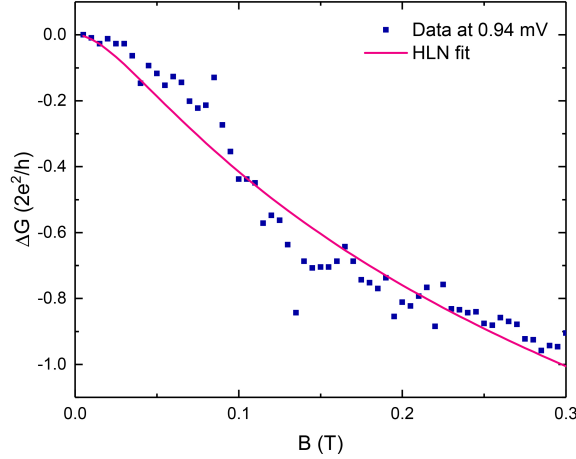


Figure 4.20: Fitting the HLN equation through the conductance as a function of magnetic field.

WAL as a function of a perpendicular magnetic field (B_\perp) is modelled by the Hikami-Larkin-Nagaoka (HLN) equation [78]

$$\begin{aligned} \Delta G(B_\perp) &= G(B_\perp) - G(B_\perp = 0) \\ &= \alpha \frac{e^2}{\pi h} \left[F \left(\frac{1}{2} + \frac{\hbar}{4e\ell_\phi^2 B_\perp} \right) - \ln \left(\frac{\hbar}{4e\ell_\phi^2 B_\perp} \right) \right], \end{aligned} \quad (4.8)$$

where F is the digamma function, ℓ_ϕ is the phase-coherence length (see Section 1.3.3) and α is a fitting parameter which is typically $\alpha = 1$ for WL and $\alpha = -0.5$ for WAL. [29] In the case of multiple conducting channels, every channel contributes $\alpha = -0.5$ for WAL.

A HLN fit was made for data around 0.94 mV, which is shown in Fig. 4.20. The optimal parameters were $\ell_\phi = 103$ nm and $\alpha = -5.12$. In BSTS, we would expect at least a conducting channel for the top and the bottom surface (two channels, $\alpha = -1$). In the case of high doping, there can be a few more channels, although we should assume there is no scattering between them,

otherwise the value of α reduces. A fitting parameter of $\alpha = -5$ points at ten conducting channels, which is very unlikely. However, similarly large values of α for BSTS have been obtained before. [69] A possible reason might be that the HLN fit is not very suitable for BSTS. The HLN equation is known to give the wrong value of α in the absence of backscattering. In this case, α is doubled compared to conventional electrons (recall the factor 2 in Eq. (4.5)). [79] Hence, it could be the case that WAL in this system slightly suppresses the conductance, although this fit is not conclusive.

4.5.4 Structure outside the gap

In the previous sections, we focussed on the gap shape and the things happening inside the gap. At certain applied magnetic fields, we can also observe some additional small peaks outside the BSTS gap (but still inside the Nb gap), which is shown in Fig. 4.21. Since these structures are located outside the BSTS gap, they are not related to the induced superconductivity in the BSTS. Hence, they probably originate from the Nb.

At $B = 0.25$ T, we can see two smaller peaks at $V = -0.83$ mV and $V = -0.57$ mV. For higher magnetic fields, we expect the Nb gap to decrease in size and only one peak remains. However, at most intermediate values of the magnetic field, there are no additional peaks at all.

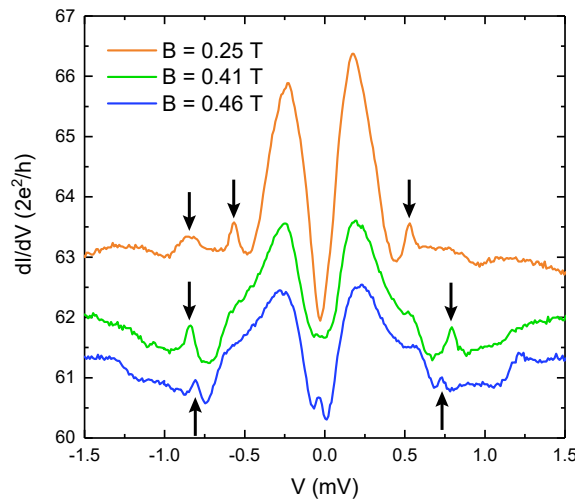


Figure 4.21: At certain values of the magnetic fields, small structures can be observed outside the BSTS gap (marked by black arrows). The bottom two graphs have an offset to improve visibility.

Most likely, the additional peaks are the result of some resonance inside the Nb gap. At certain values of the magnetic field, the Nb gap size probably corresponds to the wave length of some physical phenomenon, which allows for standing waves, giving rise to small peaks in the conductance. Fully modelling and explaining the additional peaks goes beyond the scope of this work. However, an extensive discussion on similar peaks in BSTS is given in Ref [80].

4.6 $\text{Bi}_{0.97}\text{Sb}_{0.03}$

Pure bismuth (Bi) is a semimetal, which means it has a small (or zero) bandgap. When doping Bi with antimony (Sb), the conduction band shifts to a lower energy while the valence band increases in energy, such that the two bands approach each other. Bismuth antimony ($\text{Bi}_{0.97}\text{Sb}_{0.03}$) is a so-

called *accidental Dirac semimetal*. [81] For a Sb doping of 3-4%, the bands of the semimetal happen to touch each other, which creates a Dirac cone.¹ This is the type of $\text{Bi}_{0.97}\text{Sb}_{0.03}$ that is of interest in our experiments. Increasing the Sb doping even further results in a band inversion (similar to the case with topological insulators in Section 1.3.1).

Since the 4π periodicity measurements were done using $\text{Bi}_{0.97}\text{Sb}_{0.03}$, [38] it would be interesting to see if we can also show the Majorana behaviour by means of a ZBCP.

Since $\text{Bi}_{0.97}\text{Sb}_{0.03}$ is a Dirac semimetal (instead of a topological insulator), it has linear dispersion in three directions (instead of two). Therefore, $\text{Bi}_{0.97}\text{Sb}_{0.03}$ is more robust against perturbations, such that the MBS is able to travel further and should be easier to observe. The signal from a possible MBS should be much clearer and allows for length dependent designs (varying the distance between the Au and Nb).

In practice, $\text{Bi}_{0.97}\text{Sb}_{0.03}$ is a lot harder to work with than BSTS. First of all, $\text{Bi}_{0.97}\text{Sb}_{0.03}$ is a very hard material. Sticking tape to BSTS easily gives hundreds of tiny flakes (a few μm in lateral size). If we are lucky, $\text{Bi}_{0.97}\text{Sb}_{0.03}$ gives a couple of flakes. These are, in general, a lot thicker and a lot larger (ranging from a few μm to a few mm) than the BSTS flakes. Especially the desired thin flakes are rarely large enough to put a structure on them.

Because we have very few and very large flakes, we made several structures on one flake. This can be seen in the images in Fig 4.22. Since Au lift-off can be difficult, we decided to make only one Au contact and several Nb contacts around it. Furthermore, in this design we made the Nb contacts such that they have a different angle with respect to the Au contact, to test whether the transport through the flake is directional. For all three Nb contacts, the distance to the Au contact is 1 μm .

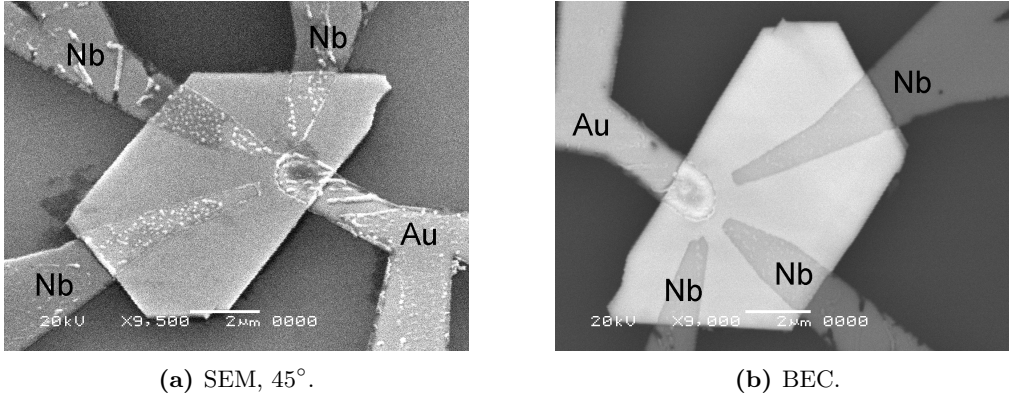


Figure 4.22: Images of a large $\text{Bi}_{0.97}\text{Sb}_{0.03}$ flake with Nb and Au contacts on it.

$\text{Bi}_{0.97}\text{Sb}_{0.03}$ is a hard material, which not only makes it difficult to exfoliate, but the etching is challenging as well. This results in contacts with a low transparency. Considering the influence of the tunnel barrier (see Section 4.4.2), this is in principle not a bad thing. It does, however, come with some additional difficulties. Since the flake is quite thick and the etching is not very successful, the Nb turned out to be discontinuous at the edge of the flake. This is visible in the bottom left corner of Fig. 4.22a. In the same picture, the Nb on top of the $\text{Bi}_{0.97}\text{Sb}_{0.03}$ has a strange, dotted structure, which made us doubt if there was any Nb left on the flake at all. By making a BEC image (Fig. 4.22b), we could see that this was not an issue. In the top right corner of Fig. 4.22b, it can again be seen that the contact is discontinuous. Comparing this image to the BEC image of BSTS (Fig. 4.11c), it also becomes clear that the $\text{Bi}_{0.97}\text{Sb}_{0.03}$ is a lot heavier. Obviously, the discontinuous contact implies that it is not possible to send a signal through. The discontinuity could be solved by making the Nb thicker. The downside is that this will also make the lift-off more

¹We note that is not a standard property of semimetals. The bands can only touch if they have the same spin structure. If this is not the case, the semimetal exhibits band avoidance instead of band crossing.

difficult.

On some of the flakes, we did manage to get good contacts. When checking the resistance in the probe station, we found reasonable values in the $\text{k}\Omega$ range. We had to wait for a couple of weeks before we were able to measure our sample at a dilution fridge. When we had loaded the sample in the measurement setup, it turned out that the resistance had gone up considerably. Some of the contacts were open, other had barriers in the $\text{M}\Omega$ range. This is most likely the result of the $\text{Bi}_{0.97}\text{Sb}_{0.03}$ degrading very fast, possibly even underneath the contacts. Because of this, we have not yet managed to do any successful measurements on the structures with $\text{Bi}_{0.97}\text{Sb}_{0.03}$.

Conclusions and outlook

5.1 Conclusions on theoretical work

We modelled the transport through both conventional and topological Josephson junctions. The current through this type of junction is determined by the interplay of Andreev reflections at the interfaces with the superconductors, and a scattering region in the middle. This combination results in multiple Andreev reflections. Since every reflection depends on the previous, the reflections are described by recurrence relations.

Every time an electron can overcome the energy gap by performing $n - 1$ Andreev reflections, current starts to flow. In the conventional case, this gap is 2Δ . A topological Josephson junction also has a midgap state, such that the energy to overcome is only Δ . If we include an extra dimension, the energy gap depends on the angle θ_S , which is a measure for the Fermi surface mismatch between the topological insulator and the superconductor. Hence, the Fermi surface mismatch determines the transparency of the junction.

As a result of multiple Andreev reflections (MAR), a small oscillation in the current is visible at applied voltages V , when

$$\begin{array}{ll} \text{S/N/S junction in 1D} & eV = \frac{2\Delta}{q}, \\ \text{S/TI/S junction in 1D} & eV = \frac{\Delta}{q}, \\ \text{S/TI/S junction in 2D} & eV = \frac{\Delta(1 + \sin \theta_S)}{q}, \quad q \in \mathbb{N}. \end{array}$$

These points coincide with singularities in the recurrence relation. We wrote the recurrence as $y_{n+1} + \gamma_n y_n + \chi_n y_{n-1} = 0$, with coefficients γ_n and χ_n . The coefficient γ_n increases quadratically with n , (i.e. $\gamma_n \sim n^2$), which implies that the recurrence is very instable.

This can be solved by using a backward recurrence algorithm, which always gives the desired minimal solution, although it is much slower than the highly optimized backslash operator that is built-in in Matlab. When executing the integration, we carefully integrated from one instability to the next, using an adaptive Simpson's method.

The condition on eV for the S/TI/S junction in 2D provides a new characteristic that can serve as a prediction for experiments. The MAR oscillations in the DC current shift with the Fermi surface mismatch between the topological insulator and the superconductor. In actual experiments, it is

not possible to measure the current for a single angle. Instead, the observed current is the average over all possible angles in which the current can go from one contact to the other. After angle averaging, the oscillating structure is hardly visible. This provides insight into why it is difficult to observe MAR and why most of the time, the experimentally obtained DC current looks like a rather smooth graph.

In the absence of an applied voltage, the Andreev reflections result in a bound state. For the S/TI/S junction in 1D, it was already known that there could be a MBS at zero energy. We have demonstrated for the first time that, in 2D, this bound state can deviate from zero energy. The corresponding bound state energy was found to be $\varepsilon = \pm\Delta \sin \theta_S$, which corresponds to the bound state that is found in chiral p -wave superconductors. This shows that it is possible to induce triplet pairing in a S/TI/S junction.

The shifting MAR structure and the bound state energy are remarkable finds which have not been seen before. At the moment of writing, these results are being prepared for publication.

5.2 Conclusions on experimental work

We measured the differential conductance through a Au/BSTS/Nb junction as a function of bias voltage, magnetic field and temperature. The BSTS gave two large coherence peaks around ± 0.25 mV. With increasing magnetic field, the coherence peaks went down and at certain magnetic fields, a small ZBCP was visible. The maximum height of this peak was $1.4e^2/h$ at a field of 0.43 T.

If this peak corresponds to a MBS, it should have a constant height of $2e^2/h$. However, there is no explicit barrier in the system. The only barrier in this system is a consequence of the distance between the Au and Nb contact, and of the bad interface with the Au. This type of barrier is small (smaller than an actual tunnel barrier) which results in a soft gap, which could partly cover the ZBCP.

Since the distance between the Au and Nb turned out to be only 50 nm, it is possible to have a SABS in between them (which can be linked to the MBS). Fixing the bias voltage to $V = 0$, the conductance as a function of magnetic field looked like a decaying function multiplied with a small oscillation (Fig. 4.16a). This oscillation is too small to draw any definitive conclusions from it. A speculative explanation is that the oscillation corresponds to an integer number of flux quanta going through the SABS, resulting in the Aharonov Bohm effect. This has also been observed in nanowires and therefore, this implies that we have mimicked a nanowire in our system.

The decrease in conductance as a function of magnetic field is most likely the result of several combined effects. Superconductivity itself is strongly suppressed by the magnetic field. In our system, both the Zeeman effect and the Doppler shift are non-negligible. By making a model, we showed that the Doppler shift can explain the formation of the shoulder for higher fields. The Zeeman effect is possibly responsible for the overall suppression, as well as a small contribution from WAL.

5.3 Outlook

To get a better idea of what is going on in the system, it is necessary to control the tunnel barrier better. This reduces the soft gap background which partly masks the ZBCP, such that the full height becomes visible. If the system truly shows the Aharonov Bohm effect, the oscillations will become more distinct with a higher tunnel barrier.

We have seen in Section 4.3.2 that the barrier is quite delicate and needs to be handled extremely carefully. Up until now, we have sputtered the Au on top of the tunnel barrier by means

of slow deposition. This might still be too violent for the fragile barrier. Even though the slow deposition did not completely destroy the barrier, some Au particles have probably penetrated the tunnel barrier, thereby weakening it and making it more sensitive to static electricity during wire bonding.

A more controlled way to obtain a Au layer would be evaporating it instead. Another possibility is creating a tunnel barrier without a layer of oxide Al_2O_3 , by means of performing controlled oxidation. This can be done by first etching into the flake inside the sputter deposition chamber, then putting it into the loadlock and letting it oxidise by means of a controlled oxygen flow. After that, we can put it in the chamber again and sputter deposit the desired material on it. This full process happens in situ.

It would also not be a bad idea to start with a slightly thicker barrier. This would eliminate the soft gap completely, such that the ZBCP will become more clearly visible. [67] On top of that, a tunnel behaves like a capacitor. Since the maximum energy a capacitor can store before breaking down is linearly dependent on its thickness, [82] a thicker barrier would be less prone to being destructed by static charge. The tunnel barrier does not harm the topological properties, so increasing it should not influence the ZBCP itself. The only risk is the barrier becoming too high, in which case tunneling is impossible and we will not be able to measure a signal through the junction. Etching before growing the Au should be avoided when we want to use the tunnel barrier.

In any case, the tunnel barrier remains the most vulnerable part of the junction and it is still recommended to bond the sample with great care.

When trying to explain the influence of the magnetic field on the superconductivity, a simple modification was made to an existing model. Although this gave some insight in the Doppler shift, it is not the most suitable model for this system. It would be better to model a real topological insulator (instead of a normal metal with strong SOC at the interface) and include the Zeeman effect in the calculations as well.

Finally, to be certain that we are dealing with a MBS, the ZBCP has to satisfy two criteria. Besides having a constant peak height of $2e^2/h$, it has to be robust in the presence of a back-gate voltage as well. This has not been checked yet.

Acknowledgements

Next week, it has been a year since I started - with a jetlag at the time - my graduation adventure at ICE/QTM. It has been a very educational and fun period to which I will always think back fondly.

First of all, I would like to express my appreciation to Alexander Brinkman for giving me the opportunity to perform research at his group. I could stop by your office at any time to discuss my results. Your enthusiasm (even at times when I had no idea what I had just calculated) was very motivating and you always provided me with new and original suggestions. For the mathematical part of my project, Jaap van der Vegt has been of great help. You helped me to understand my numerical code at a deeper level, which has resulted in beautiful, stable graphs that I can present with confidence. Furthermore, I would like to thank Geert Brocks and Christoph Brune for being part of my graduation committee, and for making the effort of reading this slightly overweight thesis.

The person who I worked with on a daily base was Bob de Ronde. Thank you very much for teaching me how to fabricate and measure samples, for the discussions on my experimental work and for helping me out with my least favourite task - the bonding. You are great at explaining things and were always very patient with me. I am also very thankful to Chuan Li for her help, suggestions and advice during the measurements and the interpretation of them. You have significantly improved my insight in how to conduct a proper experiment.

Frank Roesthuis and Dick Veldhuis, I very much appreciate your help in the lab. You introduced a lot of machines to me that looked slightly daunting at first sight. You were always willing to help and explain things, even if I was doing something incredibly silly, like rotating a screw in the wrong direction. I'm also very grateful to Jorrit de Boer for helping me out at the most unusual times. On public holidays and during nightly visits to the lab, he was always available to help me out. Jorrit, thank you for working together on the (very frustrating) $\text{Bi}_{0.97}\text{Sb}_{0.03}$ samples as well. Daan Wielens, thanks a lot for making AFM and SEM images of my samples.

I would like to thank Shu Suzuki, Sasha Golubov, Liesbeth Mulder and Jorrit de Boer for the fruitful theoretical discussions. Shu, your notes were really helpful when figuring out small details of my calculations. I would like to thank Liesbeth in particular for the many times she brought me back on earth when I was absorbed in Hilbert space again. Martijn Lankhorst, I'm grateful for your help with tracking down the instabilities in my code. Thanks to you, my code suddenly ran a lot faster.

During the writing process of my thesis, I received a lot of help and support from my fellow office inhabitants. Including Sander Smink; thanks for helping me formulate difficult English sentences and for offering "schuimblokken" on a daily base. On a similar note, I would like to thank Liesbeth for enjoying hot chocolate with me every day after lunchtime (and sometimes more often). I'm

happy to see that more and more group members are copying this unhealthy, yet delicious, habit of mine. I'm grateful to Daan for helping me during the many times I had computer trouble.

I've spent an absolutely fabulous time at ICE/QTm! I'm definitely going to miss the twaddling, fooling around, the cakes (and the corresponding nagging about the cakes), the cryptic puzzles, the "escalatiemix" on Fridays and the pleasant atmosphere in general. I have fond memories of the sailing trip, the World Cup pool (although I prefer not to discuss the results of that) and the random dinners I shared with many of the group members. I also very much enjoyed the ICE band rehearsals, consisting of Bob, Daan, Martijn, Pim and Sébastien, where I had the honour of playing the piano. I sincerely hope that I can collaborate with the ICE/QTm group again in the future. Or perhaps we will see each other at a conference, anywhere in the world. In that case, I will make sure we will have a beer together.

Finally, I would like to thank my parents, Herman and Karin, and my (not so) little brother Rens. Thank you very much for always supporting and encouraging me, both related to my studies and to other aspects of my life. You were always proud of me and my achievements (even though you had probably no idea what they were exactly). Without you, I would never have been able to successfully complete two Master's degrees. Thanks!

Appendices



Recurrence relations for the S/N/S junction

We consider the superconductor/normal metal/superconductor junction. The normal metal is divided into two regions (left and right of the eV jump). The wave amplitudes in these regions are related by the scattering matrices as follows

$$\begin{aligned} \begin{bmatrix} B_n \\ C_n \end{bmatrix} &= S_e \begin{bmatrix} \delta_{n0} + a_{2n}A_n \\ a_{2n+1}D_n \end{bmatrix}, & S_e &= \begin{bmatrix} r & t \\ t & -r^*t/t^* \end{bmatrix}, \\ \begin{bmatrix} A_n \\ D_{n-1} \end{bmatrix} &= S_h \begin{bmatrix} a_{2n}B_n \\ a_{2n-1}C_{n-1} \end{bmatrix}, & S_h = S_e^* &= \begin{bmatrix} r^* & t^* \\ t^* & -rt^*/t \end{bmatrix}. \end{aligned}$$

From these matrices, we obtain a system of equations with four unknowns A_n , B_n , C_n and D_n :

$$B_n = r [\delta_{n0} + a_{2n}A_n] + ta_{2n+1}D_n, \quad (\text{A.1})$$

$$C_n = t [\delta_{n0} + a_{2n}A_n] - \frac{r^*t}{t^*} a_{2n+1}D_n, \quad (\text{A.2})$$

$$A_n = r^*a_{2n}B_n + t^*a_{2n-1}C_{n-1}, \quad (\text{A.3})$$

$$D_{n-1} = t^*a_{2n}B_n - \frac{rt^*}{t} a_{2n-1}C_{n-1}. \quad (\text{A.4})$$

We have obtained the system of Eqs. (A.1)-(A.4) with four unknowns A_n , B_n , C_n and D_n . We are interested in A_n and B_n , since these coefficients are used for calculating the current through the junction. In this section, we will first substitute them into one another to find an expression solely depending on B_n . After this relation is obtained, B_n can be considered known. We then derive an expression depending only on A_n and B_n (such that A_n is the only unknown in this expression).

A.1 Recurrence relation for B_n

Our first goal is to find the recurrence relation for B_n . Hence, we want to get rid of the A_n and D_n . Instead of D_{n-1} , we want the equation for D_n . Hence, in Eq. (A.4), we replace $n-1$ by n :

$$D_n = t^*a_{2n+2}B_{n+1} - \frac{rt^*}{t} a_{2n+1}C_n. \quad (\text{A.5})$$

We substitute Eqs. (A.3) and (A.5) into Eq. (A.1):

$$B_n = r [\delta_{n0} + a_{2n} (r^*a_{2n}B_n + t^*a_{2n-1}C_{n-1})] + ta_{2n+1} \left(t^*a_{2n+2}B_{n+1} - \frac{rt^*}{t} a_{2n+1}C_n \right).$$

Removing the brackets, we get

$$B_n = r\delta_{n0} + rr^*a_{2n}^2B_n + rt^*a_{2n}a_{2n-1}C_{n-1} + tt^*a_{2n+1}a_{2n+2}B_{n+1} - rt^*a_{2n+1}^2C_n.$$

Sorting the terms, we obtain

$$[1 - rr^*a_{2n}^2]B_n - tt^*a_{2n+1}a_{2n+2}B_{n+1} = r\delta_{n0} + rt^*a_{2n}a_{2n-1}C_{n-1} - rt^*a_{2n+1}^2C_n. \quad (\text{A.6})$$

We now have a recurrence relation for B_n in terms of C_n . We would like to remove C_n from the equation. In order to do so, we rewrite the equation as follows, which will turn out to be convenient later on:

$$t^*a_{2n}a_{2n-1}C_{n-1} + \delta_{n0} = t^*a_{2n+1}^2C_n + \frac{1}{r}[1 - rr^*a_{2n}^2]B_n - \frac{tt^*}{r}a_{2n+1}a_{2n+2}B_{n+1}. \quad (\text{A.7})$$

We substitute Eqs. (A.3) and (A.5) into Eq. (A.2):

$$C_n = t\delta_{n0} + ta_{2n}(r^*a_{2n}B_n + t^*a_{2n-1}C_{n-1}) - \frac{r^*t}{t^*}a_{2n+1}\left(t^*a_{2n+2}B_{n+1} - \frac{rt^*}{t}a_{2n+1}C_n\right).$$

Removing the brackets, we find

$$C_n = t\delta_{n0} + tr^*a_{2n}^2B_n + tt^*a_{2n}a_{2n-1}C_{n-1} - r^*ta_{2n+1}a_{2n+2}B_{n+1} + r^*ra_{2n+1}^2C_n.$$

Again, we want to obtain an expression for C_{n-1} , which we do as follows:

$$t^*a_{2n}a_{2n-1}C_{n-1} + \delta_{n0} = \frac{1}{t}[1 - r^*ra_{2n+1}^2]C_n - r^*a_{2n}^2B_n + r^*a_{2n+1}a_{2n+2}B_{n+1}. \quad (\text{A.8})$$

Setting Eqs. (A.7) and (A.8) equal, we get

$$\begin{aligned} t^*a_{2n+1}^2C_n + \frac{1}{r}[1 - rr^*a_{2n}^2]B_n - \frac{tt^*}{r}a_{2n+1}a_{2n+2}B_{n+1} \\ = \frac{1}{t}[1 - r^*ra_{2n+1}^2]C_n - r^*a_{2n}^2B_n + r^*a_{2n+1}a_{2n+2}B_{n+1}. \end{aligned}$$

Sorting the terms, we obtain

$$\begin{aligned} \left[\frac{1}{r} - \cancel{r^*a_{2n}^2} + \cancel{r^*a_{2n}^2}\right]B_n \\ = \left[\frac{1}{t} - \left(\frac{r^*r}{t} + t^*\right)a_{2n+1}^2\right]C_n + \left(r^* + \frac{tt^*}{r}\right)a_{2n+1}a_{2n+2}B_{n+1}. \end{aligned} \quad (\text{A.9})$$

Since $r^*r + t^*t = rr^* + tt^* = 1$, we can write

$$\begin{aligned} \frac{r^*r}{t} + t^* &= \frac{1}{t}(r^*r + t^*t) = \frac{1}{t}, \\ r^* + \frac{tt^*}{r} &= \frac{1}{r}(r^*r + t^*t) = \frac{1}{r}. \end{aligned}$$

Substituting this into Eq. (A.9), we get

$$\frac{1}{r}B_n = \frac{1}{t}[1 - a_{2n+1}^2]C_n + \frac{1}{r}a_{2n+1}a_{2n+2}B_{n+1}. \quad (\text{A.10})$$

We can now express C_n in terms of B_n by rewriting Eq. (A.10):

$$C_n = \frac{t}{r} \frac{1}{1 - a_{2n+1}^2} B_n - \frac{t}{r} \frac{a_{2n+1}a_{2n+2}}{1 - a_{2n+1}^2} B_{n+1}. \quad (\text{A.11})$$

Replacing n by $n-1$, we can find an expression for C_{n-1} :

$$C_{n-1} = \frac{t}{r} \frac{1}{1 - a_{2n-1}^2} B_{n-1} - \frac{t}{r} \frac{a_{2n-1} a_{2n}}{1 - a_{2n-1}^2} B_n. \quad (\text{A.12})$$

We now substitute Eqs. (A.11) and (A.12) into our recurrence relation for B_n , given by Eq. (A.6):

$$\begin{aligned} [1 - rr^* a_{2n}^2] B_n - tt^* a_{2n+1} a_{2n+2} B_{n+1} &= r\delta_{n0} + rt^* a_{2n} a_{2n-1} \left(\frac{t}{r} \frac{1}{1 - a_{2n-1}^2} B_{n-1} - \frac{t}{r} \frac{a_{2n-1} a_{2n}}{1 - a_{2n-1}^2} B_n \right) \\ &\quad - rt^* a_{2n+1}^2 \left(\frac{t}{r} \frac{1}{1 - a_{2n+1}^2} B_n - \frac{t}{r} \frac{a_{2n+1} a_{2n+2}}{1 - a_{2n+1}^2} B_{n+1} \right). \end{aligned}$$

Removing the brackets, what remains is

$$\begin{aligned} [1 - rr^* a_{2n}^2] B_n - tt^* a_{2n+1} a_{2n+2} B_{n+1} &= r\delta_{n0} + t^* t \frac{a_{2n} a_{2n-1}}{1 - a_{2n-1}^2} B_{n-1} - t^* t \frac{a_{2n}^2 a_{2n-1}^2}{1 - a_{2n-1}^2} B_n \\ &\quad - t^* t \frac{a_{2n+1}^2}{1 - a_{2n+1}^2} B_n + t^* t \frac{a_{2n+1}^3 a_{2n+2}}{1 - a_{2n+1}^2} B_{n+1}. \end{aligned}$$

For the term on the far left, we use that $rr^* a_{2n}^2 = a_{2n}^2 - tt^* a_{2n}^2$. Substituting this and sorting the terms, we get

$$\begin{aligned} t^* t \left[\frac{a_{2n+1}^3 a_{2n+2}}{1 - a_{2n+1}^2} + a_{2n+1} a_{2n+2} \right] B_{n+1} - \left[1 - a_{2n}^2 + t^* t \left(a_{2n}^2 + \frac{a_{2n+1}^2}{1 - a_{2n+1}^2} + \frac{a_{2n}^2 a_{2n-1}^2}{1 - a_{2n-1}^2} \right) \right] B_n \\ + t^* t \frac{a_{2n} a_{2n-1}}{1 - a_{2n-1}^2} B_{n-1} = -r\delta_{n0}. \end{aligned} \quad (\text{A.13})$$

We have to slightly rewrite the coefficients. The terms in between brackets in front of B_{n+1} can be written as

$$\begin{aligned} \frac{a_{2n+1}^3 a_{2n+2}}{1 - a_{2n+1}^2} + a_{2n+1} a_{2n+2} &= \frac{a_{2n+1} a_{2n+2}}{1 - a_{2n+1}^2} (1 - \cancel{a_{2n+1}^2} + \cancel{a_{2n+1}^2}) \\ &= \frac{a_{2n+1} a_{2n+2}}{1 - a_{2n+1}^2}. \end{aligned} \quad (\text{A.14})$$

Similarly, for the B_n coefficient, we use

$$\begin{aligned} a_{2n}^2 + \frac{a_{2n}^2 a_{2n-1}^2}{1 - a_{2n-1}^2} &= \frac{a_{2n}^2}{1 - a_{2n-1}^2} (1 - \cancel{a_{2n-1}^2} + \cancel{a_{2n-1}^2}) \\ &= \frac{a_{2n}^2}{1 - a_{2n-1}^2}. \end{aligned} \quad (\text{A.15})$$

Substituting Eqs. (A.14) and (A.15) into Eq. (A.13), and defining the transparency $D \equiv t^* t$, we get the final recurrence relation for B_n :

$$\begin{aligned} D \frac{a_{2n+2} a_{2n+1}}{1 - a_{2n+1}^2} B_{n+1} - \left[D \left(\frac{a_{2n+1}^2}{1 - a_{2n+1}^2} + \frac{a_{2n}^2}{1 - a_{2n-1}^2} \right) + 1 - a_{2n}^2 \right] B_n + D \frac{a_{2n} a_{2n-1}}{1 - a_{2n-1}^2} B_{n-1} \\ = -\sqrt{1 - D} \delta_{n0}. \end{aligned} \quad (\text{A.16})$$

A.2 Recurrence relation for A_n

We start from Eq. (A.2) and replace n by $n - 1$:

$$C_{n-1} = ta_{2n-2}A_{n-1} - \frac{r^*t}{t^*}a_{2n-1}D_{n-1} + t\delta_{n-1,0}. \quad (\text{A.17})$$

Plugging this into Eq. (A.3) yields

$$\begin{aligned} A_n &= r^*a_{2n}B_n + t^*a_{2n-1}C_{n-1} \\ &= r^*a_{2n}B_n + t^*a_{2n-1} \left(ta_{2n-2}A_{n-1} - \frac{r^*t}{t^*}a_{2n-1}D_{n-1} + t\delta_{n-1,0} \right) \\ &= r^*a_{2n}B_n + \textcolor{violet}{t}t^*a_{2n-1}a_{2n-2}A_{n-1} - r^*ta_{2n-1}^2D_{n-1} + \textcolor{violet}{t}t^*a_{2n-1}\delta_{n-1,0}. \end{aligned}$$

We rewrite the purple terms as $tt^* = 1 - rr^*$ to obtain

$$\begin{aligned} A_n &= r^*a_{2n}B_n + a_{2n-1}a_{2n-2}A_{n-1} - rr^*a_{2n-1}a_{2n-2}A_{n-1} - r^*ta_{2n-1}^2D_{n-1} \\ &\quad + a_{2n-1}\delta_{n-1,0} - rr^*a_{2n-1}\delta_{n-1,0}. \end{aligned}$$

Sorting the terms in a smart way, we get

$$\begin{aligned} A_n - a_{2n-1}a_{2n-2}A_{n-1} &= r^*a_{2n}B_n - r^*a_{2n-1}(ta_{2n-1}D_{n-1} + ra_{2n-2}A_{n-1} + r\delta_{n-1,0}) \\ &\quad + a_{2n-1}\delta_{n-1,0}. \end{aligned} \quad (\text{A.18})$$

We take Eq. (A.1) and replace n by $n - 1$:

$$B_{n-1} = r\delta_{n-1,0} + ra_{2n-2}A_{n-1} + ta_{2n-1}D_{n-1}. \quad (\text{A.19})$$

This is exactly the part in between brackets in Eq. (A.18). Hence, we can write Eq. (A.18) as

$$\textcolor{blue}{A}_n - a_{2n-1}a_{2n-2}\textcolor{blue}{A}_{n-1} = r^*a_{2n}B_n - r^*a_{2n-1}B_{n-1} + a_{2n-1}\delta_{n-1,0}.$$

This is already a correct recurrence relation for A_n . However, to mimic the Averin and Bardas [40], we replace $n - 1$ by n :

$$\textcolor{blue}{A}_{n+1} - a_{2n+1}a_{2n}\textcolor{blue}{A}_n = r^*(a_{2n+2}B_{n+1} - a_{2n+1}B_n) + a_{2n+1}\delta_{n,0}.$$

Since $rr^* = r^*r = R$, we write $r^* = \sqrt{R}$. The source (last term) has a Kronecker δ -function at $n = 0$. Hence, we can plug $n = 0$ into the factor in front of it: $a_{2n+1} = a_1$. Our final recurrence relation for A_n becomes

$$\textcolor{blue}{A}_{n+1} - a_{2n+1}a_{2n}\textcolor{blue}{A}_n = \sqrt{R}(a_{2n+2}B_{n+1} - a_{2n+1}B_n) + a_1\delta_{n,0}. \quad (\text{A.20})$$

B

Recurrence relations for the S/TI/S junction

If we replace the normal metal with a topological insulator (TI), the wave functions stay the same. According to Badiane et al. [41], the reflection coefficient for the hole gets an additional minus sign. This changes the scattering matrices to

$$\begin{aligned} \begin{bmatrix} B_n \\ C_n \end{bmatrix} &= S_e \begin{bmatrix} \delta_{n0} + a_{2n}A_n \\ a_{2n+1}D_n \end{bmatrix}, & S_e &= \begin{bmatrix} r & t \\ t & -r^*t/t^* \end{bmatrix}, \\ \begin{bmatrix} A_n \\ D_{n-1} \end{bmatrix} &= S_h \begin{bmatrix} a_{2n}B_n \\ a_{2n-1}C_{n-1} \end{bmatrix}, & S_h &= \begin{bmatrix} -r^* & t^* \\ t^* & rt^*/t \end{bmatrix}. \end{aligned}$$

The other parts of the calculation remain unchanged. Below, the calculation from the previous section is repeated. The changes are marked in red. The system of equations becomes

$$B_n = r [\delta_{n0} + a_{2n}A_n] + ta_{2n+1}D_n, \quad (\text{B.1})$$

$$C_n = t [\delta_{n0} + a_{2n}A_n] - \frac{r^*t}{t^*} a_{2n+1}D_n, \quad (\text{B.2})$$

$$A_n = -r^* a_{2n}B_n + t^* a_{2n-1}C_{n-1}, \quad (\text{B.3})$$

$$D_{n-1} = t^* a_{2n}B_n + \frac{rt^*}{t} a_{2n-1}C_{n-1}. \quad (\text{B.4})$$

B.1 Recurrence relation for B_n

We repeat the calculations from the previous section, but leave out some of the steps. The changes due to the different sign are marked in red. We start again with D_n :

$$D_n = t^* a_{2n+2}B_{n+1} + \frac{rt^*}{t} a_{2n+1}C_n. \quad (\text{B.5})$$

Substituting Eqs. (B.5) and (B.3) this into Eq. (B.1), we get

$$B_n = r\delta_{n0} - rr^* a_{2n}^2 B_n + rt^* a_{2n} a_{2n-1} C_{n-1} + tt^* a_{2n+1} a_{2n+2} B_{n+1} + rt^* a_{2n+1}^2 C_n. \quad (\text{B.6})$$

Rewriting this equation, we obtain

$$t^* a_{2n} a_{2n-1} C_{n-1} + \delta_{n0} = -t^* a_{2n+1}^2 C_n + \frac{1}{r} [1 + rr^* a_{2n}^2] B_n - \frac{tt^*}{r} a_{2n+1} a_{2n+2} B_{n+1}. \quad (\text{B.7})$$

We substitute Eqs. (B.3) and (B.5) into Eq. (B.2) and work out the brackets.

$$C_n = t\delta_{n0} - tr^*a_{2n}^2B_n + tt^*a_{2n}a_{2n-1}C_{n-1} - r^*ta_{2n+1}a_{2n+2}B_{n+1} - r^*ra_{2n+1}^2C_n.$$

Again, we want to obtain an expression for C_{n-1} , which we do as follows:

$$t^*a_{2n}a_{2n-1}C_{n-1} + \delta_{n0} = \frac{1}{t} [1 + r^*ra_{2n+1}^2] C_n + r^*a_{2n}^2B_n + r^*a_{2n+1}a_{2n+2}B_{n+1}. \quad (\text{B.8})$$

Setting Eqs. (B.7) and (B.8) equal, we get

$$\begin{aligned} -t^*a_{2n+1}^2C_n + \frac{1}{r} [1 + rr^*a_{2n}^2] B_n - \frac{tt^*}{r} a_{2n+1}a_{2n+2}B_{n+1} \\ = \frac{1}{t} [1 + r^*ra_{2n+1}^2] C_n + r^*a_{2n}^2B_n + r^*a_{2n+1}a_{2n+2}B_{n+1}. \end{aligned}$$

Sorting the terms, we obtain

$$\frac{1}{r}B_n = \left[\frac{1}{t} + \left(\frac{r^*r}{t} + t^* \right) a_{2n+1}^2 \right] C_n + \left(r^* + \frac{tt^*}{r} \right) a_{2n+1}a_{2n+2}B_{n+1}.$$

Using $r^*r + t^*t = rr^* + tt^* = 1$, this reduces to

$$\frac{1}{r}B_n = \frac{1}{t} [1 + a_{2n+1}^2] C_n + \frac{1}{r} a_{2n+1}a_{2n+2}B_{n+1}. \quad (\text{B.9})$$

By rewriting Eq. (B.9) and subsequently replacing n by $n-1$, we obtain expressions for C_n and C_{n-1} :

$$\begin{aligned} C_n &= \frac{t}{r} \frac{1}{1 + a_{2n+1}^2} B_n - \frac{t}{r} \frac{a_{2n+1}a_{2n+2}}{1 + a_{2n+1}^2} B_{n+1}, \\ C_{n-1} &= \frac{t}{r} \frac{1}{1 + a_{2n-1}^2} B_{n-1} - \frac{t}{r} \frac{a_{2n-1}a_{2n}}{1 + a_{2n-1}^2} B_n. \end{aligned}$$

Substituting these expressions into Eq. (B.6), we get

$$\begin{aligned} [1 + rr^*a_{2n}^2] B_n - tt^*a_{2n+1}a_{2n+2}B_{n+1} &= rt^*a_{2n}a_{2n-1} \left(\frac{t}{r} \frac{1}{1 + a_{2n-1}^2} B_{n-1} - \frac{t}{r} \frac{a_{2n-1}a_{2n}}{1 + a_{2n-1}^2} B_n \right) \\ &\quad + rt^*a_{2n+1}^2 \left(\frac{t}{r} \frac{1}{1 + a_{2n+1}^2} B_n - \frac{t}{r} \frac{a_{2n+1}a_{2n+2}}{1 + a_{2n+1}^2} B_{n+1} \right) + r\delta_{n0}. \end{aligned}$$

For the term on the far left, we use that $rr^*a_{2n}^2 = a_{2n}^2 - tt^*a_{2n}^2$. Substituting this and sorting the terms, we get

$$\begin{aligned} t^*t \left[a_{2n+1}a_{2n+2} - \frac{a_{2n+1}^3a_{2n+2}}{1 + a_{2n+1}^2} \right] B_{n+1} - \left[1 + a_{2n}^2 + t^*t \left(\frac{a_{2n}^2a_{2n-1}^2}{1 + a_{2n-1}^2} - a_{2n}^2 - \frac{a_{2n+1}^2}{1 + a_{2n+1}^2} \right) \right] B_n \\ + t^*t \frac{a_{2n}a_{2n-1}}{1 + a_{2n-1}^2} B_{n-1} = -r\delta_{n0}. \end{aligned} \quad (\text{B.10})$$

The terms in between brackets in front of B_{n+1} and B_n can be rewritten as, respectively,

$$\begin{aligned} a_{2n+1}a_{2n+2} - \frac{a_{2n+1}^3a_{2n+2}}{1 + a_{2n+1}^2} &= \frac{a_{2n+1}a_{2n+2}}{1 + a_{2n+1}^2}, \\ \frac{a_{2n}^2a_{2n-1}^2}{1 + a_{2n-1}^2} - a_{2n}^2 &= -\frac{a_{2n}^2}{1 + a_{2n-1}^2}. \end{aligned}$$

Plugging these terms back into Eq. (B.10) and using that $D = t^*t$, we are left with

$$\begin{aligned} D \left[\frac{a_{2n+2}a_{2n+1}}{1 + a_{2n+1}^2} B_{n+1} + \left(\frac{a_{2n+1}^2}{1 + a_{2n+1}^2} + \frac{a_{2n}^2}{1 + a_{2n-1}^2} \right) B_n + \frac{a_{2n}a_{2n-1}}{1 + a_{2n-1}^2} B_{n-1} \right] - (1 + a_{2n}^2) B_n \\ = -\sqrt{1 - D}\delta_{n0}. \end{aligned} \quad (\text{B.11})$$

B.2 Recurrence relation for A_n

Similar to before, we substitute Eq. (B.2) into Eq. (B.3)

$$\begin{aligned} A_n &= -r^* a_{2n} B_n + t^* a_{2n-1} C_{n-1} \\ &= -r^* a_{2n} B_n + t^* a_{2n-1} \left(t a_{2n-2} A_{n-1} - \frac{r^* t}{t^*} a_{2n-1} D_{n-1} + t \delta_{n-1,0} \right). \end{aligned}$$

We work out the brackets, use $tt^* = 1 - rr^*$ and sort the terms. What we are left with is

$$\begin{aligned} A_n - a_{2n-1} a_{2n-2} A_{n-1} &= -r^* a_{2n} B_n - r^* a_{2n-1} (t a_{2n-1} D_{n-1} + r a_{2n-2} A_{n-1} + r \delta_{n-1,0}) \\ &\quad + a_{2n-1} \delta_{n-1,0}. \end{aligned}$$

Combining this with Eq. (B.1), we obtain

$$A_n - a_{2n-1} a_{2n-2} A_{n-1} = -r^* a_{2n} B_n - r^* a_{2n-1} B_{n-1} + a_{2n-1} \delta_{n-1,0}.$$

We replace $n-1$ by n and substitute $rr^* = r^*r = R$ and $r^* = \sqrt{R}$. The final recurrence relation for A_n becomes

$$A_{n+1} - a_{2n+1} a_{2n} A_n = -\sqrt{R} (a_{2n+2} B_{n+1} + a_{2n+1} B_n) + a_1 \delta_{n0}. \quad (\text{B.12})$$



Scattering matrix

We define $\psi_{L(R)\pm}$ as the wave function amplitudes of quasi particles carrying the charge current in the $\pm x$ -direction for $x < 0$ ($x > L$). The scattering matrix is then given by

$$\begin{bmatrix} \psi_{L-} \\ \psi_{R+} \end{bmatrix} = \begin{bmatrix} r & t \\ \underline{t} & \underline{r} \end{bmatrix} \begin{bmatrix} \psi_{L+} \\ \psi_{R-} \end{bmatrix}. \quad (\text{C.1})$$

The coefficients r and t can be obtained by assuming an incoming electron-like quasi particle incoming from the left. Similarly, in order to determine \underline{r} and \underline{t} , we assume an incoming electron-like quasi particle incoming from the right.

The wave function for the incoming electron-like quasi particle from the left is given by

$$\psi_{e \rightarrow}(x, y) = \begin{cases} \frac{1}{\sqrt{2}} \left(\begin{bmatrix} 1 \\ e^{i\theta_S} \end{bmatrix} e^{ik_x^S x} + r \begin{bmatrix} 1 \\ -e^{-i\theta_S} \end{bmatrix} e^{-ik_x^S x} \right) e^{ik_y y} & \text{for } x < 0, \\ \frac{1}{\sqrt{2}} \left(a \begin{bmatrix} 1 \\ e^{i\theta} \end{bmatrix} e^{ik_x x} + b \begin{bmatrix} 1 \\ -e^{-i\theta} \end{bmatrix} e^{-ik_x x} \right) e^{ik_y y} & \text{for } 0 < x < L, \\ \frac{t}{\sqrt{2}} \begin{bmatrix} 1 \\ e^{i\theta_S} \end{bmatrix} e^{ik_x^S x} e^{ik_y y} & \text{for } x > L. \end{cases} \quad (2.21)$$

Imposing continuity at $x = 0$ and $x = L$, we obtain a system of four equations with four unknowns (r , a , b and t). Solving the system, we obtain

$$r = 2e^{i\theta_S} \sin(k_x L) \frac{\sin \theta_S - \sin \theta}{e^{-ik_x L} \cos(\theta_S + \theta) + e^{ik_x L} \cos(\theta_S - \theta) - 2i \sin(k_x L)}, \quad (\text{C.2})$$

$$t = \frac{2e^{-ik_x^S L} \cos \theta \cos \theta_S}{e^{-ik_x L} \cos(\theta_S + \theta) + e^{ik_x L} \cos(\theta_S - \theta) - 2i \sin(k_x L)}. \quad (\text{C.3})$$

Assuming an incoming electron-like quasi particle incoming from the right, the wave function we

get is

$$\psi_{e\leftarrow}(x, y) = \begin{cases} \frac{\underline{t}}{\sqrt{2}} \begin{bmatrix} 1 \\ -e^{-i\theta_S} \end{bmatrix} e^{-ik_x^S x} e^{ik_y y} & \text{for } x < 0, \\ \frac{1}{\sqrt{2}} \left(\underline{b} \begin{bmatrix} 1 \\ e^{i\theta} \end{bmatrix} e^{ik_x x} + \underline{a} \begin{bmatrix} 1 \\ -e^{-i\theta} \end{bmatrix} e^{-ik_x x} \right) e^{ik_y y} & \text{for } 0 < x < L, \\ \frac{1}{\sqrt{2}} \left(\begin{bmatrix} 1 \\ -e^{-i\theta_S} \end{bmatrix} e^{-ik_x^S x} + \underline{r} \begin{bmatrix} 1 \\ e^{i\theta_S} \end{bmatrix} e^{ik_x^S x} \right) e^{ik_y y} & \text{for } x > L. \end{cases} \quad (\text{C.4})$$

Imposing continuity at the $x = 0$ and $x = L$ again, we obtain

$$\underline{r} = \frac{2e^{-i\theta_S} \sin(k_x L) (\sin \theta - \sin \theta_S) e^{-2ik_x^S L}}{e^{-ik_x L} \cos(\theta_S + \theta) + e^{ik_x L} \cos(\theta_S - \theta) - 2i \sin(k_x L)}, \quad (\text{C.5})$$

$$\underline{t} = t. \quad (\text{C.6})$$

Similarly, the scattering matrix for holes can be obtained by assuming an incoming hole-like quasi particle from both sides. In the main text, we only use the expression for Eq. (C.2).

D

Nb etch rate calibration

In our structures, we grow Nb contacts with a thickness of 80 nm. On top of that, we grow a 2 nm Pd capping layer. We grew this on a test substrate and covered it partially with photo-resist, such that the parts underneath it are protected and will not be etched. We etched for one minute and removed the photo-resist. We then applied a second layer of photo-resist again and made sure it was partially overlapping with the first layer. We etched again for two minutes and removed the photo-resist. We then put the substrate underneath an atomic force microscope (AFM) and searched for a point where four different thicknesses were visible, as shown in figure D.1.

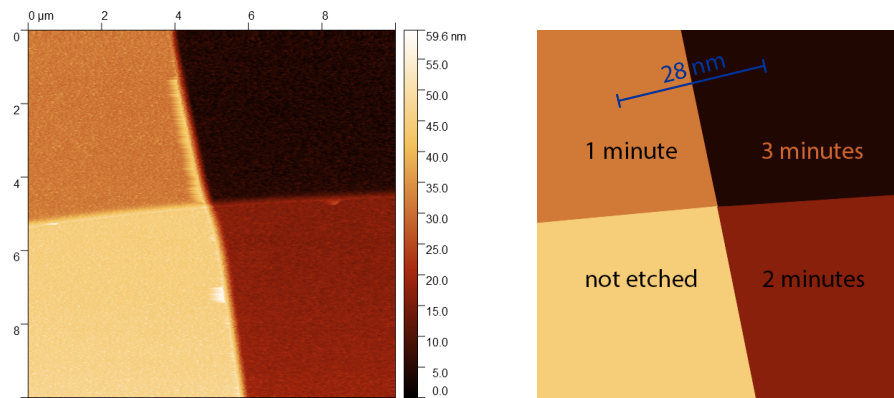


Figure D.1: Nb sample etched twice. This point shows four areas with different etch times. Left: real AFM image. Right: schematic image with etch times and measured step height.

We measured all four steps. Since we are interested in the etch rate of Nb only, comparing two regions that do not include the Pd is the most reliable. We found that the etch rate of Nb is 14 nm/min.

Relation between the DOS and the conductance

The famous BTK theory that we have often considered throughout this thesis [47] considers the conductance of a conventional N/S junction. They show that without barrier, the conductance is constant and equal to 2 inside the gap (i.e. for $E < \Delta$). When they introduce a δ -potential barrier with strength Z , two coherence peaks appear at the gap edge ($E = \pm\Delta$) and the conductance is strongly suppressed inside the gap. With increasing barrier strength, the conductance resembles the density of states of a superconductor (see Figs. 1.12, 2.5 and 2.7) more and more.

The density of states is equal to

$$D(E) = -\frac{1}{\pi} \text{Im} [G(x, x'; E)], \quad (\text{E.1})$$

where $G(x, x'; E)$ is a Green function. The theory concerning Green functions goes beyond the scope of this thesis, but we will say that this function is proportional to the probability amplitude of the wave function. In a superconductor, the wave function consists of the four possible states at a given energy $E > \Delta$, denoted by t_1 to t_4 in Fig. E.1. Hence,

$$G(x, x'; E) \sim \psi^* \psi = |\psi|^2 \sim |t_1|^2 + |t_2|^2 + |t_3|^2 + |t_4|^2. \quad (\text{E.2})$$

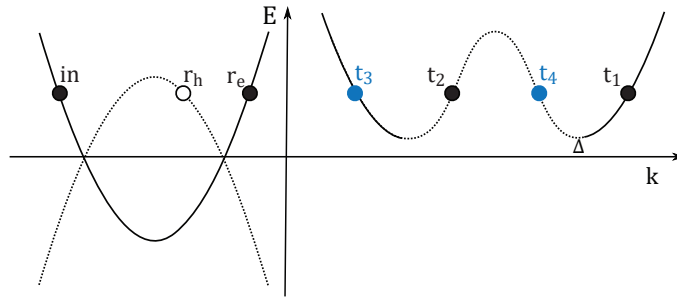


Figure E.1: Dispersion relations of a normal metal (left) and a superconductor (right) with the particles that play a role in the BTK formalism (black) and two additional states that we do not usually consider (blue).

We now return to N/S junction in BTK theory. They consider an incoming electron in the normal metal, which results in a reflected electron and an Andreev reflected hole in the normal metal, and

two transmitted quasi particles in the superconductor (t_1 and t_2 in Fig. E.1). Therefore, if we consider the superconductor in the context of BTK theory, the two blue states in Fig. E.1 do not play a role and the density of states is proportional to

$$D(E) \sim |t_1|^2 + |t_2|^2. \quad (\text{E.3})$$

Let us now consider the conductance. In BTK theory, the conductance is related to the particles in the normal metal (this is easier than considering the superconductor where a pre-factor in the momentum plays a role). The conductance in the normal metal is the sum of the right going particles (i.e. the incoming particle and the reflected hole), minus the left going particle (the reflected electron), i.e.

$$G \sim 1 - |r_e|^2 + |r_h|^2. \quad (\text{E.4})$$

Probability conservation dictates that $|r_e|^2 + |r_h|^2 + |t_1|^2 + |t_2|^2 = 1$. Substituting this in the conductance, we obtain

$$G \sim 2|r_h|^2 + |t_1|^2 + |t_2|^2. \quad (\text{E.5})$$

The Andreev proportion is inversely proportional to the barrier strength, i.e. $|r_h|^2 \sim 1/Z^2$. [47] Hence, it follows that in the limit of a high barrier ($Z \rightarrow \infty$), the conductance is proportional to the density of states,

$$G \sim |t_1|^2 + |t_2|^2 \sim N(E). \quad (\text{E.6})$$

References

- [1] M.J. Wolf, F.S. Grodzinsky, and K.W. Miller. *Artificial Agents, Cloud Computing, and Quantum Computing: Applying Floridis Method of Levels of Abstraction*. Springer, 2012.
- [2] Cade Metz. For Google, quantum computing is like learning to fly. *Wired*. 11 December 2015.
- [3] R. P. Feynman. Simulating physics with computers. *International Journal of theoretical physics*, 21(6/7), 1982.
- [4] Emma Strubell. *An Introduction to Quantum Algorithms*. PhD thesis, University of Massachusetts Amherst, 2011.
- [5] Jason Palmer. Quantum computing: Is it possible, and should you care? *BBC News*. 13 April 2012.
- [6] Naaman Zhou. Australian scientists move closer to world-beating quantum computer. *The Guardian*. 8 March 2018.
- [7] Will Knight. IBM Raises the Bar with a 50-Qubit Quantum Computer. *MIT Technology Review*. 10 November 2017.
- [8] Chetan Nayak, Steven H. Simon, Ady Stern, Michael Freedman, and Sankar Das Sarma. Non-Abelian anyons and topological quantum computation. *Rev. Mod. Phys.*, 80:1083–1159, Sep 2008.
- [9] Picture by Thies Jansen.
- [10] R.P. Feynman, R.B. Leighton, and M. Sands. *The Feynman lectures on physics, Vol. 3*. Ingram publisher services US, 1964.
- [11] D.V. Schroeder. *An introduction to thermal physics*. Pearson, 1999.
- [12] A. Einstein. Concerning an heuristic point of view toward the emission and transformation of light. *Annals of Physics*, 17(132), 1905.
- [13] D. Harrison. *Complementarity and the Copenhagen interpretation of quantum mechanics*. 2002.
- [14] D.J. Griffiths. *Introduction to Quantum Mechanics, second edition*. Pearson Education, 2005.
- [15] Richard D. Mattuck. *A guide to Feynman diagram in the many-body problem*. Dover Books on Physics, 1992.
- [16] Robert C. Hilborn. Answer to Question 7 [“The spinstatistics theorem,” Dwight E. Neuen-schwander. *American Journal of Physics*, 63(298), 1995.
- [17] Ian Duck and E C. G. Sudarshan. Toward an understanding of the spin-statistics theorem. *American Journal of Physics*, 66:284–303, 04 1998.

- [18] J. Bardeen, L.N. Cooper, and J.R. Schrieffer. Theory of superconductivity. *Physical Review*, 108(5), 1957.
- [19] Michael Tinkham. *Introduction to superconductivity*. Dover publications, inc., 1996.
- [20] N. N. Bogoljubov. On a new method in the theory of superconductivity. *Il Nuovo Cimento (1955-1965)*, 7(6):794–805, Mar 1958.
- [21] D. van Delft and P. Kes. The discovery of superconductivity. *Physics Today*, 63(9):38, 2010.
- [22] V.L. Ginzburg and E.A. Andryushin. *Superconductivity*. World Scientific Pub Co Inc, 2004.
- [23] W. Meissner and R. Ochsenfeld. Ein neuer Effekt bei Eintritt der Supraleitfähigkeit. *Die Naturwissenschaften*, 21(44):787–788, 1933.
- [24] Anshul Kogar. Pictures of band theory: a real space view of where bands and bands gaps come from. 11 February, 2018.
- [25] Grigory Tkachov. *Topological Insulators*. Pan Stanford Publishing, 2016.
- [26] V.V. Schmidh. *The Physics of Superconductors*. Springer, 1997.
- [27] C. L. Kane and E. J. Mele. Z_2 topological order and the quantum spin hall effect. *Phys. Rev. Lett.*, 95:146802, Sep 2005.
- [28] Markus Knig, Steffen Wiedmann, Christoph Brne, Andreas Roth, Hartmut Buhmann, Laurens W Molenkamp, Xiao-Liang Qi, and Shou-Cheng Zhang. Quantum Spin Hall Insulator State in HgTe Quantum Wells. *Science*, 318:766–70, 12 2007.
- [29] Marieke Snelder. *Non-triviality matters: examining the interplay between s-wave superconductivity and topological surface states*. PhD thesis, University of Twente, 2015.
- [30] Joe McKendrick. ‘Flipper Bridge’ joins roads of countries that drive on left with those that drive on right. 28 July, 2010.
- [31] E. Frantzeskakis, N. De Jong, B. Zwartsenberg, Y. K. Huang, T. V. Bay, P. Pronk, E. Van Heumen, D. Wu, Y. Pan, M. Radovic, N. C. Plumb, N. Xu, M. Shi, A. De Visser, and M. S. Golden. Micro-metric electronic patterning of a topological band structure using a photon beam. *Scientific Reports*, 5(16309), 2015.
- [32] Liang Fu, C. L. Kane, and E. J. Mele. Topological insulators in three dimensions. *Phys. Rev. Lett.*, 98:106803, Mar 2007.
- [33] Hai-Zhou Lu and Shun-Qing Shen. Weak localization and weak anti-localization in topological insulators. *Proceedings of SPIE - The International Society for Optical Engineering*, 9167, 09 2014.
- [34] A.Yu. Kitaev. Unpaired Majorana fermions in quantum wires. *Physics-Uspekhi*, 44, 2001.
- [35] Sumathi Rao. *Topology and Condensed Matter Physics*. Springer, 2017.
- [36] Jason Alicea. New directions in the pursuit of Majorana fermions in solid state systems. *Reports on Progress in Physics*, 75(7):076501, 2012.
- [37] L.A.B. Olde Olthof, S.-I. Suzuki, A.A. Golubov, M. Kunieda, S. Yonezawa, Y. Maeno, and Y. Tanaka. Theory of tunneling spectroscopy of normal metal/ferromagnet/spin-triplet superconductor junctions. *Phys. Rev. B*, 98:014508, Jul 2018.

-
- [38] C. Li, J.C. de Boer, B. de Ronde, S.V. Ramankutty, E. van Heumen, Y. Huang, A. de Visser, A.A. Golubov, M.S. Golden, and A. Brinkman. 4π periodic Andreev bound states in a Dirac semimetal. 2018. arXiv:1707.03154.
 - [39] Liang Fu and C. L. Kane. Superconducting proximity effect and majorana fermions at the surface of a topological insulator. *Phys. Rev. Lett.*, 100:096407, Mar 2008.
 - [40] D. Averin and A. Bardas. AC Josephson Effect in a Single Quantum Channel. *Phys. Rev. Lett.*, 75:1831–1834, Aug 1995.
 - [41] Driss M. Badiane, Manuel Houzet, and Julia S. Meyer. Nonequilibrium Josephson Effect through Helical Edge States. *Phys. Rev. Lett.*, 107:177002, Oct 2011.
 - [42] Pictures made with the help of Jorrit de Boer.
 - [43] Ion Cosma Fulga. *Scattering theory of topological phase transitions*. PhD thesis, Universiteit Leiden, 2013.
 - [44] Rafael de la Madrid. The role of the rigged Hilbert space in quantum mechanics. *European Journal of Physics*, 26(2), 2005.
 - [45] M.I. Katsnelson, K.S. Novoselov, and A.K. Geim. Chiral tunnelling and the klein paradox in graphene. *Nature Physics*, 2(620), 2006.
 - [46] Alexandre Zagoskin. *Quantum Theory of many-body systems*. Springer, 1998.
 - [47] G. E. Blonder, M. Tinkham, and T. M. Klapwijk. Transition from metallic to tunneling regimes in superconducting microconstrictions: Excess current, charge imbalance, and supercurrent conversion. *Phys. Rev. B*, 25:4515–4532, Apr 1982.
 - [48] Yasushi Nagato, Katsuhiko Nagai, and Jun'ichiro Hara. Theory of the andreev reflection and the density of states in proximity contact normal-superconducting infinite double-layer. *Journal of Low Temperature Physics*, 93(1):33–56, Oct 1993.
 - [49] S. V. Bakurskiy, A. A. Golubov, M. Yu. Kupriyanov, K. Yada, and Y. Tanaka. Anomalous surface states at interfaces in p -wave superconductors. *Phys. Rev. B*, 90:064513, Aug 2014.
 - [50] S. Higashitani, S. Matsuo, Y. Nagato, K. Nagai, S. Murakawa, R. Nomura, and Y. Okuda. Odd-frequency cooper pairs and zero-energy surface bound states in superfluid ^3He . *Phys. Rev. B*, 85:024524, Jan 2012.
 - [51] Carsten Honerkamp and Manfred Sgristt. Andreev reflection in unitary and non-unitary triplet states. *Journal of Low Temperature Physics*, 111(5):895–915, Jun 1998.
 - [52] Masashige Matsumoto, Mikito Koga, and Hiroaki Kusunose. Emergent odd-frequency superconducting order parameter near boundaries in unconventional superconductors. *Journal of the Physical Society of Japan*, 82(3):034708, 2013.
 - [53] Masashige Matsumoto and Manfred Sgrist. Quasiparticle states near the surface and the domain wall in a $p_x + i p_y$ -wave superconductor. *Journal of the Physical Society of Japan*, 68(3):994–1007, 1999.
 - [54] Yasushi Nagato, Seiji Higashitani, and Katsuhiko Nagai. Subgap in the edge states of two-dimensional chiral superconductor with rough surface. *Journal of the Physical Society of Japan*, 80(11):113706, 2011.
 - [55] Yasushi Nagato, Mikio Yamamoto, and Katsuhiko Nagai. Rough surface effects on the p -wave fermi superfluids. *Journal of Low Temperature Physics*, 110(5):1135–1171, Mar 1998.

- [56] Walter Gautschi. Computational aspects of three-term recurrence relations. *SIAM Review*, 9(1):24–82, 1967.
- [57] W.H. Press, B.P. Flannery, S.A. Teukolsky, and W.T. Vetterling. *Numerical Recipes in C: The Art of Scientific Computing*. Cambridge University Press, 1992.
- [58] Germund Dahlquist and Ake Bjork. *Numerical methods in scientific computing*. Society for Industrial and Applied Mathematics, 2008.
- [59] Cleve Moler. Modernization of numerical integration, from quad to integral, May 2016. Math-Works Blogs.
- [60] V. Mourik, K. Zuo, S. M. Frolov, S. R. Plissard, E. P. A. M. Bakkers, and L. P. Kouwenhoven. Signatures of Majorana Fermions in Hybrid Superconductor-Semiconductor Nanowire Devices. *Science*, 336(6084):1003–1007, 2012.
- [61] A. A. Golubov, M. Yu. Kupriyanov, and E. Il'ichev. The current-phase relation in josephson junctions. *Rev. Mod. Phys.*, 76:411–469, Apr 2004.
- [62] J. Wiedenmann, E. Bocquillon, R.S. Deacon, S. Hartinger, O. Herrmann, T.M. Klapwijk, L. Maier, C. Ames, C. Brüne, C. Gould, A. Oiwa, K. Ishibashi, S. Tarucha, H. Buhmann, and L.W. Molenkamp. 4π -periodic josephson supercurrent in hgte-based topological josephson junctions. *Nature Communications*, 7(10303), 2016.
- [63] Sidney Shapiro. Josephson currents in superconducting tunneling: The effect of microwaves and other observations. *Phys. Rev. Lett.*, 11:80–82, Jul 1963.
- [64] Fernando Domínguez, Fabian Hassler, and Gloria Platero. Dynamical detection of majorana fermions in current-biased nanowires. *Phys. Rev. B*, 86:140503, Oct 2012.
- [65] Estimation was made based on numbers that were experimentally obtained for BSTS by Bob de Ronde.
- [66] M Wimmer, A R Akhmerov, J P Dahlhaus, and C W J Beenakker. Quantum point contact as a probe of a topological superconductor. *New Journal of Physics*, 13(5):053016, 2011.
- [67] Chun-Xiao Liu, F. Setiawan, Jay D. Sau, and S. Das Sarma. Phenomenology of the soft gap, zero-bias peak, and zero-mode splitting in ideal majorana nanowires. *Phys. Rev. B*, 96:054520, Aug 2017.
- [68] Hao Zhang, Chun-Xiao Liu, Sasa Gazibegovic, Di Xu, John A. Logan, Guanzhong Wang, Nick van Loo, Jouri D.S. Bommer, Michiel W.A. de Moor, Diana Car, Roy L.M. op het Veld, Petrus J. van Veldhoven, Sebastian Koelling, Marcel A. Verheijen, Mihir Pendharkar, Daniel J. Pennachio, Borzoyeh Shojaei, Joon Sue Lee, Chris J. Palmstrom, Erik P.A.M. Bakkers, S. Das Sarma, and Leo P. Kouwenhoven. Quantized majorana conductance. *Nature*, 556, 2018.
- [69] Thijs Scholten. Master Thesis - Superconductor $\text{Bi}_{0.5}\text{Sb}_{0.5}\text{Te}_{1.7}\text{Se}_{1.3}$ topological insulator hybrid devices, 2013.
- [70] Gerd Bergmann. Weak localization in thin films: a time-of-flight experiment with conduction electrons. *Physics Reports*, 107(1):1 – 58, 1984.
- [71] D.I. Pikulin, J.P. Dahlhaus, M. Wimmer, H. Schomerus, and C.W.J. Beenakker. A zero-voltage conductance peak from weak antilocalization in a Majorana nanowire. *New Journal of Physics*, 14(12):125011, 2012.
- [72] Supriyo Datta. *Electronic Transport in Mesoscopic Systems*. Cambridge University Press, 1995.

-
- [73] Chun-Xiao Liu, Jay D. Sau, Tudor D. Stanescu, and S. Das Sarma. Andreev bound states versus majorana bound states in quantum dot-nanowire-superconductor hybrid structures: Trivial versus topological zero-bias conductance peaks. *Phys. Rev. B*, 96:075161, Aug 2017.
- [74] V.R. Karasik and I.Yu. Shebalin. Superconducting properties of pure niobium. *Soviet physics JETP*, 30(6), 1969.
- [75] Sungjae Cho, Brian Dellabetta, Ruidan Zhong, John Schneeloch, Tiansheng Liu, Genda Gu, Matthew J. Gilbert, and Nadya Mason. Aharonov-bohm oscillations in a quasi-ballistic three-dimensional topological insulator nanowire. *Nature Communications*, 6, 2015.
- [76] Vincent E. Sacksteder and Quansheng Wu. Quantum interference effects in topological nanowires in a longitudinal magnetic field. *Phys. Rev. B*, 94:205424, Nov 2016.
- [77] A. Wolos, S. Szyszko, A. Drabinska, M. Kaminska, S. G. Strzelecka, A. Hruban, A. Materna, M. Piersa, J. Borysiuk, K. Sobczak, and M. Konczykowski. g -factors of conduction electrons and holes in Bi_2Se_3 three-dimensional topological insulator. *Phys. Rev. B*, 93:155114, Apr 2016.
- [78] S. Hikami, A.I. Larkin, and Y. Nagaoka. Spin-orbit interaction and magnetoresistance in two dimensional random systems. *Prog. Theor. Phys.*, 63(2), 1980.
- [79] Weizhe Edward Liu, Ewelina M. Hankiewicz, and Dimitrie Culcer. Weak localization and antilocalization in topological materials with impurity spin-orbit interactions. *Materials (Basel)*, 10(7)(807), 2017.
- [80] Nico Hendrickx. Master Thesis - Transport measurements on S-TI junctions, 2017. Page 31.
- [81] Yu-Hsin Su, Wujun Shi, Claudia Felser, and Yan Sun. Topological Weyl semimetals in $\text{Bi}_{1-x}\text{Sb}_x$ alloys. *Phys. Rev. B*, 97:155431, Apr 2018.
- [82] D.J. Griffiths. *Introduction to electrodynamics, third edition*. Pearson Education, 2008.